INFORMATION TO USERS

This manuscript has been reproduced from the microfilm master. UMI films the text directly from the original or copy submitted. Thus, some thesis and dissertation copies are in typewriter face, while others may be from any type of computer printer.

The quality of this reproduction is dependent upon the quality of the copy submitted. Broken or indistinct print, colored or poor quality illustrations and photographs, print bleedthrough, substandard margins, and improper alignment can adversely affect reproduction.

In the unlikely event that the author did not send UMI a complete manuscript and there are missing pages, these will be noted. Also, if unauthorized copyright material had to be removed, a note will indicate the deletion.

Oversize materials (e.g., maps, drawings, charts) are reproduced by sectioning the original, beginning at the upper left-hand corner and continuing from left to right in equal sections with small overlaps. Each original is also photographed in one exposure and is included in reduced form at the back of the book.

Photographs included in the original manuscript have been reproduced xerographically in this copy. Higher quality 6" x 9" black and white photographic prints are available for any photographs or illustrations appearing in this copy for an additional charge. Contact UMI directly to order.

UMI

A Bell & Howell Information Company
300 North Zeeb Road, Ann Arbor MI 48106-1346 USA
313/761-4700 800/521-0600

DYNAMICS OF PATTERN FORMATION DURING DIRECTIONAL SOLIDIFICATION OF BINARY ALLOYS

by

Wolfgang Karl Josef Losert

A dissertation submitted to the Graduate Faculty in Physics in partial fulfillment of the requirements for the degree of Doctor of Philosophy, The City University of New York.

1998

This manuscript has been read and accepted for the Graduate Faculty in Physics in satisfaction of the dissertation requirement for the degree of Doctor of Philosophy.

23 Feb 1998
Date

Chair of Examining Committee

2/23/98
Date

Executive Officer

H. Z. Cummins

H. Chou

H. Falk

J. Koplik

M. Tomkiewicz

P. Wiltzius

Supervisory Committee

THE CITY UNIVERSITY OF NEW YORK

Abstract

DYNAMICS OF PATTERN FORMATION DURING DIRECTIONAL SOLIDIFICATION OF BINARY ALLOYS

by

Wolfgang Karl Josef Losert

Advisor: Professor H.Z. Cummins

The dynamics of pattern formation during directional solidification of binary alloys was investigated experimentally on the transparent organic crystal Succinonitrile doped with the laser dye Coumarin 152 (solute). The UV fluorescence properties of Coumarin 152 were used to measure the solute concentration field *in situ* during solidification. Because UV absorption by the Coumarin 152 locally heats up the sample, UV illumination of the solid-liquid interface through a mask with rows of uniformly spaced holes was used to apply spatially periodic perturbations for a large range of perturbation wavelengths. Through the perturbations the interface was forced into stable and (temporarily) into unstable patterns of a desired wavelength. The decay mechanisms of unstable patterns were measured with this method and additional stable patterns, not accessible during the dynamics of

pattern formation from an initially planar front, were found.

While only preliminary results were obtained on the complete dynamics of formation of a dendritic array as it evolves through a coarsening phase from the initial instability of a planar front, key aspects of the coarsening process (the initial instability, the cell to dendrite transition and dendritic array stability) were analyzed in detail.

Measurements of positive and also negative growth coefficients for perturbations of the planar interface were carried out and verified that the Warren-Langer time dependent linear stability analysis [J.A. Warren and J.S. Langer, Phys. Rev. E, **47**, 2702 (1993)] provides a good description for the stability and initial instability of a planar interface.

At high crystal growth speeds, the stability of dendritic arrays was measured directly through perturbations and period doubling was found to be the mechanism limiting stability for small dendrite spacings, in agreement with the Warren-Langer dendritic stability analysis. [J.A. Warren and J.S. Langer, Phys. Rev. A, **42**, 3518 (1990)].

In addition, at intermediate crystal growth speeds, the stability region and limiting instability mechanisms of asymmetric doublet cellular patterns were investigated and compared to phase-field model simulations by Kopczyński, Rappel and Karma.

ACKNOWLEDGEMENTS

I am deeply grateful to my advisor, Professor Herman Z. Cummins, for letting me work on such an interesting project when I first came to his laboratory as an exchange student, and for his continuous help and guidance during my entire graduate work.

I want to thank everybody I collaborated with on these experiments. Their direct contributions to this work are acknowledged in the appropriate chapters, but the ideas coming from them were invaluable. I am very thankful to Jim Warren who gave me insight into the Warren-Langer theory, which became a foundation for many experimental results in this thesis. I learned much from the collaboration with Przemek Kopczyński, Wouter-Jan Rappel and Alain Karma, who helped me understand their phase-field model computer simulations and theoretical aspects of directional solidification. As an experimentalist, I profited most from discussions and the collaborative experiments with Oscar Mesquita, José Marcos Figueiredo and Orlando Gomes.

Daniel Stillman played an important part in this work, since he participated in parts of the experiments, helped in many rounds of sample preparation and also started my interest in teaching.

I thank Tracy Turner, Joel Hernandez, and Paul Shen for providing such a pleasant work atmosphere.

I am very thankful to Yoon Hwae Hwang for his good advice on how to become a physicist and many interesting conversations.

Without my parents, who gave me continuous support and encouragement, this thesis would not have been possible.

Finally, I thank Johanna for giving meaning to it all and for her enormous patience during my graduate student days.

Contents

List of Tables

List of Figures

Chapter 1

INTRODUCTION

[1] Why and how does nature form so many complex shapes and patterns? The fascination with beautiful patterns on different lengthscales, the abundance of snowflake patterns or the arrangement of stars into galaxies for example, has certainly inspired scientists. One reward for studying pattern formation is that the patterns often reveal underlying structures on a much smaller lengthscale or very weak forces. The patterns in turn are frequently observed as microstructures of materials orders of magnitude larger and can influence physical properties on that larger scale. In probably the first breakthrough in understanding pattern formation, the symmetry of snowflakes led Kepler to an understanding of the atomic order in snow [5, 6] long before it would have been possible to test the atomic

[1]Portions of text and figures in this thesis were adapted from my publications [1, 2, 3, 4]. Chapters or sections adapted from publications are noted in a footnote at the beginning of that chapter.

order itself.

However, while many physical problems can be expressed by linear equations, pattern formation is highly nonlinear and therefore harder to analyze theoretically or experimentally, as small parameters or slight changes of the environment may quantitatively or qualitatively alter the observed pattern.

Many patterns occur as a result of dynamical instabilities, when a sufficiently strong force drives a system far from equilibrium. Hydrodynamic systems in particular exhibit many dynamical instabilities, which trigger patterns such as turbulent flow or arrays of convective rolls. Dynamical instabilities also often take place at the interface between two phases of one material, e.g. at the solid-liquid interface of a crystal, or at the interface between immiscible materials e.g. oil and air. In stationary state the interfaces are given by the minimization of free energy, and their shape is mostly planar or spherical. When driven far from equilibrium (when the crystal is grown into the melt or air is pressed into oil), the free interfaces become dynamically unstable and evolve into more complex patterns.

Most of the instabilities we will discuss in this thesis occur at the solid-liquid interface during growth of binary alloys from the melt. In alloy solidification instabilities often lead to dendritic (i.e. treelike) microstructures, which are of considerable practical importance. While material properties of solidified alloys depend on the macroscopic shape of the sample and the alloy composition, they are also strongly influenced by these microscopic patterns, which reflect a 'memory' of the shape of the solid-liquid interface during the solidification process.

Dendritic crystal growth mechanisms influence the size, shape and orientation of crystalline grains in a regular, polycrystalline metal. The grain shape and orientation is important, since diffusion of grainboundaries between crystalline grains can alter the length of a material, especially for materials subject to sustained high temperatures and large centrifugal forces, e.g. turbine blades. Grainboundaries perpendicular to those forces can shift and thereby elongate a turbine blade, potentially making it touch the turbine housing and causing serious damage. While a regular cast creates approximately spherical grains, directional solidification with a proper orientation of dendrites can create long grains along the blade axis with no grainboundaries perpendicular to it, and it is possible to eliminate grainboundaries completely. Figure 1.1, taken from ([7], page 8) shows at the left a regular cast turbine blade, in the middle a directionally solidified blade, and to the right a grainboundary free turbine blade.

New evidence about the cause for the sinking of the Titanic, recently reported in the New York Times [8], also illustrates the influence of grainboundaries on essential macroscopic material properties. Examination of the wreckage suggests that the heads of rivets, which held the steel hull together, broke off when an iceberg hit the Titanic and made the rivets pop out. This created large gaps between metal plates of the hull and accelerated, possibly even caused the disaster, since the steel plates themselves did not break to the extent previously assumed. Metallography of some recovered rivets found grainboundaries perpendicular to the applied force with large intergranular voids in the region of the rivet heads severely weakening

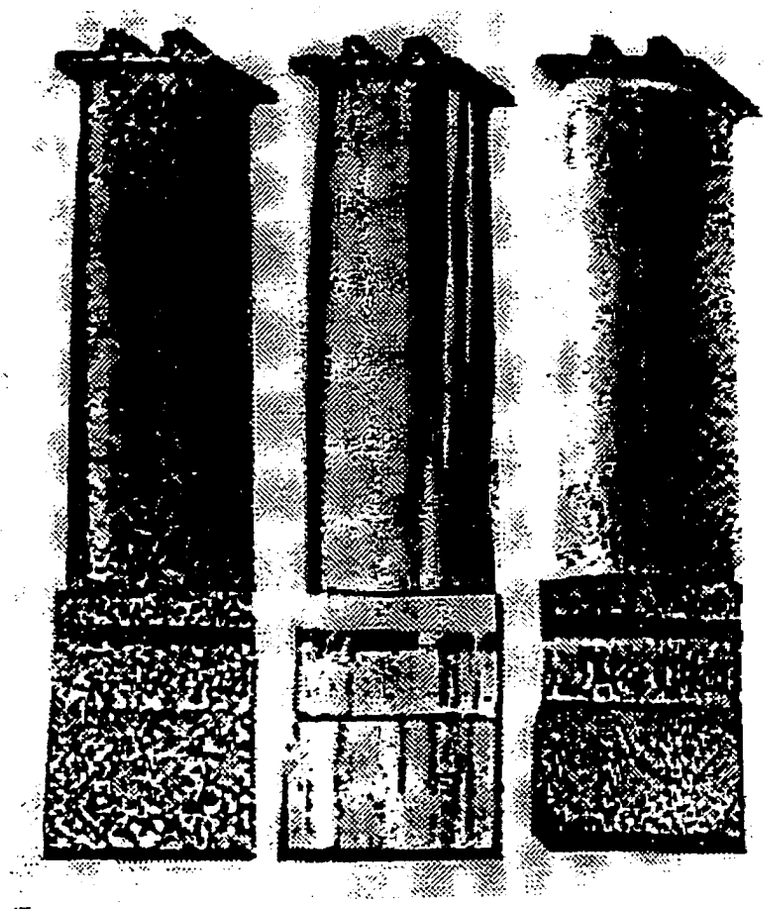

Figure 1.1: Grain structure of turbine blades, from left to right: Regular cast, directionally solidified and grainboundary free directionally solidified turbine blade. Taken from ([7], page 8).

those small but crucial parts of the ship. Figure 1.2, taken from that article [8], shows a metallographic image of one rivet, an enlargement with grainboundaries perpendicular to the force acting on the rivet, and illustrations.

Within a grain, the microscopic lengthscales of dendrites also turn out to have an important influence on the macroscopic mechanical properties material scientists are most interested in. It was found that if the dendritic trunks are in the direction of the centrifugal force they "serve as a continuous fiber ... and contribute to strength and ductility" [9]. The cracking rate is higher in coarser microstructures and the cracking probability is a function of the spacing between dendrites [10, 11]. Experiments on X4CrNi18-10 steel show that the spacing between sidebranches has a large influence on mechanical properties [12].

Metallic alloys can be designed to meet specifications for example for creep, ductility, elasticity or rupture life. Design has traditionally been done using empirical equations based on experimental data. For new superalloys consisting of ten components this is unlikely to give the best possible result in a reasonable time without a better theoretical understanding of the mechanisms through which patterns form during crystal growth. A detailed understanding is especially needed, since the lengthscales of the dendritic trunk, sidebranch, and interdendritic spacing are found to be strongly dependent on the solidification process in metals [13].

The formation of alloy microstructures is frequently studied in directional solidification of binary alloys, where the sample is pulled through a linear temperature gradient at a constant pulling speed, which (after a transient) leads to a uniform

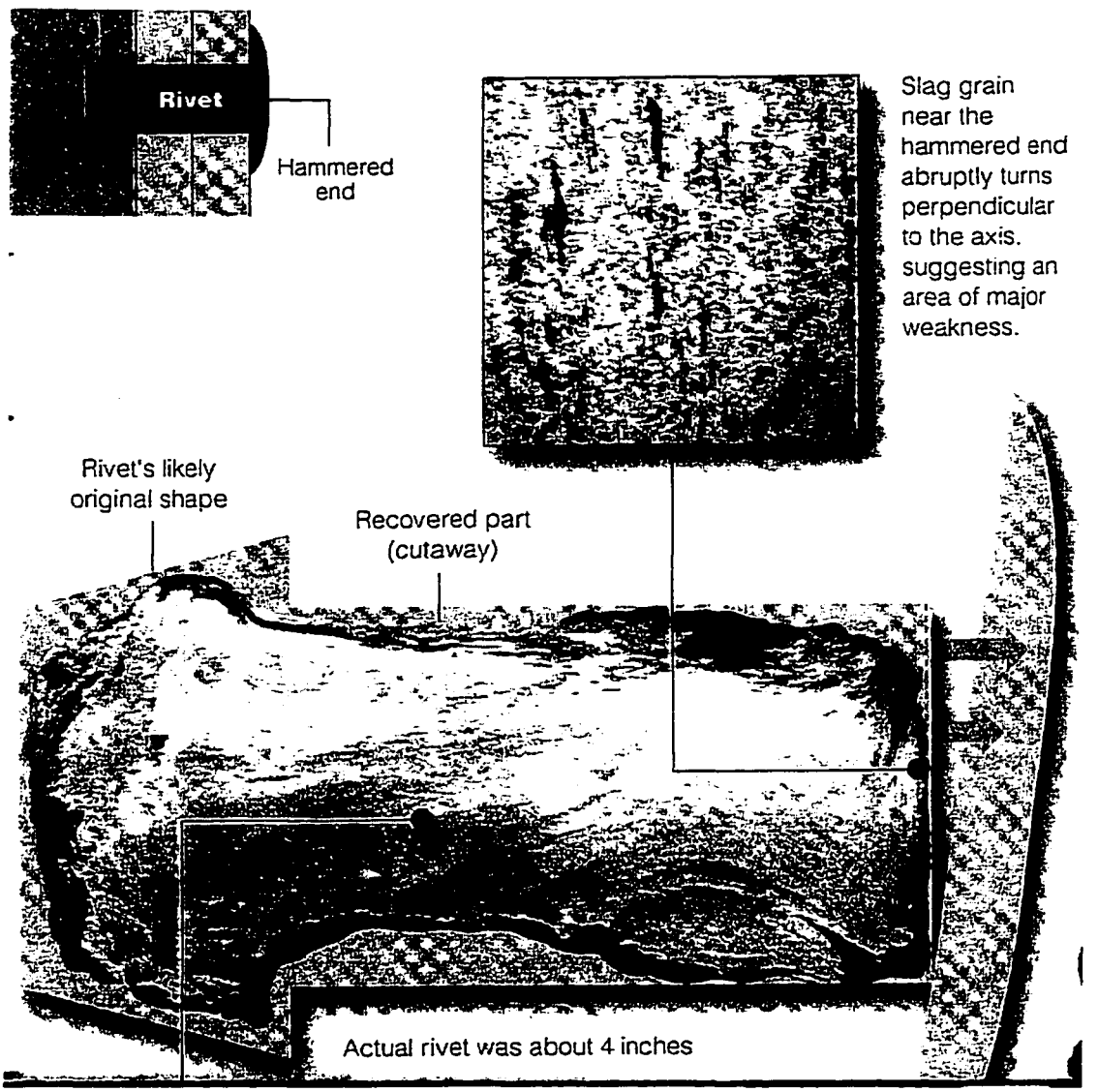

Figure 1.2: Rivets from the Titanic. Metallographic image of one rivet, an enlargement showing grainboundaries perpendicular to the force acting on the rivet, and illustrations. Taken from [8].

crystal growth speed and often to a steady state solid-liquid interface pattern (see [14] for a review). In many experiments, where the motor is started abruptly and set to a constant speed, the initially planar solid-liquid interface reproducibly evolves into one steady state pattern. At rest and at low pulling speeds the solid-liquid interface is planar, stabilized by the temperature gradient. Above a critical speed the planar interface destabilizes due to the Mullins-Sekerka instability [15] and small amplitude cells develop. At intermediate speeds (about five to ten times the critical speed in our experiments) the grooves between cells become deep. At high pulling speeds (usually at least one order of magnitude larger than the critical speed [16]) the cells develop sidebranches and an array of dendrites forms. Figure 1.3 shows those steady state patterns at increasing speeds from top to bottom. In figure 1.4, the evolution of the interface morphology, following the start of the motor at high speed, from a stationary planar interface to a steady state dendritic array is shown from top to bottom.

In addition to these symmetric patterns asymmetric doublet states can be observed in different pulling speed regimes. At high pulling speeds dendritic doublets have been observed in experiments [17] and found in simulations [18, 19]. At intermediate pulling speeds cellular doublets were observed experimentally by Jamgotchian, Trivedi and Billia [20] and numerically by Kopczyński *et al* [21].

The physical origin of the instability of the planar interface in directional solidification of alloys was described in 1953 by Rutter and Chalmers and by Tiller *et al* as *constitutional supercooling* [22, 23]. Since the solute is usually more soluble

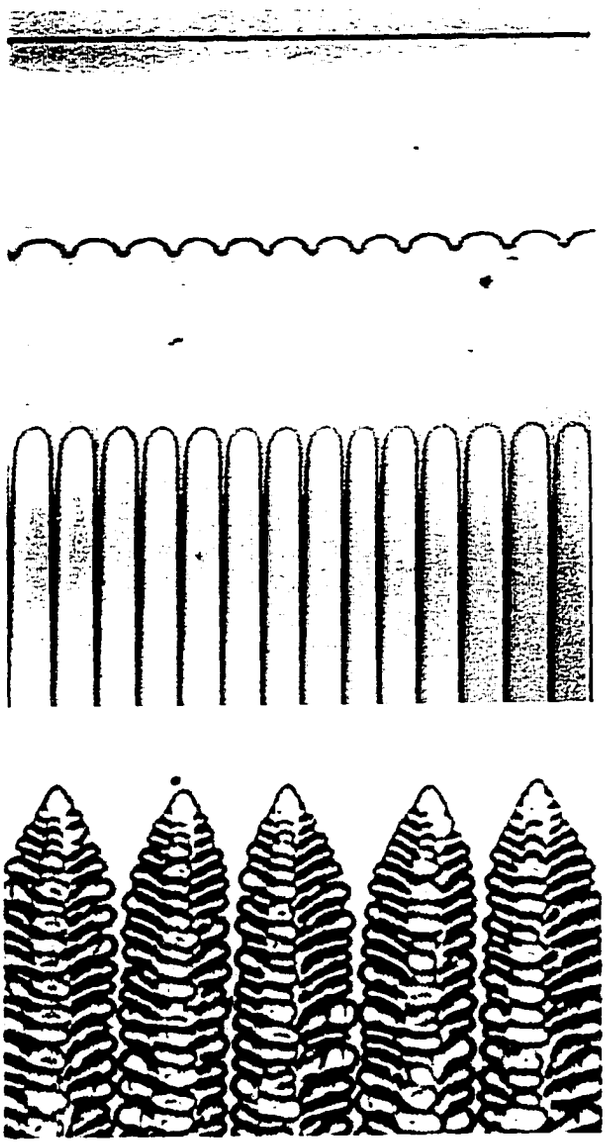

Figure 1.3: Steady-state patterns formed at the crystal-melt interface of a binary alloy of Succinonitrile-Coumarin 152 during directional solidification. From top to bottom (with increasing growth speed): planar interface, cellular interface, deep cells, and dendritic array.

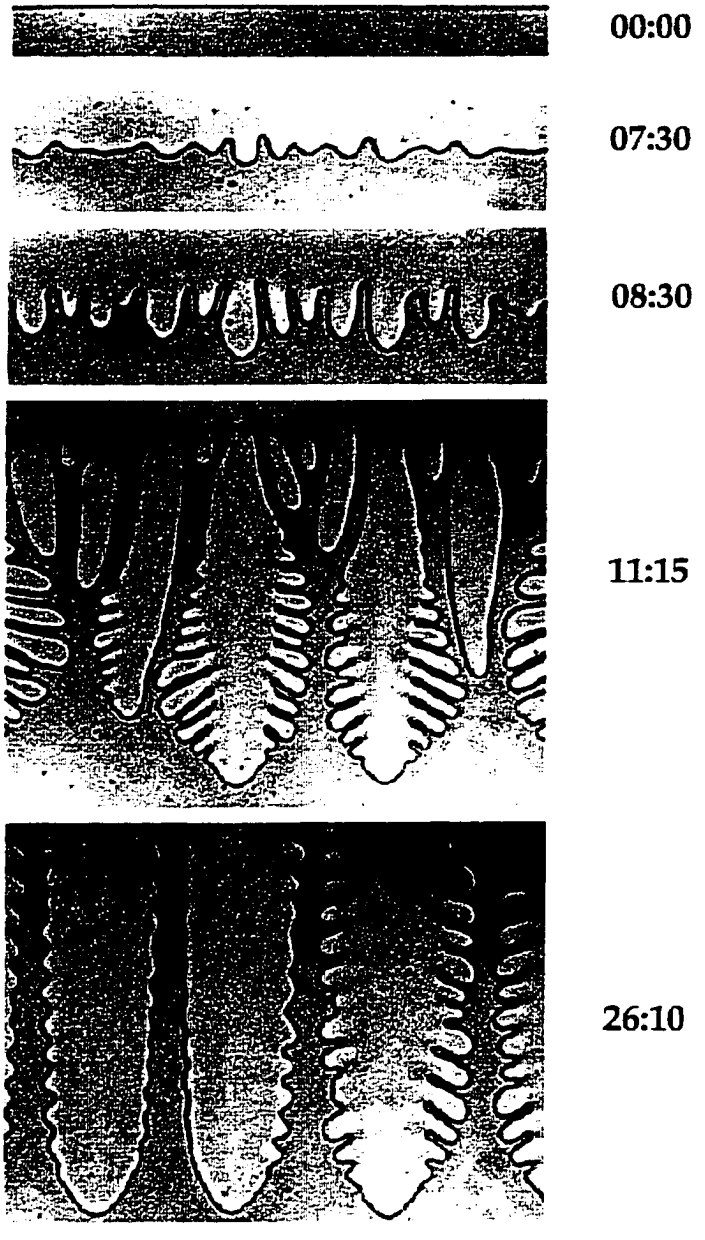

Figure 1.4: Time evolution of the interface morphology for SCN-Rhodamine 6G at constant pulling speed V_P ($C_\infty = 0.325$wt%, $V_P = 3.11\mu$m/s, $G = 2.8$K/cm). From top to bottom: stationary planar interface, cellular pattern at the crossover time, onset of nonlinear instabilities, coarsening phase, and steady state dendritic array. Elapsed time (in minutes:seconds) from the initiation of pulling is shown at the right.

in the melt than in the crystal, solute rejection occurs continuously during solidification, producing a *snowplow* buildup of rejected solute ahead of the advancing solidification front. Because of freezing-point depression, the local crystallization temperature ahead of the advancing front increases with distance, inducing the instability if the gradient in crystallization temperature exceeds the actual temperature gradient present at the interface. The dynamical theory of this solidification instability was first analyzed in 1964 in a seminal paper by Mullins and Sekerka [15], to be described in chapter 2.2.1.

Studying morphological instabilities in metallic alloys is extremely difficult because the samples are opaque and the high melting temperature impedes precise control of the solidification conditions. The usual metallurgical approach is to allow the sample to solidify, and then to cut, polish, and etch the exposed surface so that the solidification pattern can be examined in a microscope.

A major experimental breakthrough occurred in 1965 when Jackson and Hunt showed that transparent organic materials with low surface tension anisotropy effectively solidify like metals, and the evolution of pattern-forming instabilities can be studied *in situ* in thin samples of these materials in an ordinary optical transmission microscope equipped with a motor-driven temperature-gradient stage (directional solidification, see Fig. 2.1) [24, 25]. Stimulated by this convenient transparent analogue of metallic alloys, many experimental studies of solidification instabilities and pattern formation were performed on these materials (e.g. succinonitrile (SCN) doped with acetone) by various groups, and detailed

tests of theoretical predictions were undertaken. (Reviews can be found in, e.g., Refs. [14, 26, 27, 28]). Recent experimental tests have shown that analytic formulas, derived from experiments on organic model systems, are adequate to predict lengthscales in metallic dendrites [29]. The hope is that further theoretical understanding of organic model alloys will also be transferable to the technologically important metallic alloys, leading to a better predictability of pattern formation in new materials.

Dendritic growth theory may also be applicable to the dynamics of void formation through etching in n-type silicon [30]. Voids in silicon have been found to increase the bandgap into the visible range indicating the possibility of semiconductor lasers and other applications using silicone technology. The voids grow into a dendritic shape, since their growth is driven by an applied electric field that depends on the shape of the surface. The finetuning of the bandgap requires accurate control over the pattern of the remaining silicon after etching, i.e. good control over the dendrite tip radius and the interdendritic spacing during etching.

As for snowflakes, observation of patterns under different growth conditions is necessary but not sufficient for understanding the underlying forces and dynamical instabilities that create the pattern. During the past decade the study of dynamical instabilities has developed dramatically due to both major theoretical advances and the introduction of videomicroscopy and computerized digital image analysis techniques permitting precise quantitative tests of theoretical predictions.

Many earlier experiments have investigated, which pattern is selected by the

interface at a given pulling speed (see e.g. [31, 32]). The radius and position of a dendrite tip in steady state at different pulling speeds was explained by microscopic solvability theory [33, 34]. The spacing between cells and dendrites, on the other hand, a very important parameter in metallic alloys, has not yet been explained theoretically, even though some phenomenological models, derived from experiments where the motor was started at a given pulling speed, exist in the literature [35, 36]. Recent experiments [1, 37, 38] (one described in chapter 5) and theoretical studies [39, 40] have shown, however, that the spacing between dendrites is history dependent, and that at a given pulling speed the array is stable for a range of interdendritic spacings. The fitting functions, which work remarkably well when the motor is started abruptly, do not work any more under a change in pulling speed [41]. A similar history dependence was also observed for cellular array spacings [42].

In light of these experiments, the focus of this thesis is to investigate **separately** the questions:

1. Which patterns are *stable* at a given pulling speed?

2. What are the *mechanisms limiting stability*?

3. Since a range of spacings is stable, how is one stable pattern reproducibly *selected* when the directional solidification experiments follows the same protocol?

4. How can other stable patterns be selected at a given pulling speed?

These questions are addressed with new measurements and experimental techniques. Different experimental approaches are possible in order to determine, which patterns are stable at a given pulling speed. One approach is to change the pulling speed in the course of the experiment and to measure whether the pattern remains stable at the new speed. Another option is to force the interface into a pattern of a desired wavelength and to measure whether that pattern remains stable, without changing the pulling speed. In order to investigate pattern selection, it is necessary to analyse the dynamics of pattern formation starting from a planar front (e.g the dynamics of formation for a dendritic array shown in figure 1.4) or the dynamics starting from another pattern present at the start of the experiment.

To force the interface into a pattern of a desired wavelength, an alloy model system and an apparatus for spatially periodic perturbations was developed, which is described in chapter 3. Periodic perturbations have been used before: Perturbations periodic in time determined the amplitude of sidebranching as a function of perturbation frequency at a dendrite tip [43]. Variations in gas pressure periodic in time lead to sidebranching of Saffman-Taylor fingers[2], when anisotropy was introduced into the system [44]. A spatially periodic grid of separating wires was used to set a uniform initial distribution of gas fingers in a Saffman-Taylor experiment [45] in order to observe the coarsening dynamics of those fingers. In another experiment a spatially periodic grid was etched into the cover glass to cre-

[2]Saffman Taylor fingers are gas fingers that form when gas is pressed into a thin oil filled channel

ate surface tension anisotropy and thus dendritic growth in a radial Hele-Shaw flow experiment [46]. However, to our best knowledge, brief, small amplitude spatially periodic perturbations that create small modulations of the unperturbed interface pattern have not been used to study pattern formation in crystal growth.

The first major experimental result in this thesis in chapter 4 is a detailed analysis of the initial instability of the planar interface. The experiments have shown that the Mullins-Sekerka analysis provides a qualitatively correct description of the planar-cellular instability, but the experimentally observed initial cellular patterns usually have considerably larger wavelengths than the theory predicts. The origin of this disagreement lies in one assumption of the Mullins-Sekerka approach: that the instability of a planar front occurs after the dynamical steady state has been reached. In reality, the planar interface will generally become unstable before the steady-state concentration profile has been established. Thus, in order to quantitatively describe the initial instability and its evolution, a non-steady-state theory is needed. A generalization of the Mullins-Sekerka theory incorporating non-steady-state dynamics was developed recently by Warren and Langer [39], opening the way for a full analysis of the evolution of dendritic patterns during solidification. In chapter 2.2.2, we will briefly review the Warren-Langer approach, and then present experimental results obtained with a new model alloy system which allows quantitative tests of many of the new theoretical predictions in chapter 4. We have analyzed the time dependence of both the interface morphology and the solute concentration field starting with the initial transient following the initiation

of crystal growth, investigated the time evolution of the linear growth coefficients, and determined the time required for the initial instability to develop.

A second major part of this thesis is the problem of dendritic array stability, discussed in chapter 5, and the associated problem of the cell to dendrite transition, discussed in chapter 6. The stability of a uniform array of dendrites was measured directly through perturbations and continuous small step reductions in the pulling speed. Period doubling was found to be the mechanism limiting stability for small dendrite spacings, in agreement with the Warren-Langer dendritic stability analysis [39, 40].

A third major part of this thesis is a study of pattern stability and selection on asymmetric doublet cells discussed in chapter 7, in connection with phase-field model simulations by Kopczyński, Rappel and Karma (included as appendix C). In our experiments and in the simulations the interface was forced into a range of stable doublets and also into transient unstable doublets, in order to analyze the stability range and dynamical evolution of doublet cellular structures. Phase-field model simulations and experiments show remarkable qualitative agreement in the dynamic evolution, steady state structure, and instability mechanisms of doublet cellular arrays.

Chapter 2

THEORY OF DIRECTIONAL SOLIDIFICATION

2.1 Basic Principles of Directional Solidification

The basic principles of directional solidification (DS) of dilute binary alloys are best discussed on the simplest model system shown in Fig. 2.1, where the sample, assumed to be two-dimensional and isotropic, moves in the $-z$ direction at constant pulling speed V_P in an externally-imposed temperature gradient G parallel to the z-direction. The solid-liquid interface in this case is one-dimensional, parallel to the x-axis.[1] This model is realistic for many experiments, including the experiments discussed in this thesis, where a thin binary alloy sample is used, which has

[1]For an experimentalist's review of one-dimensional interfaces see [47].

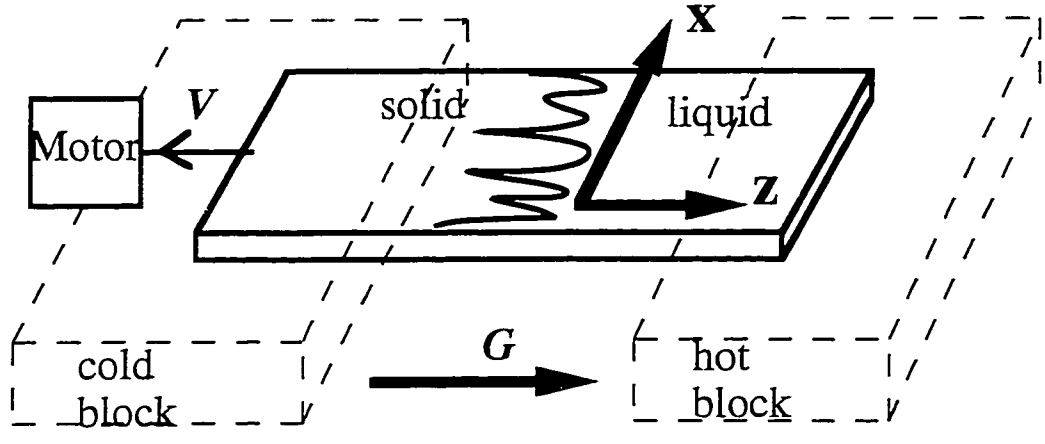

Figure 2.1: Schematic drawing of the directional solidification experiment. The (thin) sample is moved through the temperature gradient G at pulling speed V_P in the $-z$ direction while the crystal-melt interface parallel to the x-axis remains nearly fixed in the laboratory reference frame.

a smaller thickness than the characteristic size of most interface patterns under investigation, thus allowing for the *in situ* observation of a quasi one-dimensional interface pattern.[2]

A continuum description is used for low-anisotropy materials and local thermodynamic equilibrium is assumed. The interface temperature $T_i(x)$, where x is the direction parallel to the interface, is given by

$$T_i(x) = T_M - mC_i(x) - d_0\kappa(x)T_M \tag{2.1}$$

In Eq. 2.1 T_M is the bulk melting temperature of the major component of the dilute binary alloy, m is the slope of the liquidus line, which is a constant in the small concentration limit, C_i is the concentration of solute (the minor material component of the alloy) on the liquid side of the interface, $d_0 = \sigma/L$ is the capillary length (where σ is the surface free energy density and L is the latent heat), and $\kappa(x)$ is the local interface curvature. The second term on the right of Eq. 2.1 is the freezing point depression due to the solute; the third term is freezing point depression due to curvature, the Gibbs-Thomson correction. Attachment kinetics lead to additional freezing point depression adding also kinetic anisotropy [48], but the term is negligible for DS of most alloys, for which the interface is microscopically rough, the melting entropy low, and correspondingly the attachment kinetics quasi-instantaneous. Attachment kinetics can become significant in DS, e.g. in

[2]While most experimental and theoretical results for two dimensions also hold for bulk samples, the differences between pattern formation in two and in three dimensions, and the influence of the small dimension in thin samples can be important as discussed in chapter 8.

dendritic growth of some materials (where its effect was studied theoretically [49], in simulations [50], and experimentally on Pivalic Acid [51]) and under rapid solidification conditions [52]. In rapid solidification additional freezing point depression is caused by non-equilibrium effects such as solute trapping or solute drag [48].

For binary alloy directional solidification the solute concentration field and the thermal field can be described by the **one-sided model** [53, 54]. The thermal diffusion coefficient D_{th} is assumed equal in the solid and in the liquid[3], which ensures a linear temperature gradient equal to the applied gradient G across the solid-liquid interface. Since D_{th} is usually much larger than the chemical diffusion coefficient D, latent heat effects are small and also neglected in the one-sided model (at very low concentrations latent heat has to be taken into account, because this small effect starts to influence dynamical instabilities [55]). Solute diffusion in the solid is neglected. In the liquid, the solute concentration $C(x, z, t) = C(\vec{x}, t)$ obeys the diffusion equation in the frame of reference fixed in the laboratory:

$$\left(\frac{\partial}{\partial t} - V_P \frac{\partial}{\partial z}\right) C(\vec{x}, t) = D\nabla^2 C(\vec{x}, t) \tag{2.2}$$

The interface at $\vec{x} = (x, z_0(x))$ introduces additional boundary conditions (with C for the liquid and C_S for the solid):

$$C_S(\vec{x}_0, t) = kC(\vec{x}_0, t) \tag{2.3}$$

The partition coefficient k is the ratio of equilibrium concentrations on the solid and liquid sides of the interface. In the small concentration limit k is independent

[3]this is approximately the case in many metallic and organic alloys

of solute concentration. In the following it is assumed that $k < 1$ which is true for most alloys. The basic equations also hold for $k > 1$, only minor changes in notation would be needed. Conservation of solute yields the other boundary condition:

$$\frac{k-1}{k} C_S(\vec{x}_0, t)\vec{V} \cdot \vec{n} = -D\nabla C(\vec{x}, t)|_{\vec{x}_0} \tag{2.4}$$

Equations 2.1 - 2.4 are first solved assuming a flat one-dimensional interface ($\kappa = 0$) to find the one-dimensional steady- state concentration field $C_0(z)$:

$$C_0(z) = C_\infty \left(1 + \frac{1-k}{k} \exp\left(\frac{-2(z-z_I)}{\ell}\right)\right) \tag{2.5}$$

where C_∞ is the background concentration in the liquid far away from the advancing interface and z_I is the steady state position of the interface. Equation 2.5 predicts that at steady state $C_0(z_I) = C_\infty/k$ and that $C_0(z)$ decays exponentially from $C_0(z_I)$ to C_∞ with a decay length $\ell = 2D/V_P$. This *spike* (or snowplow) of rejected solute moves ahead of the advancing interface. (The decay length ℓ is defined such that a solute spike of triangular shape with length ℓ and maximum height C_∞/k would contain the amount of solute present in the actual spike.)

2.2 Planar Interface Stability

2.2.1 Mullins-Sekerka Linear Stability Analysis

The central theoretical approach which has been followed in virtually all analyses of data obtained from directional solidification experiments is the linear stability

analysis first employed by Mullins and Sekerka in 1964 [15]. The Mullins-Sekerka linear stability analysis begins with the steady-state concentration field Eqn. 2.5 and adds an infinitesimal sinusoidal modulation with wavevector q:

$$C(x,z,t) = C_0(z,t) + \delta C \cos(qx) e^{-k_q z + a_0(q)t} \tag{2.6}$$

A similar modulation is assumed for the interface position:

$$z(x,t) = z_\infty + \xi_q(t)\cos(qx) = z_\infty + A_0 \cos(qx) e^{a_0(q)t} \tag{2.7}$$

Here δC and A_0 are small modulation amplitudes, k_q is the inverse decay length of the concentration field modulation ahead of the interface, and $a_0(q)$ is the *linear growth coefficient* of the modulation amplitude. This interface and concentration field ansatz is then put into the governing equations 2.1 - 2.4 which are solved for k_q and the linear growth coefficient $a_0(q)$:

$$a_0(q) = \left[d\xi_q(t)/dt\right]/\xi_q(t) \tag{2.8}$$

The main results of this linear stability analysis, shown schematically in figure 2.2, are:

(a) For pulling speeds V_P below a critical value V_C, $a_0(q) < 0$ for all q and the interface is therefore stable against all deformations. At high concentrations, V_C is given approximately by the constitutional supercooling criterion [22, 23]:

$$V_C = \frac{GDk}{(1-k)mC_\infty} \tag{2.9}$$

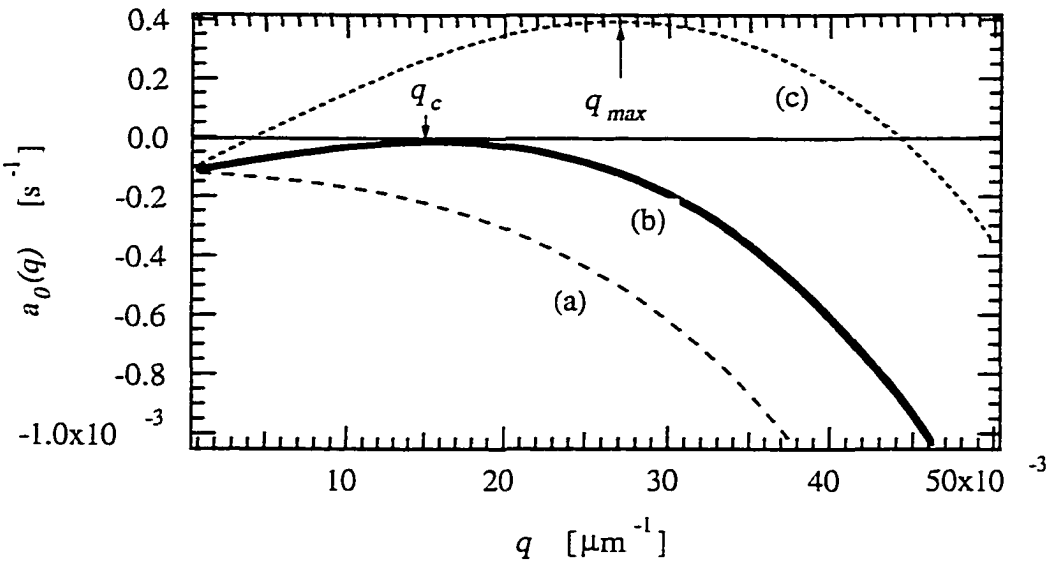

Figure 2.2: The Mullins-Sekerka linear growth coefficient $a_0(q)$ vs q at steady state for (a) $V_P < V_C$, (b) $V_P = V_C$, and (c) $V_P > V_C$. These curves can also represent the evolution of $a_0(q,t)$ with time for $V_P > V_C$ as the concentration field evolves towards steady state.

(b) When $V_P = V_C$, the interface is marginally stable ($a_0(q_C) = 0$) for a single wavevector q_C ($q_C \approx (D/V_C)^{-2/3} d_0^{-1/3}$, see [56]).

(c) For $V_P > V_C$, the interface is unstable against a range of wavevectors, i. e. there is a band of unstable modes for which $a_0(q) > 0$.

In the $a_0(q)$ vs q curve (c), for $V_P > V_C$, the range of unstable modes is set by the two neutral stability points where $a_0(q) = 0$, while the maximally unstable mode q_{max} defined by the maximum of the $a_0(q)$ vs q curve should grow most rapidly. The calculated neutral stability curve with its maximally unstable mode has been the main tool for comparing experiments and theory. In general, however, the wavevector q_{init} of the initial modulation observed experimentally does not correspond to the calculated maximally unstable mode q_{max}. Typically, q_{init} is

smaller than q_{max} by a factor of ~ 5 [57]. There are several limitations to this method of comparing experimental data with predictions of the linear stability analysis which could explain the disagreement.

1. While the Mullins-Sekerka stability analysis is performed assuming a steady-state planar interface, if the pulling speed V_P is well above V_C the interface may destabilize long before steady state is reached with a different q_{max} than that at steady state.

2. The results of the Mullins-Sekerka linear stability analysis beginning with Eq. 2.7 are equivalent to an equation of motion for $\xi_q(t)$:

$$\frac{d}{dt}\xi_q(t) = a_0(q)\xi_q(t) \tag{2.10}$$

Note, however, that if $\xi_q(t=0) = 0$, then from Eq. 2.10 $\xi_q(t) = 0$ for all $t \geq 0$ even if $a_0(q)$ is positive. The linear stability theory therefore does not provide a complete equation of motion for $\xi_q(t)$. An initiation mechanism, e.g. thermal noise effects, should be included, as discussed in the next section.

3. While the thermal diffusion field can be ignored for high impurity concentrations, this approximation becomes less valid as C_∞ decreases and thermal effects become important [55, 58]. Latent heat that has to be transported away from the growing solid modifies the temperature field at the interface. Because the thermal diffusion constant is several orders of magnitude larger than the solute diffusion constant, this effect only becomes important, if the

instability occurs at high speeds (i.e. at very low solute concentrations), when enough latent heat is generated.

4. Linear stability analysis does not fully describe the instability. Nonlinear terms must also be included to obtain steady-state non-planar solutions [59, 60] and to determine if the initial instability is subcritical or supercritical, i.e. with or without hysteresis [55].

The experiments presented in this thesis and in [2] show that limitations (1) and (2) have to be overcome for a self consistent calculation of the initial instability of a planar front in all cases, while limitations (3) and (4) need only be considered at small concentrations or close to the critical pulling speed.

2.2.2 Warren - Langer Time Dependent Linear Stability Analysis

Warren and Langer (WL) [39] reanalyzed the pattern-formation phenomenon of directional solidification with a procedure based on the Mullins-Sekerka linear stability approach, but without the approximations (1) and (2). WL analyzed the dynamics beginning from the time that pulling is initiated, and followed the motion of the interface $z_0(t)$ and the evolution of the concentration field $C(x, z, t)$. They applied the Mullins-Sekerka stability analysis dynamically as the concentration field evolves with time rather than assuming steady state.

Taking $z_0 = 0$ as the position of the interface of an undoped sample in equilib-

rium, the initial ($t = 0$) and steady-state ($t \to \infty$) values of $z_0(t)$ are:

$$z_0(t = 0) = z_\infty = \frac{-mC_\infty}{G} \tag{2.11}$$

$$z_0(t \to \infty) = \frac{-mC_\infty}{kG} \tag{2.12}$$

For the planar interface WL assumed that the concentration field in the liquid is given by

$$C(z,t) = C_\infty + (C(z_0,t) - C_\infty) \exp\left(\frac{-2(z(t) - z_0(t))}{\ell(t)}\right) \tag{2.13}$$

i.e., an exponential decay with a time-dependent decay length $\ell(t)$. At steady state, Eq. 2.13 becomes identical to Eq. 2.5 [i.e. $\ell(t \to \infty) = \frac{2D}{V_P}$]. This assumption simplifies the numerical calculations significantly since the problem can now be reduced to two coupled differential equations for $\ell(t)$ and $z_0(t)$ (see ref. [39]):

$$\dot{z_0}(t) = f_1(z_0(t), \ell(t)) = \frac{2D(z_0(t) - z_\infty)}{\ell(t)(1-k)z_0(t)} - V_P \tag{2.14}$$

$$\dot{\ell}(t) = f_2(z_0(t), \ell(t)) = \frac{4D(z_\infty - kz_0(t))}{\ell(t)(1-k)z_0(t)} - \frac{\ell(t)}{z_0(t) - z_\infty}\left(\frac{2D(z_0(t) - z_\infty)}{\ell(t)(1-k)z_0(t)} - V_P\right) \tag{2.15}$$

These equations can be solved numerically, with results as illustrated in Figs. 2.3 and 2.4.

The ad-hoc assumption of an exponential concentration profile with time dependent characteristic length was shown to give essentially the same results for $z_0(t)$ and $\ell(t)$ as a full numerical calculation [61]. The WL calculations deviate from the full numerical calculation only after the planar front overshoots the steady state planar interface position at speeds above the critical pulling speed. The amplitude and frequency of the subsequent damped oscillatory approach to steady

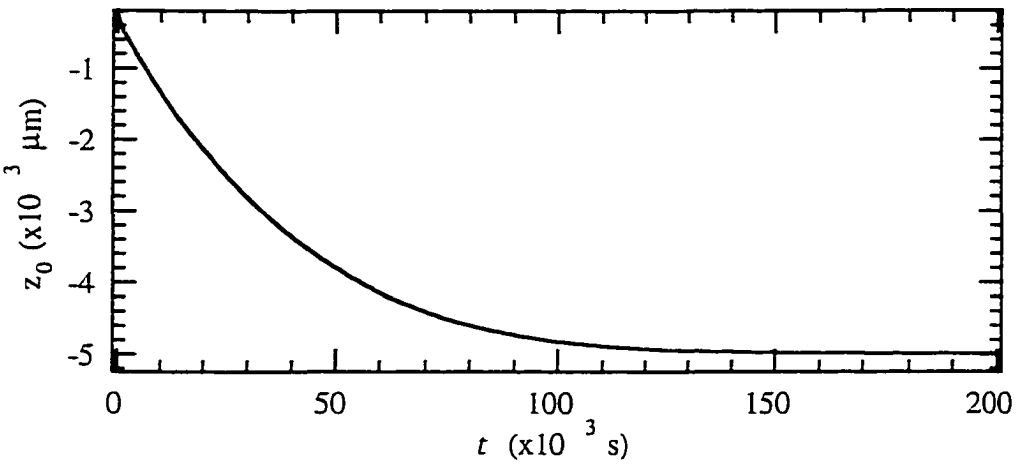

Figure 2.3: Solution of the Warren-Langer equations for $z_0(t)$. The parameters used correspond to the experiment shown in Fig. 4.4 (SCN/Coumarin 152 at $V_P = 0.549\mu$m/s $\approx 6V_C$, $C_\infty = 0.30$wt%, $G = 20.2$K/cm).

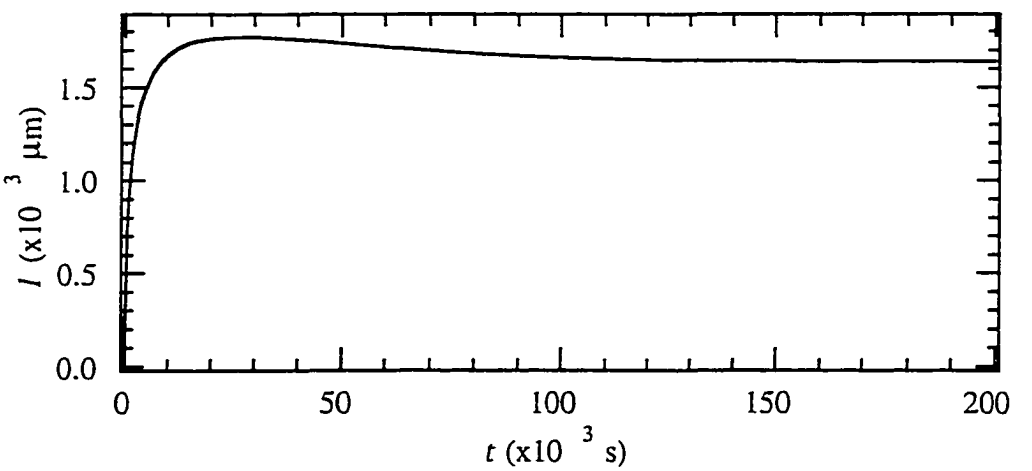

Figure 2.4: Solution of the Warren-Langer equations for $\ell(t)$. The parameters used correspond to the experiment shown in Fig. 4.4 (SCN/Coumarin 152 at $V_P = 0.549\mu$m/s $\approx 6V_C$, $C_\infty = 0.30$wt%, $G = 20.2$K/cm).

state differs slightly in the WL analysis and the full numerical analysis [61]. These deviations become observable only well above the critical speed V_C, but in this case the planar interface goes unstable before the overshooting can occur. The WL approximation therefore holds for all observable planar interfaces.

WL next solved linearized (Langevin) equations of motion for interface modulations $\xi_q(t)$:

$$\xi_q(t) = a_0(q,t)\xi_q(t) + \eta_q(t) \tag{2.16}$$

Equation 2.16 differs from Eq. 2.10 in two ways. First, the inclusion of the random thermodynamic (Langevin) fluctuating force term $\eta_q(t)$ provides an initiation mechanism for the instability; second, the linear growth coefficient $a_0(q,t)$ is time-dependent, computed from the instantaneous concentration field of Eq. 2.13 rather than from the steady-state result. In order to solve equation 2.16 the WL-approximation of a (time dependent) exponential concentration profile is essential, since it provides a value for $\ell(t)$, which allows the use of the MS linear stability analysis with time dependent $z_0(t)$ and $\ell(t)$ instead of their steady state values.

Numerical solution of Eq. 2.16 for all q predicts how the pattern will evolve with time. The instability is assumed to occur for a two dimensional interface, to allows comparison to most experiments, where the initial instability wavelength is smaller or equal the sample width. Important results are verified experimentally in chapter 4:

- Following the start of the pulling motor even well above V_C, $a_0(q,t)$ is initially negative for all q.

- At pulling speeds above V_C, $a_0(q,t)$ crosses over from negative to positive for one q at a well defined time after crystal growth is started. This time will be called **marginal stability time** t_i in this thesis.

- After t_i the instability takes time to build up sufficiently to become visible. WL introduced a **crossover time** t_0, distinct from t_i, at which the initial modulation amplitude reaches the same magnitude as the mean wavelength λ_0, and the (approximate) end of the linear regime is reached. Since $a_0(q,t)$ increases with time the amplitude of interface modulations grows faster than exponentially. The mean wavelength of those modulations, on the other hand, decreases only slowly. Both t_0 and λ_0 are thus well defined quantities, as illustrated in figure 4.10.

2.3 Numerical Methods beyond the Planar Interface

Analytic solutions for any steady-state pattern beyond the planar interface are difficult to calculate. The solution of the differential equations for the solute (and temperature) field in the solid and the liquid phase is determined by the boundary conditions at the a priori undetermined solid-liquid interface position. However, the movement of the interface in turn is determined by the differential equations for the solute (and temperature) field (Stefan problem).

2.3.1 Boundary Integral Calculations

For numerical computations the system of differential equations (2.1 - 2.4) can be replaced by an equivalent single integro - differential equation (for a detailed derivation of the integro-differential equations see e.g. Caroli, Caroli and Roulet([52], appendix B) or Kessler, Koplik and Levine [33]). To obtain the integral, the interface is treated as a source of solute: The interface at $\vec{x_B}$ rejects the solute amount $S(\vec{x_b}, t) \sim C(\vec{x_B}, t)(1-k)$. The solute concentration in the liquid is then the stationary solute concentration C_∞ plus the superposition of interface sources along the whole interface at all previous times, calculated using the retarded Greens function of the solute diffusion equation in the liquid: (see ([52], Appendix B) for the complete integro-differential equation)

$$C(x,z,t) = C_\infty + \int_{-\infty}^{t} dt' \int_{\text{Interface}} d\vec{x_B} G(x,z,t;\vec{x_B},t') S(\vec{x_B},t') \qquad (2.17)$$

$$C(x,z,t) = C_\infty + \int_{-\infty}^{t} dt' \int_{\text{Interface}} d\vec{x_B} G(x,z,t;\vec{x_B},t') S(\vec{x_B},t') \qquad (2.17)$$

In quasistatic approximation the Greens function of the diffusion equation is given by:

$$G(\vec{x};\vec{x_B}) = \int\int dk_z dk_x \frac{e^{ik_z(z-z_B)} e^{ik_x(x-x_B)}}{k_x^2 + k_z^2 + 2iV_P k_z/D} \qquad (2.18)$$

Equation 2.17 can be solved analytically for special cases, but it is most useful for numerical simulations, since it can be used to compute the evolution of the interface shape from given initial conditions. The best approach for finding stable steady state shapes appears to be [62], to first find all steady state cell shapes numerically using the quasistatic Greens function and to subsequently test their stability through linear perturbations with all perturbation wavelengths applied to

the full time dependent integro- differential equation.

Two main problems limit the boundary integral method. A sharp interface between solid and melt is assumed, which neglects the finite size boundary layer and limits numerical simulations to small grid sizes and therefore mostly to cellular patterns. In addition, the model does not include the experimental observation that portions of the interface can merge, for example inside the sidebranch structure far behind a dendrite tip.

2.3.2 Phase-Field Model Simulations

Phase field models are a new numerical approach that overcomes the limitations of the boundary integral method mentioned above (for a review, see [63, 64]). The solid and liquid phase are described by an additional variable, the phase field Φ. This variable can be seen as an order parameter for the material; the solid is described by $\Phi = -1$ (or 0) and the liquid by $\Phi = 1$. The phase is derived from a *phenomenological* free energy functional $\mathcal{F}$:

$$\mathcal{F} = \int d\vec{r}\left(W^2 |\nabla\Phi|^2 + f(\Phi, C)\right) \tag{2.19}$$

The first term containing $|\nabla\Phi|$ models the surface tension, and surface tension anisotropy ($W = W(\vec{n})$) in some newer models [50]). The second term $f(\Phi, C)$ models the free energy of the bulk material. In order to ensure that local entropy production is positive, an entropy functional was proposed by Penrose and Fife [65] which is used in some simulations [63, 66, 67]. In all models the phase field

obeys the principle of minimization of free energy (or maximization of entropy, not shown):

$$\tau \frac{\partial \Phi}{\partial t} = -\frac{\delta \mathcal{F}}{\delta \Phi} \tag{2.20}$$

Here τ is the inverse of a mobility parameter for the phase. The phase field equation couples to the diffusion field through $f(\Phi, C)$, and the diffusion equation couples to the phase, since it has to be modified to be valid across the interface in both the solid and the liquid using the new phase parameter Φ. Now we have two coupled differential equations, one for the solute field and one for the phase field, but no moving boundary conditions. However, the width of the solid-liquid interface is entering the problem as an additional variable. The expressions for $f(\Phi, u)$ and $W(\vec{n})$ in the free energy equation depend on the phase-field model used, but all models have to reduce to the free boundary equations (2.1 - 2.4) in the sharp interface limit.

The phase-field method was introduced by by Langer [68], and models were developed by Kobayashi [69, 70] , by Penrose and Fife [65, 71] , and by Wang *et al* [67, 72]. In the first simulations, the two differential equations were generally solved with a finite difference technique on a fixed grid. This limits computations to two dimensions and to large interface widths [63]. All early simulations also had to keep the kinetic undercooling term large. The number of grid points necessary can be reduced through an adaptive grid method, developed by Braun and Murray [73], but the kinetic undercooling term prevented quantitative comparisons to theories and experiments on directional solidification, where that term is often negligible.

One recent model by Karma and Rappel [74] introduces anisotropy in both W and τ and uses equations for $f(\Phi, u)$, $W = W(\vec{n})$ and $\tau = \tau(\vec{n})$ that eliminate the need to keep any kinetic undercooling in the sharp interface limit and allow for a computational grid significantly larger relative to the dendrite shape without loosing validity. These simulations make quantitative three-dimensional calculations possible [75, 76] and permit simulations of large cellular or dendritic arrays in two dimensions, which can address the problem of pattern selection. This makes a direct comparison of directional solidification simulations and experiments possible. In chapter 7 we will compare new experiments on doublet cellular patterns to phase-field model simulations by Kopczyński, Rappel and Karma which are included as appendix C.

2.4 Cellular Patterns

Above V_C, at intermediate crystal growth speeds, cellular arrays develop after the planar front has gone unstable. At pulling speeds close to the threshold shallow cells are observed. Since the linear stability analysis predicts exponential growth of unstable modes, additional terms are needed in the Landau equation 2.10 to model a restabilisation of a cellular front:

$$\frac{d}{dt}\xi_q(t) = a_0(q)\xi_q(t) + a_1(q)\xi_q^3(t) + ... \tag{2.21}$$

The coefficient a_1 indicates the nature of the planar-cellular bifurcation:

- $a_1 < 0$: Supercritical bifurcation: Steady state finite amplitude cellular solutions with $\xi = (-a_0/a_1)^{1/2}$ exist, even for arbitrarily small amplitudes.

- $a_1 > 0$: Subcritical bifurcation: Higher order terms are necessary for steady state non-planar solutions. A minimum amplitude for steady state cellular solutions exists. For $a_0 < 0$ both the planar and the cellular interface are stable steady states. A sufficiently large perturbation can therefore lead to a spontaneous planar to cellular transition while $a_0 < 0$.

This analysis assumes that all modes are independent and do not couple to each other, so it is only valid as long as the range of unstable modes is small, i.e. close to the critical speed V_C. The coefficient a_1 can be calculated analytically (see Wollkind and Segel [77]). A stability analysis of small amplitude cells shows that a continuous range of stable cellular spacings exist, limited for small and large cell spacings by the long wavelength Eckhaus instability [77, 78, 79].

At higher speeds the weakly nonlinear analysis is no longer sufficient as cells become deep. The shape of large amplitude cells can be calculated from matching expansions [80] or numerically from boundary integral calculations or from phase-field model simulations (see section 2.3).

The stability of those shapes has to be confirmed through separate calculations, from the response of the shape to small perturbations. Ten generic instabilities exist for one-dimensional interfaces. They can be derived analytically from symmetry arguments in space (symmetric or antisymmetric, with the same, double or an irrationally related period) and in time (stationary or oscillatory). (See Coullet

and Ioos [81] for the derivation and Flesselles *et al* [47] for an explicit list of these instabilities.)

Recent theoretical [82] work using matching expansions and experiments [42, 83] have shown that steady state cellular patterns can exist for a continuous band of cell spacings at higher pulling speeds. The stability range was found to be limited by oscillatory instabilities [84], which lie within the stable Eckhaus band at higher speeds [62]. The stability range was found to increase dramatically with surface tension anisotropy [62]. Without anisotropy, uniformly spaced cellular arrays were found to be unstable against oscillatory instabilities, except close to V_C. New phase-field model simulations [85] indicate that uniform cellular arrays form spontaneously during the planar-cellular transition only for very large surface tension anisotropy, i.e. natural selection of a uniform pattern requires a large band of stable patterns.

2.5 Dendritic Patterns

2.5.1 Shape of One Dendrite

At higher pulling speeds cells start to develop sidebranches and a cell to dendrite transition takes place. It is not yet clearly established, if cells and dendrites are one continuous family of solutions that differs only through a sidebranching instability, or if they represent qualitatively different solutions. The current understanding of the cell-dendrite transition and new experiments that could help to resolve the

question will be discussed in chapter 6.

Another (often neglected) transition that takes place in many experiments in this range of pulling speeds is the transition from a two-dimensional cell tip shape to a three dimensional cell tip shape, when the cell tip dimension becomes smaller than the sample width. For dendrites, a three dimensional dendrite tip will therefore be assumed in the following discussion.

When surface tension is neglected, shape preserving (i.e. steady state) interface profiles can be found under isoconcentrate boundary conditions. The resulting shape is a parabola of radius ρ, as first calculated by Ivantsov [86].

$$\frac{C_T - C_\infty}{C_T(1-k)} = Pe^P \int_P^\infty \frac{e^{-z}}{z} dz \tag{2.22}$$

Here C_T is the solute concentration in the liquid at the dendrite tip and $P = \rho V_P/2D$ is the Peclet number (the ratio of tip radius and solute diffusion length). This equation determines the relationship between ρ and $C_T \sim z_o(tip)$, and leads to a continuous family of possible dendrite operating states. The physical force selecting an operating state seems to be missing in the Ivantsov calculation, and an analysis shows that this parabolic shape is unstable against tipsplitting unless surface tension is introduced as a stabilizing force.

A linear stability analysis including surface tension [87, 88, 89] found a band of stable states, and the marginally stable states showed agreement with experimental data. The marginal stability hypothesis then assumed that the marginally stable state is selected in experiments. Even though the theory leads to the same equation for σ^* (which characterizes the dendrite operating state) as microscopic solvability

(discussed below, see Eq. 2.23), it does not capture the dependence of σ^* on the material as observed in experiments [90]. In addition, local models of solidification showed that surface tension can not be introduced as a small parameter in a stability analysis, because the perturbation is singular. A more detailed description of the interface is needed, now surface tension anisotropy is added to the equations.

Microscopic solvability theory[4], developed by Kessler, Koplik and Levine [33] and by Langer [79], captures the dependence of σ^* on the surface tension anisotropy. Microscopic solvability theory predicts that the operating state of a dendrite is given by the equation:

$$\sigma^*(\epsilon) = \frac{2Dd_0T_M}{\rho^2 V_P m C_T (1-k)} \tag{2.23}$$

$\sigma^*(\epsilon)$ is a function of the surface tension anisotropy ϵ only, constant for a given material ($\sigma^* \sim \epsilon^{7/4}$ in two dimensions [79] and three dimensions [91] for very small anisotropies). Boundary integral calculations by Misbah *et al* [92] found agreement with the scaling of $\sigma^*(\epsilon)$ with ϵ in two dimensions. New, quantitatively correct phase-field model simulations [75, 76] in three dimensions find quantitative agreement with microscopic solvability theory in three dimensions, and also the predicted dependence of σ^* on the surface tension anisotropy.

Up to here sidebranches have been neglected. Theoretical calculations indicate that sidebranches are triggered through noise at the tip which is amplified along the side of the dendrite [93]. Experiments by Williams *et al* [43], in which

[4]Microscopic solvability theory was derived in two dimensions, but recent calculations [91] showed that the structure of solvability theory remains valid in three dimensions

a periodic laser perturbation is applied to the dendrite tip, measured the amplitude of sidebranches behind the tip for different frequencies and found qualitative agreement with that theory.

2.5.2 Interdendritic Spacings (Warren - Langer Stability Analysis)

The interdendritic spacing in directional solidification is a parameter of great practical importance, yet it is not included in the theoretical descriptions above. Warren and Langer carried out a stability analysis of a dendritic array undergoing directional solidification in order to determine if a selection mechanism for the interdendritic spacing exists [39, 40]. They first set up a periodic array of dendrites consistent with both microscopic solvability theory and the macroscopic equations for the solute diffusion field. As shown in Fig. 2.5, the periodic array, with interdendritic spacing λ_1, is given a periodic modulation of tip positions in the direction of growth, with modulation wavelength λ. The stability analysis yields the linear growth coefficient $a_0(\lambda)$ of the modulation amplitude.

Figure 2.6 shows the result for $a_0(\lambda)$ at three different growth speeds. At sufficiently high V_P the array is stable against modulation of any λ since $a_0(\lambda) < 0$ for all λ. As V_P is reduced, the initial instability $a_0(\lambda) = 0$ occurs for $\lambda_1/\lambda = \pm 0.5$, corresponding to spatial period doubling. At yet lower V_P, a large range of λ becomes unstable, but spatial period doubling remains the maximally unstable mode. Thus the analysis indicates that a dendritic array of given λ_1 is stable over

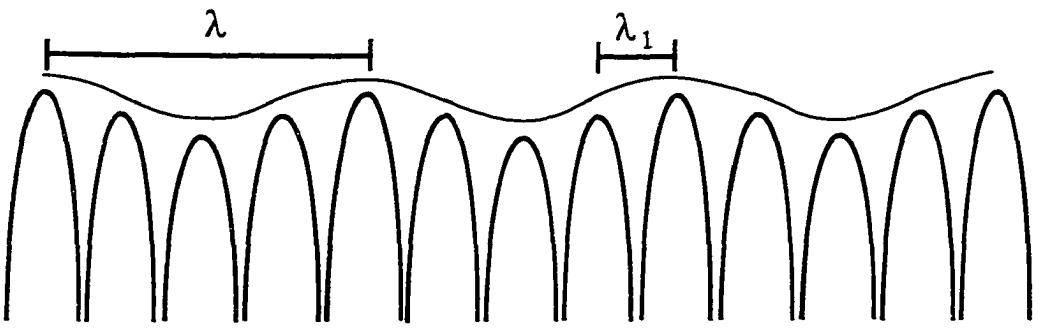

Figure 2.5: Schematic of the stability analysis of a dendritic array. A periodic array with spacing λ_1 with a sinusoidal modulation of tip positions with modulation wavelength λ.

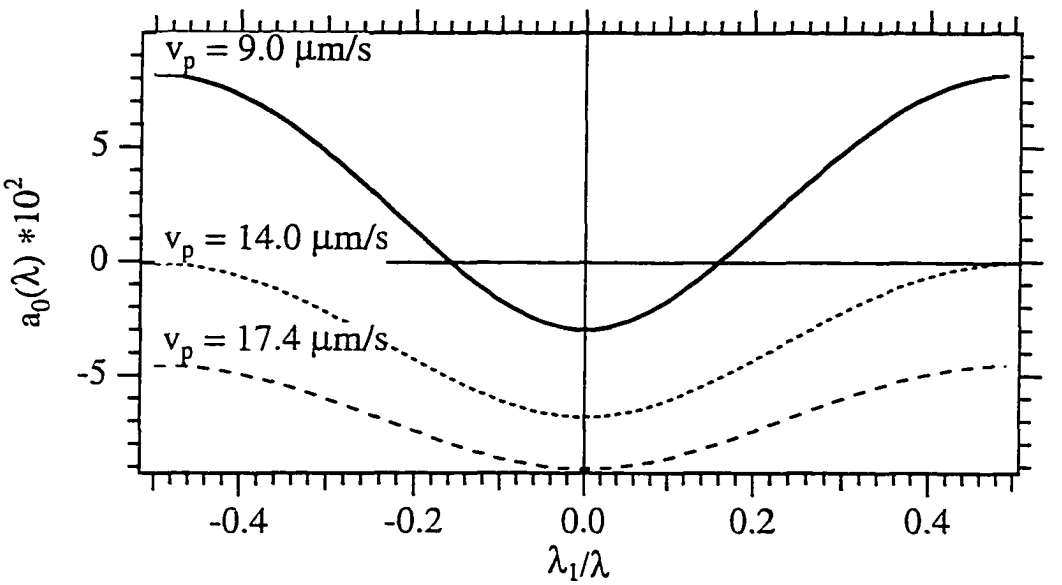

Figure 2.6: Stability analysis of a periodic dendritic array with spacing λ_1 with a sinusoidal modulation of tip positions with modulation wavelength λ. Result of the linear stability analysis of Ref. [40] for $C_\infty = 0.43$wt% with $\lambda_1 = 170\mu$m. For $V_P = 17.4\mu$m/s the array is stable for all λ: for $V_P = 14.0\mu$m/s it is marginally unstable for $\lambda = 2\lambda_1$; for $V_P = 9.0\mu$m/s it is unstable for $2\lambda_1 \leq \lambda \lesssim 6\lambda_1$.

a large range of V_P with a lower bound, i.e. that there is no selection mechanism. Presumably there is also an upper bound on V_P set by either a tip-splitting instability, or by development of tertiary arms into dendrites [36], but this instability has not yet been investigated analytically. The same analysis for fixed V_P with different λ_1 shows that this instability sets a lower bound for the range of stable λ_1 values.

Chapter 3

EXPERIMENTAL PROCEDURES

The experiments were carried out in a high precision computerized directional solidification apparatus (section 3.1.1). The binary alloy sample (section 3.2) is filled into thin glass capillaries and inserted into the temperature gradient of the directional solidification apparatus. The system is mounted onto a videomicroscope and the solid-liquid interface is observed through the videocamera (section 3.1.2). Finally, the shape of the interface is extracted using pattern recognition algorithms (section 3.5).

3.1 Directional Solidification Apparatus

3.1.1 Temperature Gradient Microscope Stage

The standard temperature gradient microscope stage designed by Hunt *et al* [25] and used in most experiments on directional solidification of transparent organic materials was modified for our experiments to improve the thermal contact of a moving sample.

The glass capillary sample cell is glued to a holder attached to a translation stage that is driven with a computer-controlled DC motor. The glass capillary extends into an oil-filled stainless steel tunnel that has two sapphire windows to allow visual observation of the interface. The tunnel is inserted into copper hot and cold blocks and brought into good thermal contact with both so that a linear temperature gradient is established in the tunnel between the two blocks. Light mineral oil inside the tunnel exposes the glass capillary (which is suspended in the middle of the tunnel) to the applied temperature gradient, assures spatial uniformity of heat conduction, and also approximately matches the refractive index of the glass capillary. The whole system has a plastic cover for thermal insulation. A schematic of the setup is shown in figure 3.1.

The hot block is held at constant temperature by an electronic proportional temperature controller (YSI Model 72, Yellow Springs Instruments, Yellow Springs, OH). The range of available temperatures is 30°C to 120°C with an accuracy of ±0.01K. The cold block is cooled with a water bath (Lauda RM6, Lauda

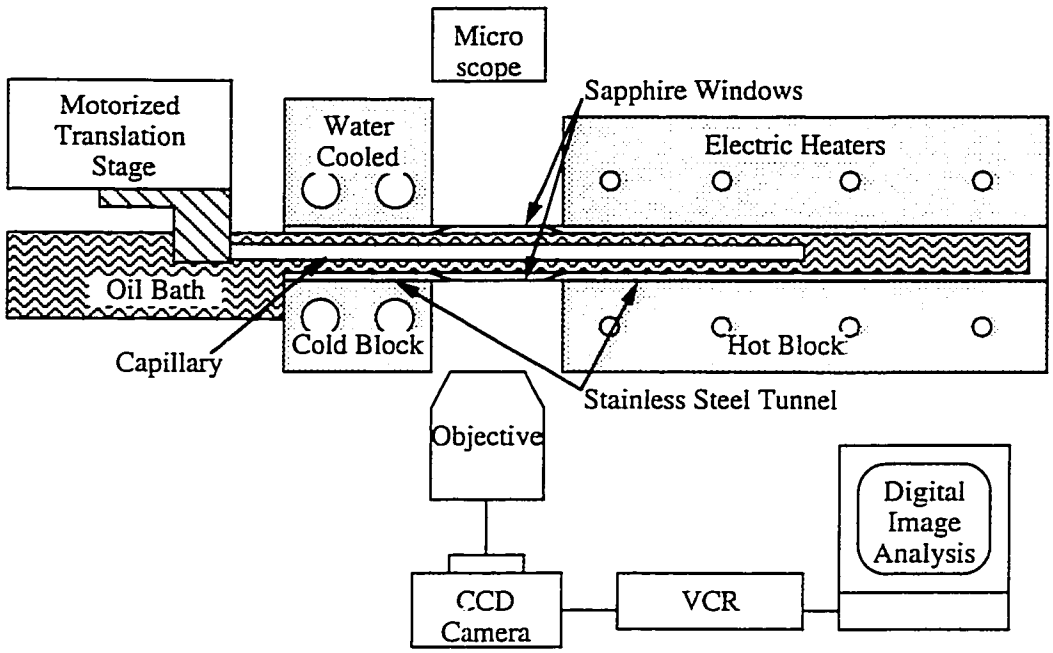

Figure 3.1: Schematic of the experimental setup

GmbH, Lauda-Königshofen, Germany). The available temperature range is 10°C to 80°C with an accuracy of ±0.01K. We also measured the actual temperature profile in the tunnel and found a linear temperature gradient across the region of observation. Measurements with a thermocouple inside a glass capillary showed that the temperature gradient does not change with a change in pulling speed, permitting accurate determination of the interface temperature both in equilibrium and while pulling.

With the motor drive, pulling speeds in the range from 0.05μm/s to more than 100μm/s can be selected. The motor (MicroMo Electronics Inc., St. Petersburg, FL) is controlled by a 386 PC and held at constant speed with an optical decoder with an accuracy of ±0.5%. The pulling speed can be set in 127 increments and the motor reaches the selected pulling speed V_P in approximately two msec.

The motor is attached through a gearhead to the translation stage (CTC 462-1S by Micro Kinetics, Laguna Hills, CA), which controls the sample position to within 0.5μm.

3.1.2 Videomicroscopy

The whole setup is mounted on the stage of a Nikon inverted Diaphot microscope. In most experiments a large aperture 4× objective from Nikon is used. (An additional 10× objective in the eyepiece gives a total magnification of 40×.) The microscope is operated as a bright field microscope or phase-contrast microscope to achieve maximum interface contrast relative to the background.[1] Images of the experiments are captured with a Dage-MTI (Michigan City, IN) CCD 72 camera with a resolution of 480 × 640 points (pixels) with 256 greyscales.[2] Data acquisition is carried out with a Macintosh IIci computer equipped with a Quickcapture DT-2255 frame grabber interface board (Data Translation,Marlboro,MA) that can capture images at a rate of up to 30 frames per second. The video images are either directly analyzed on the computer or stored on a Hi-Fi Super-VHS HR-S5200U

[1]The oil in the temperature gradient channel sometimes contains micron-size particles often from the insertion of the samples into the oil channel. It is very difficult to completely remove these dirt spots, and if they are present near the interface they can prevent phase-contrast microscopy. The dark spots in many images shown in this thesis are such dust particles, not contaminations inside the sample capillary.

[2]Parallel to the temperature gradient along the z-axis 1pixel = 3.17μm; perpendicular to the temperature gradient along the x-axis 1pixel = 3.29μm.

VCR (JVC). The solid-liquid interface is then extracted as described in chapter 3.5.

3.2 The Alloy Model System

3.2.1 Material Characterization: Organic Crystal - Laser Dye

The dilute binary alloy model system used is the transparent organic crystal Succinonitrile (SCN) (Fluka, Milwaukee, WI) which is widely used in directional solidification studies [94, 20, 31, 35], since SCN was found to have crystal growth properties similar to metallic alloys. The material parameters of SCN have been accurately measured [95] (see Table 3.1). Usually acetone or ethanol is used for the second component (solute). However, since both SCN and acetone are transparent, the solute concentration field cannot be directly observed.

Following preliminary unpublished experiments of Bechhoefer, Heslot and Libchaber who introduced a laser dye as the solute to produce a visible solute field, we have employed SCN with the laser dye coumarin 152 (C152) (Sigma,St. Louis, MO) as the solute[3]. The C152 is added in small concentrations of < 0.5wt%. In

[3]Fluorescein appears to be the first dye used in transparent organic crystals. Jackson (see [96] fig. 5) used it in the organic crystal cyclohexanol to make coarsening and the associated solute redistributions visible.

addition to being visible under the microscope, C152 has a broad absorption peak in the near UV ($\lambda_{Max} = 394$nm), which allows for a thermal perturbation of the sample through absorption of UV light and makes a direct determination of the concentration possible through Fluorescence measurements.

All material parameters necessary for a quantitative comparison to theoretical predictions have been carefully measured for the SCN-C152 system (see table 3.1).

3.2.2 Sample Preparation

The preparation of SCN/C152 samples is difficult since SCN degrades quickly under contact with air or epoxies, including Torrseal (Varian, Lexington, MA). Compatible materials for sample cells are austenitic steel 304 and borosilicate glass [99]. The addition of C152 causes even quicker degradation of the sample under contact with air or epoxies. A long sample lifetime can thus only be achieved, when contact with air is prevented through vacuum distillation and when the sample is filled into suitable cells under vacuum.[4]

First, SCN with 99% purity was four times vacuum distilled ($P < 200$mTorr). The pure SCN was then mixed under vacuum with C152 powder at concentrations from 0 to 0.45wt%. The mixture was filled under vacuum into precleaned glass

[4]Preparing the sample in an inert gas atmosphere also poses problems, because residual gas impurities build up ahead of the advancing interface during crystal growth and can eventually nucleate into gas bubbles ahead of the growing crystal [100, 101].

Succinonitrile-Coumarin152		Unit	Ref
Segregation coefficient k	0.05		this work
Liquidus slope m	5.43	K/mol%	this work
Diffusion Constant D	450	$\mu m^2/s$	this work
Interfacial free energy γ (SCN)	8.95	$10^{-15}J/\mu m^2$	[95]
Melting temperature T_M (SCN)	331.24	K	[95]
Latent heat (SCN)	4.627	$10^{-11}J/\mu m^3$	[95, 97]
Thermal conductivity (solid SCN)	5.36	10^{-4}Cal/cms	[95]
Thermal conductivity (liquid SCN)	5.32	10^{-4}Cal/cms	[95]
Surface tension anisotropy ϵ_4	0.55%		[90]
Molecular weight (SCN)	80.09	g/mol	[95]
Molecular weight (C152)	257	g/mol	[98]
Density (solid SCN)	1.016	g/cm^3	[95]
Density (liquid SCN)	0.970	g/cm^3	[95]

Table 3.1: Selected material parameters of the model alloy Succinonitrile - Coumarin 152

capillaries with inner dimensions 0.1 × 2.0 × 300mm (Vitro Dynamics, Mountain Lakes, NJ). The capillaries were flame sealed while connected to the vacuum pump. The detailed steps of the sample preparation process are described in appendix B.

The sample height of 100μm is chosen to allow one row of cells or dendrites to form. Since our objective is to measure cellular or dendritic spacings, it is necessary to observe the widest possible solid-liquid interface patterns. Unfortunately, the width of commercially available capillaries with a height of 100μm is limited to 2mm. One alternative would be to use microscope slides with spacers, but all epoxies used lead to a degradation of the sample. In future experiments it may be possible to join microscope slides on all sides using low melting point glass powder and to fill the cell through an attached capillary that fits the existing filling setup.

Three samples were produced at the same time from each mixture. As a test for other impurities one sample of pure SCN was directionally solidified at a high pulling speed ($V > 10\mu$m/s) with a low temperature gradient ($G < 5$K/cm) where a small impurity concentration should produce an instability ("Chester test"). No instabilities occurred, and it was therefore assumed that any remaining impurities in the doped samples would not affect the experimental results.

In order to produce an oriented single crystal the whole sample is first solidified as a polycrystalline solid by rapid cooling. When the sample is inserted into the directional solidification apparatus and allowed to equilibrate, the solid-liquid interface consists of many grains. The sample is then pulled rapidly and dendritic crystal growth starts. If a properly oriented dendrite is found, it is grown further

while dendrites from other grains are melted back with laser pulses (laser perturbation setup described in section 3.3.1) and are overgrown by the oriented dendrite until the solid-liquid interface is made up of a single grain. (If no grain develops dendrites growing in the z-direction within an angle of less than one degree, or if the sidebranches do not lie in the $x - z$ plane, the sample is melted back until other grains are at the solid-liquid interface and the process is repeated.) Once a properly oriented dendrite has been selected the temperature is lowered slowly so that the oriented grain grows and completely fills the liquid side of the sample. The temperature gradient is subsequently inverted, which melts away all other grains, and the temperature is again lowered slowly to let the single correctly oriented grain fill the complete sample. The interface is then positioned so that about three quarters of the capillary is liquid and one quarter solid. The sample, which is now a single properly oriented crystal, is brought into equilibrium in the selected temperature gradient by waiting for at least one day.

Another technique to produce oriented single crystals in the sample cell is to narrow the cell width at one end to $\sim 100\mu$m, which is only possible in sample cells created using spacers. Rapid crystal growth is then started in the narrow section. Only one dendrite fits into the thin channel so that a properly oriented dendrite can overgrow all other grains, emerging and filling the whole sample width.

3.2.3 Other Materials

Liquid crystals were used in some recent directional solidification experiments. Here the pattern of a smectic A - smectic B [102] or a nematic-isotropic [103, 104, 105, 59, 60] interface are analyzed. Liquid crystals offer truly one-dimensional interfaces, no surface tension anisotropy and approximately equal solute diffusion constants in both phases. Preliminary tests on the liquid crystal 8CB doped with C152 were carried out in collaboration with O.N. Mesquita and J.M.A. Figueiredo (UFMG, Belo Horizonte, Brazil). Capillaries can not be used for liquid crystal samples, since the glass surface has to be prepared with silane to create a hydrophobic surface and since the optimal sample thickness is of the order of 4μm. Microscope slides with Mylar spacers were used instead. The 8CB/C152 mixture was found to react quickly with all epoxies used and with Torrseal after several days. However, first results using the sample sealed with Torrseal indicate that C152 mixes with 8CB and that spatially periodic perturbations can be triggered in thin liquid crystal samples. A wealth of dynamical instabilities (e.g. traveling waves or solitons), observed in unperturbed experiments, promises to make the exploration of new steady states and stability limits through perturbations very interesting.

R. Ragnarsson and E. Bodenschatz at Cornell University recently started using a sample preparation technique similar to the one described in section 3.2.2 and use a large polymer with an embedded dye molecule (Sulfonerhodamine Bis-(PEG 2000), Molecular Probes) mixed with SCN. This creates samples with small

D, thus facilitating rapid solidification at significantly smaller V_P. In addition, Sulfonerhodamine Bis-(PEG 2000) has an absorption peak at visible light wavelengths $\lambda_{Max} = 550$nm [106], making the concentration field visible to the CCD camera through strong absorption of direct illumination. From CCD images of the concentration field in one sample, a diffusion constant of $D \approx 68\mu m^2/s$ was obtained.

3.3 Perturbation Methods

3.3.1 Laser Perturbation

A 1 Watt Model 165 Argon Ion laser (Spectra Physics, Mountain View, CA) is used at $\lambda_{Ar} = 488$nm. The light is brought to the directional solidification apparatus through fiber optics and focussed onto the sample at a small angle with a microlens (see figure 3.2). The diameter of the laser spot on the sample can be reduced to $\sim 10\mu$m. The peak absorption of C152 is at a slightly smaller wavelength than λ_{Ar} so the absorption is only a fraction of the absorption at the peak. This decreases the fluorescence intensity significantly, but it effectively prevents bleaching of the sample. Bleaching does occur after continuous illumination with UV light. In addition, the fluorescence intensity depends only on the C152 concentration and does not change after a solid-liquid phase transition, while a small increase of fluorescence intensity after melting is observed with UV illumination.

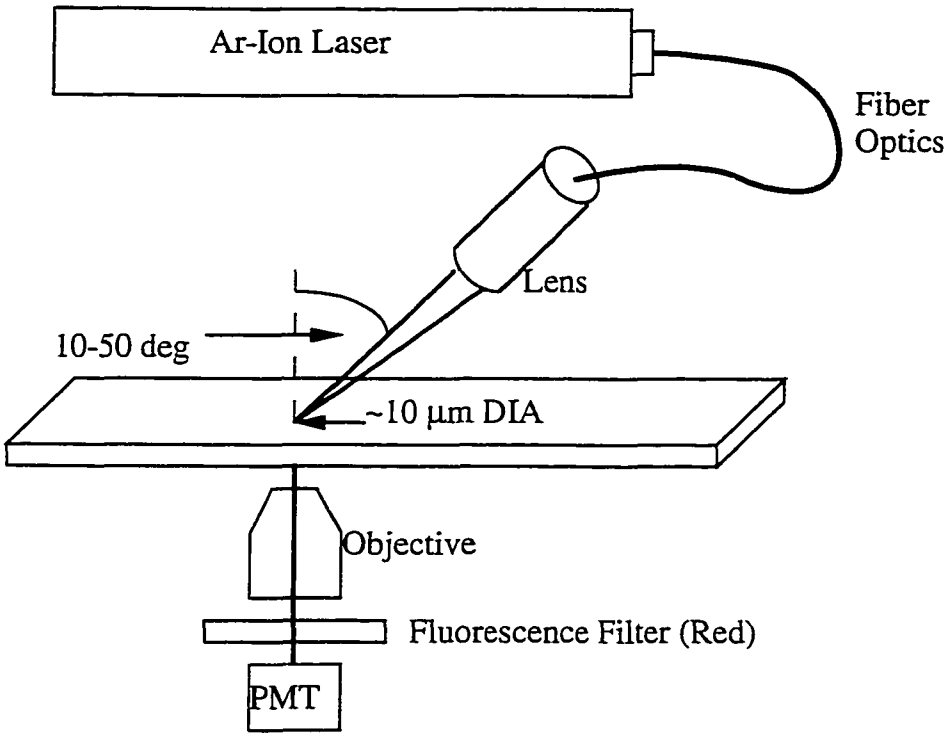

Figure 3.2: Schematic of the laser perturbation setup.

3.3.2 UV Perturbation

A UV perturbation apparatus was built using the Nikon Epi-fluorescence 2 attachment with UV optics and a 100W Hg lamp (100W/2 Osram). One mercury emission line in the near UV at $\lambda = 404$nm lies within the broad absorption peak of C152 ($\lambda_{Max} = 394$nm). Illuminating the sample with the mercury lamp leads to absorption by C152, which heats up the sample. Even though the temperature increase is small, it leads to visible melting when the UV light is focused onto the solid-liquid interface (a temperature change of 10mK changes the interface position by 5μm for $G = 20$K/cm). A reference sample without C152 shows no interface movement under UV illumination, confirming that the observed heating up of the sample is caused by the C152.

The UV light is collimated onto a Nikon Fluorescence cube equipped with an incident light filter (which selects the range $\lambda = 380$nm to 425nm that contains the near UV $\lambda = 404$nm peak of the Hg lamp from the incident light), a dichroic mirror (which reflects the incident light onto the sample and transmits light coming back from the sample only for $\lambda > 510$nm), and an outgoing light filter (which selects the fluorescent light through its transmission of $\lambda > 520$nm). Between cube and sample incident and fluorescence light pass through a $4\times$ large aperture lens.

The Fluorescence intensity is generally too small to be observable without high noise levels with the CCD camera used. The solid-liquid interface does not appear clearly in the fluorescence images. Therefore, regular illumination is often used simultaneously to track the solid-liquid interface. To create localized UV illumination the shutter in the collimator attachment was replaced by a mask holder since the contour of the shutter is focussed sharply onto the sample. Metal masks with rows of uniformly spaced holes are placed into the mask holder and positioned to produce rows of high intensity UV spots in the sample along the solid-liquid interface. See page 73 for an image of a solid-liquid interface perturbed with this setup.

This spatially periodic melting produces an approximately sinusoidal modulation along the interface with a well defined wavelength λ_P. Since UV illumination causes a perturbation of the thermal field, it is applied for sufficiently long times to allow the concentration field to adjust to the modulated interface shape.

The perturbation wavelengths currently obtainable in our apparatus with this

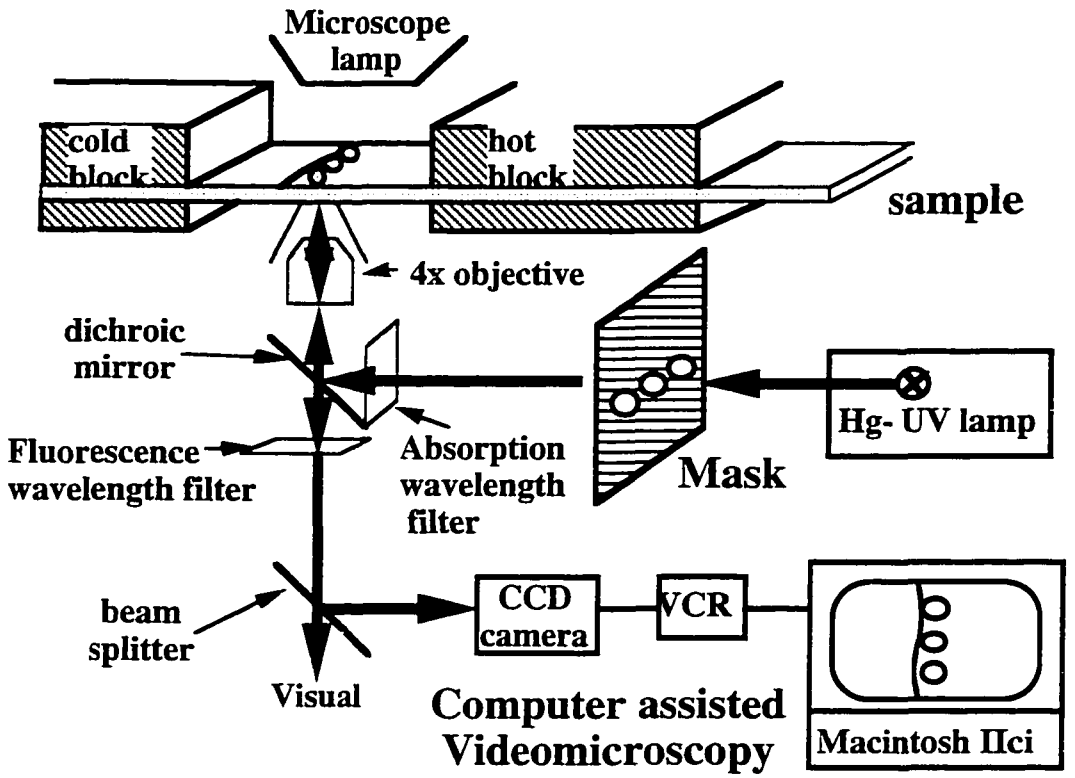

Figure 3.3: Schematic of the UV perturbation setup.

method range from $150\mu m$ (limited by machinability of the mask and low total UV intensity per spot) up to $1000\mu m$ (limited by the sample size).

3.4 Measurement of Material Parameters

The SCN-C152 alloy is best described by the one-sided model of directional solidification: The liquidus slope m and the segregation coefficient k are independent of solute (C152) concentration in the small concentration limit. Diffusion of C152 in the solid is several orders of magnitude slower than in the liquid and can be neglected.

3.4.1 Concentration Calibration

The solute concentration of each sample was calibrated by fluorescence measurements. For the low concentrations used, a linear relationship between the concentration and fluorescent intensity holds under illumination with laser light (see [43]). To determine the absolute concentration, a pure sample and a sample of known concentration, produced in a nitrogen environment to avoid sublimation loss of C152, were used as fluorescence intensity calibration standards. In recent experiments, Brown *et. al.* [107] calibrated the acetone concentration by a similar method from the intensity of the absorption peak of Acetone at $\lambda = 1700 - 1720\text{cm}^{-1}$, using Fourier transform infrared spectroscopy (FT-IR).

3.4.2 Segregation Constant

The ratio of equilibrium solute concentrations in the solid and in the liquid side of an interface (the segregation coefficient) of SCN-C152 is $k = 0.05$. It was obtained from the ratio of fluorescence intensities of the solid and the liquid side of a stationary planar interface, measured by focusing the laser onto both sides. Prior to the measurement, the crystal has to be grown with a planar interface at low growth speed ($V_P < 1\mu\text{m/s}$) over at least 3mm so that the approximate equilibrium stationary concentration in the solid is reached in the newly solidified region (solute diffusion in the solid is too slow to allow for equilibration in reasonable time without this measure). The sample then has to be left to equilibrate for > 1 day before the fluorescence intensity measurement. The segregation coefficient k is about half of

that of SCN-acetone (see [94]), within the range observed in metallic alloys [108].

3.4.3 Liquidus Slope

The liquidus slope m was determined by fixing the temperature gradient, stage and microscope focus so that the solid-liquid interface position measured by the camera reproducibly indicates the melting temperature of the sample. After sufficient equilibration time (> 2 days) the interface positions of seven samples were measured, from which we determined $m = 5.43 \pm 1$K/mol%. A liquidus slope of $m = 2.38$K/mole% was found with the conventional theory of freezing point depression. This is a factor of ~ 2 smaller than measured, possibly since the theory of freezing point depression assumes that one molecule of solute replaces one molecule of solvent. For SCN/C152 the Coumarin is ~ 3 times heavier than SCN thus presumably replacing more than one SCN in the crystalline matrix, which gives C152 a higher "effective" area of interface coverage and therefore more freezing point depression. A value of 2.15K/mole% was found experimentally for dilute SCN solutions by [109]. Unfortunately, the solute is not described in the article.

3.4.4 Diffusion Constant

The diffusion constant D was determined from an exponential fit to the concentration profile in the liquid ahead of a growing planar front as it approaches steady state (see Eq. 2.5). From the long-time asymptotic value of the characteristic length for different pulling speeds we found $D = 450 \pm 50 \mu m^2/s$. The measure-

ment of the concentration profile will be explained in section 4.1. The values of m and D were verified through fits of the experimental evolution of the position $z_0(t)$ to the WL calculations. This value is also comparable to that of SCN-acetone (for SCN/acetone: $D = 1270\mu m^2/s$ [110]) and is about ten times smaller than for typical metallic alloys [108].

Other methods of measurement gave values of D from $D = 500\mu m^2/s$ down to $D = 140\mu m^2/s$. This discrepancy is probably due to different experimental conditions and the possible presence of convection which can lead to a different *effective* diffusion constant. The measurement used was carried out under conditions relevant for all experiments in this thesis, thus providing the appropriate (effective?) diffusion coefficient.

3.5 Data Analysis

3.5.1 Extraction of the Interface Shape

The captured images are viewed on a Macintosh IIci computer using the NIH *image* program and analyzed through a set of C programs running in the Macintosh Programmers workshop MPW 3.0 environment. Custom programs are needed for the extraction of the solid-liquid interface position with better than one pixel resolution, which allows detection of very small deformations of the interface shape. For each of the 480 lines of pixels along the z-axis (perpendicular to the planar interface) the pixel greyscale profiles are extracted and a parabola is fitted through

regions of large greyscale or regions of large greyscale changes. The tip of the interpolated parabola is taken to define a point of the solid-liquid interface with a resolution of up to 0.3μm, one tenth of one pixel [111].

Different tape qualities influence the obtainable resolution. While images digitized directly from the video camera reach a resolution of 0.1pixel images digitized from Super-VHS show a noticeably smaller resolution, with the worst resolution obtained for regular VHS videotapes. Most of the decrease in resolution comes from jitter in the video image i.e. inaccuracies (by parts of a pixel) in the starting points of horizontal image lines. The extraction accuracy is shown in figure 3.4 which shows a planar interface digitized and extracted from a VHS videotape (Δ), from a Super-VHS videotape (*), and from the CCD camera directly (O).

To extract the interface profile the image is captured at desired time intervals and stored on disk. To decrease the time required for image storing and thus increase the capture rates, one can store regions of the image. Figure 3.5 shows the minimum time delay between captured frames for a 480 pixel long interface, as a function of the width of the selected region using the *get5.3* program described in appendix A on our Macintosh IIci.

For deep cellular or dendritic shapes the line can cross the interface more than once, but for further analysis only the front interface point for each line is selected through pattern recognition algorithms (described below in sections 3.5.3 and 3.5.2) that distinguish the front of the interface from the back and from stray dust points. Removal of all stray points is crucial to obtain reliable data for inter-

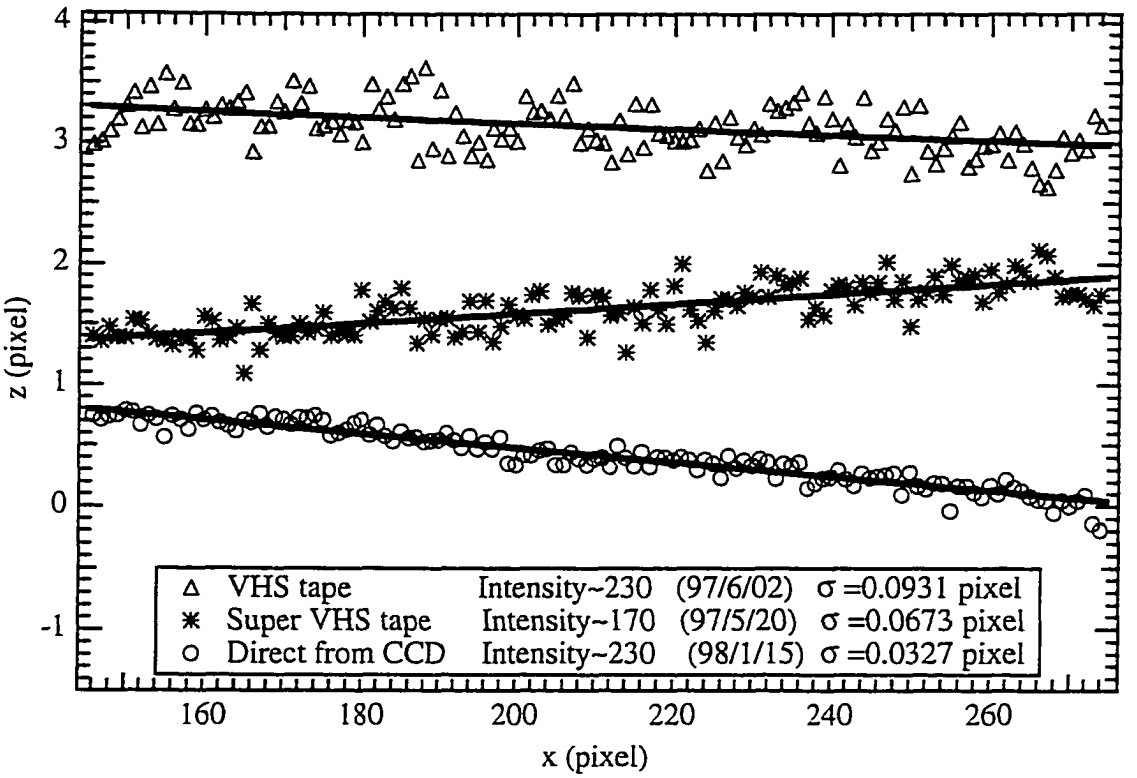

Figure 3.4: Interface profiles digitized and extracted from VHS videotapes, Super-VHS videotapes, and directly from the CCD camera.

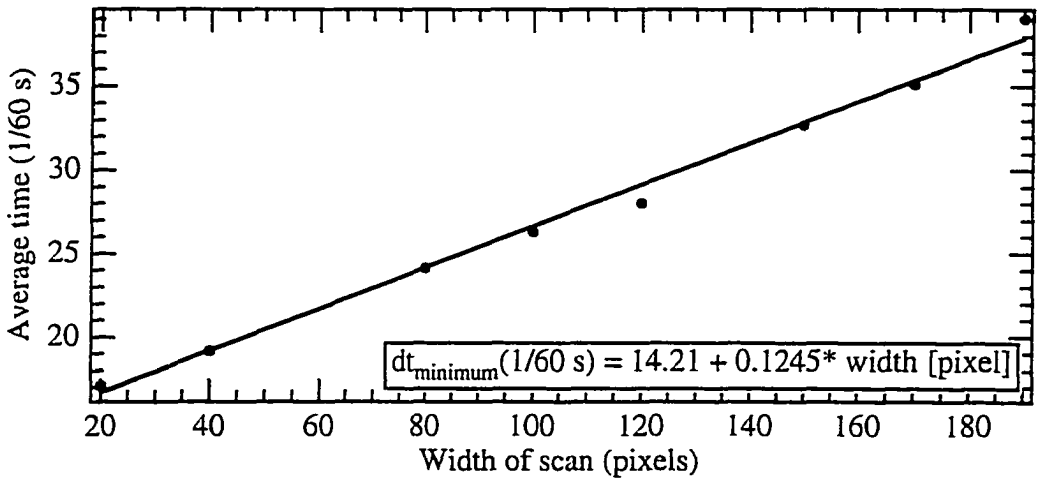

Figure 3.5: Minimum time delay between captured frames on a Macintosh IIci hard drive using the *get5.3* program as a function of the width of the extracted image region.

faces close to planar and for a determination of cellular or dendritic tip positions, spacings and shapes and comparison to theoretical predictions.

3.5.2 Pattern Recognition of Planar and Cellular Arrays

Figure 3.6 shows, from top to bottom, the steps of the pattern recognition process for cellular arrays. First, a region of the image containing a cellular array is saved. All possible interface points ($\diamond$) are then located through parabolic fits to points above a greyscale threshold. While visual recognition of the cellular pattern "hidden" in those points is simple, it poses problems for a pattern recognition algorithm due to the divergent slopes in the grooves of deep cells. Most points have to be recognized to allow for an accurate Fourier transformation and dust points in the grooves should not be mistaken for the end of a groove (this eliminates the possibility to search purely with a nearest neighbor algorithm). To recognize the cellular pattern, the following algorithm is used.

1. Compute the average z-position of all points and the standard deviation from that average.

2. Scan all lines, left to right.

3. Find three consecutive points that are less than one pixel apart in the z-direction and above the average.

4. Search the neighboring line for points with Δz similar to the two preceding points, or close to the preceding point. (allow larger Δz for points behind

the average.)

5. After reaching right end, scan all lines right to left to find improved points, but take only points close to the preceding point or points with matching *negative* Δz.

The length of the groove can still be underestimated, if the groove is bent slightly, as seen in some deeper grooves of the sample image. The extracted cellular interface profile (—) is subsequently analyzed through a spatial Fourier transform procedure (bottom of figure 3.6). In our experiments the visible interface pattern often includes fewer than 20 wavelengths which precludes a FFT (Fast Fourier Transform) analysis. The interface profile was therefore transformed through direct calculation of the Fourier integral $f(q)$ for at least 100 values of q using C programs provided by J.M.A. Figueiredo [112]. The largest peak of $f(q)$ determines the largest Fourier component q_0 with good frequency resolution, reveals small shifts in frequency, and provides the amplitude of the largest Fourier component with better accuracy than FFT.

3.5.3 Pattern Recognition of Dendritic Arrays

The position of all dendrite tips and the radius of those tips are the most important features of a dendritic array for a dendritic stability analysis. Of all interface points (extracted through parabolic fits to greyscale areas above a threshold as described above) a small set of points around the dendrite tips is selected through the following pattern recognition algorithm:

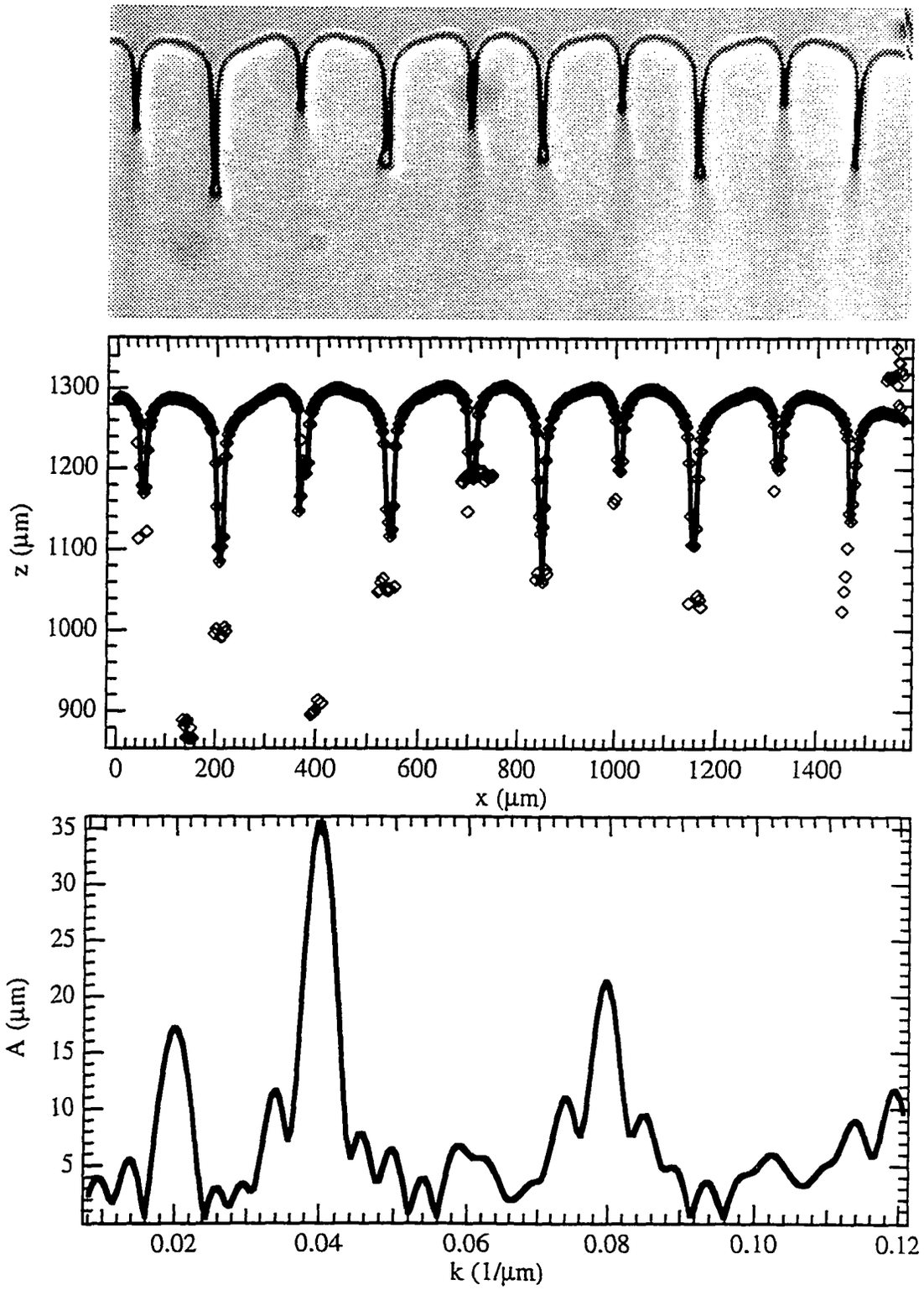

Figure 3.6: Pattern recognition process for cellular arrays, from top to bottom: Image region with cellular array; interface points (calculated from points with a greyscale above threshold (◇) and selected continuous line of points of a cellular interface (—); and spatial Fourier transform of the interface profile.

1. All points are eligible.

2. Of all eligible point the largest z-position is selected.

3. The 16 neighboring x-positions are checked for a parabolic dendrite tip: At least eight points have to be found within a maximum distance of one another (a maximum distance of three pixel times the x distance proved useful with a maximum of four for the x distance and less than 30% of x positions without a point in that range).

4. If the parabola has an inappropriate radius or tip position, or not enough points are found the largest z point becomes ineligible. Return to (2.).

5. The parabola is taken as a dendrite tip and all points behind the parabola within an angle of 45% become ineligible for further consideration. Return to (2.) until all points are checked.

Figure 3.7 shows, from top to bottom, the steps in the data extraction process: The image region with dendrite tips, interface points obtained from parabolic fits of the greyscale profile above threshold, selected points around the dendrite tip with fitted parabola, and close-up comparison of datapoints and fit.

As shown in the figure, parabolic fits provide a good description of the dendrite close to the tip (sidebranches eventually outgrow the parabolic envelope along the side of the dendrite) and help determine the tip position and radius with good accuracy.

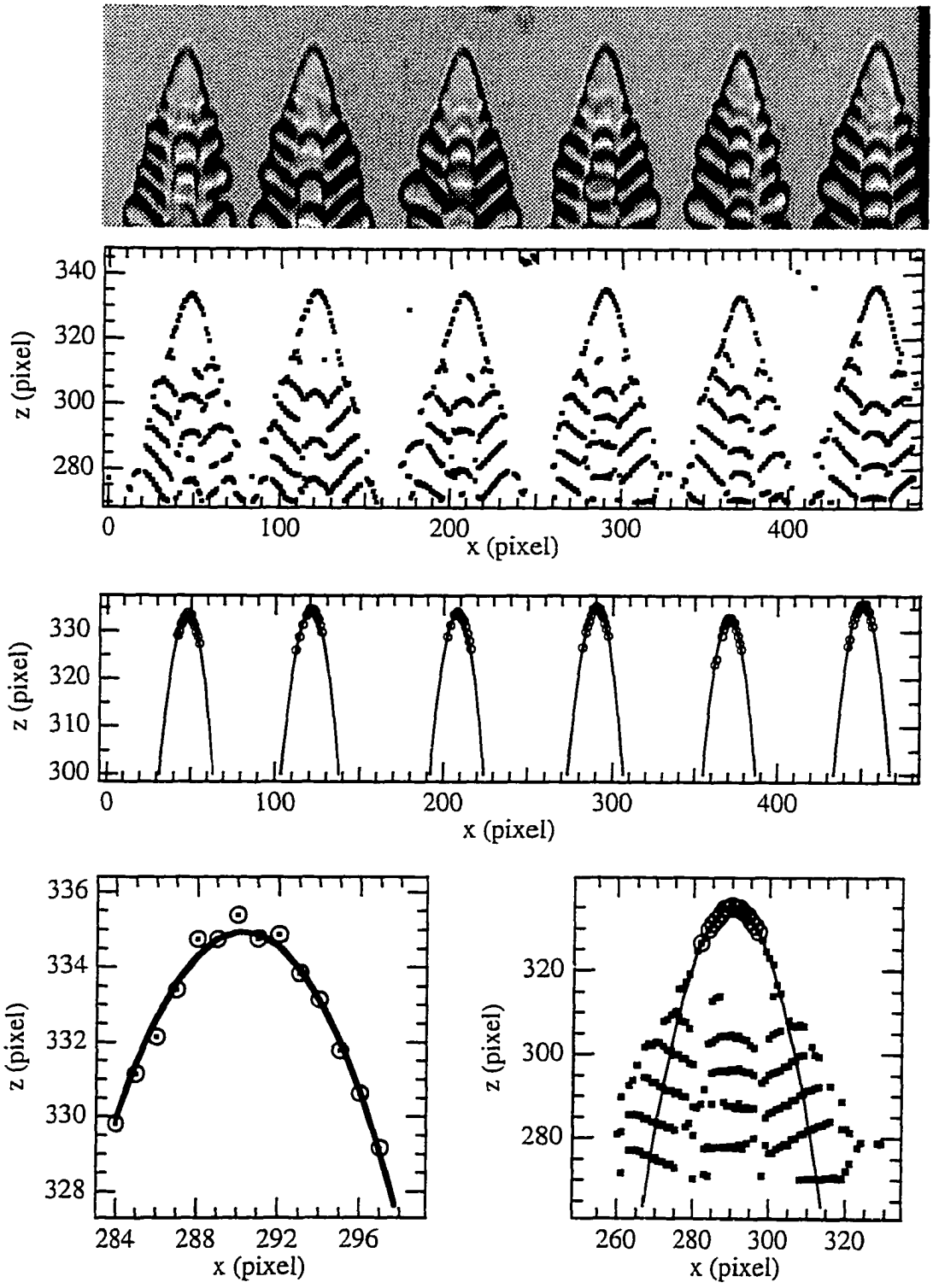

Figure 3.7: Pattern recognition process for dendrites, from top to bottom: The image region with dendrite tips, interface points obtained from parabolic fits of the greyscale profile above threshold, selected points around the dendrite tip with fitted parabola, and close-up comparison of datapoints and fit.

Chapter 4

EVOLUTION OF DENDRITIC PATTERNS FROM A PLANAR FRONT

[1]In this first chapter on experimental results, the dynamics of the buildup of solute ahead of the initially stable planar interface, the instability of the planar front, and the subsequent evolution toward a dendritic pattern are are investigated experimentally. Our emphasis is on the initial instability, because it is a relatively simple instability that had not been quantitatively understood, and because this instability is the starting point from which one can analyze the coarsening dynamics toward a dendritic array.

The buildup of solute and the subsequent instability of the planar front were

[1]This chapter was adapted from my publications [2, 3].

measured in detail and compared to recent theoretical calculations by Warren and Langer [39]. The fluorescence of Coumarin 152 was used for direct observations of the evolution of the solute concentration profile ahead of the initially planar solid-liquid interface. UV absorption was used to produce thermal perturbations of the sample which generated spatially periodic modulations of the planar interface. This technique allows for measurement of both positive and negative linear growth coefficients (determined from the growth or decay rate of the modulation after the perturbation is switched off) for a large range of wavevectors.

The marginal stability time t_i at which the planar interface first becomes unstable and the time delay between t_i and the crossover time t_0 at which the interface modulation becomes observable are determined experimentally.

The interface morphology is analyzed as the cellular pattern appeared, and followed through the coarsening phase to the final steady state dendritic pattern. The relevance of the initial instability for steady state pattern selection is verified experimentally and some aspects of the coarsening dynamics are measured and compared with theoretical predictions of Warren and Langer [39, 40].

4.1 Evolution of the Solute Concentration Field and Recoil of the Planar Interface

We first investigated the time evolution of the solute concentration field $C(z,t)$ and the interface position $z_0(t)$ in the SCN-C152 mixtures following initiation of

pulling at constant speed V_P at $t = 0$. The Warren-Langer prediction is that $C(z,t)$ will obey Eq. 2.13 with the decay length $\ell(t)$ determined by the numerical solution illustrated in Fig. 2.4. At $t = 0$, $C(z,t)$ should exhibit a step discontinuity at the interface with $C(z,0) = C_\infty$ in the liquid and $C_s(0) = kC_\infty$ in the solid. As $t \to \infty$, $C(z_0,t)$, the concentration on the liquid side of the interface should increase to C_∞/k, while $C_s(z_0,t)$, the concentration on the solid side of the interface should approach C_∞.

The fluorescence of C152 permits measurement of the solute concentration profile since the fluorescence intensity is directly proportional to the solute concentration for the small concentrations used in the experiments. Unfortunately, fluorescence is too weak to allow for good visualization of solute buildup with the CCD camera. While absorption of C152 lies mostly in the UV, the laser dye embedded in a polymer used by Ragnarsson *et al* (see chapter 3.2.3) strongly absorbs visible light which allows for a good observation of the solute buildup. Figure 4.1 shows CCD-camera images of SCN with 0.1wt% Sulfonerhodamine Bis-(PEG 2000) (with $G = 28.7$K/cm) after the pulling motor is switched on at 16:00 minutes with $V_P = 0.33\mu$m/s. The solute buildup is clearly visible, since it darkens the region ahead of the interface. While the greyscale range $(0-255)$ is too limited for quantitative measurements of the solute buildup, image analysis shows that the greyscale intensity ahead of the interface can be fittted well with an exponential.

For quantitative determination of $C(z,t)$, a 488nm laser beam of $< 10\mu$m diameter was scanned along the 0.3wt% SCN/C152 sample perpendicular to the

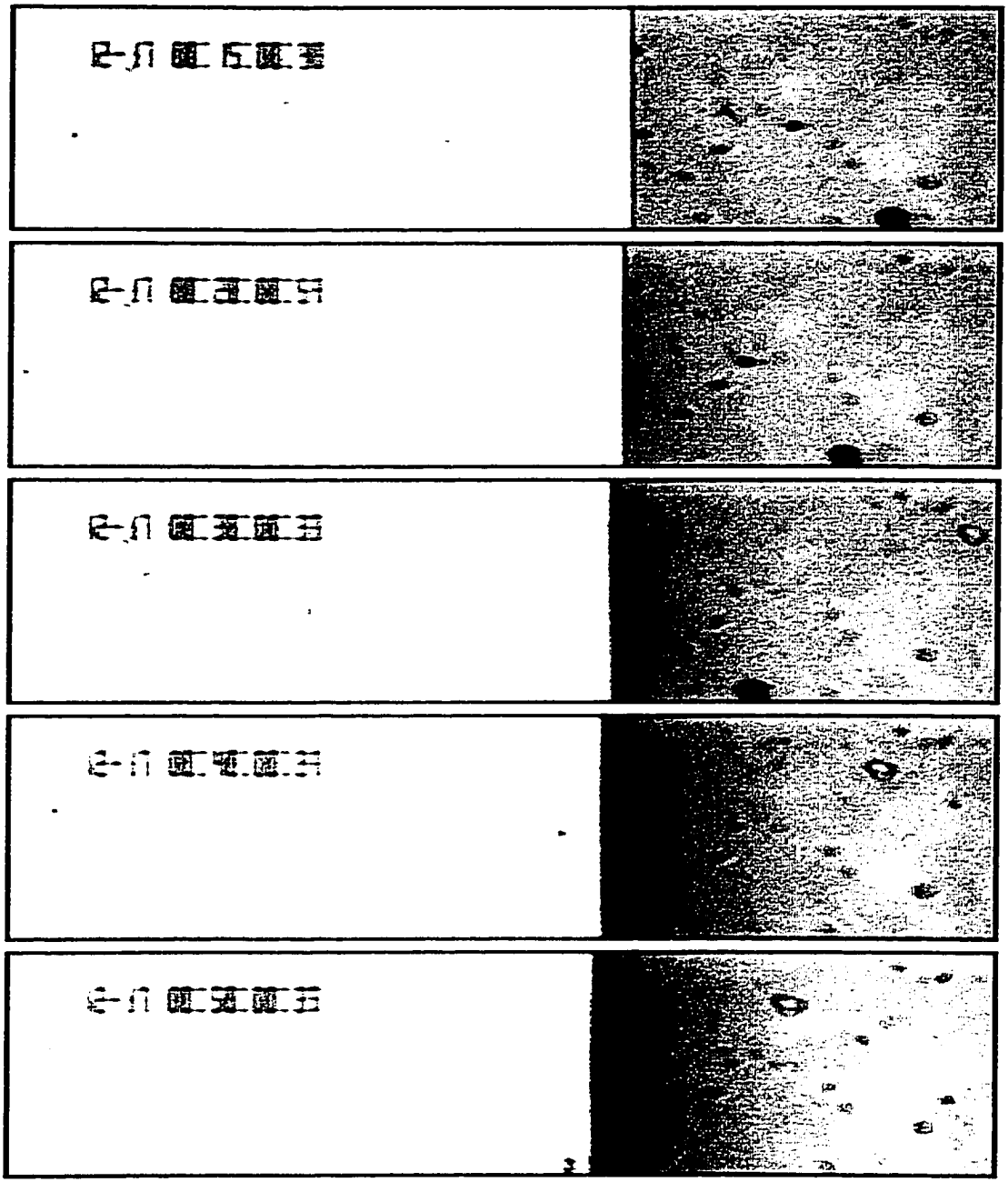

Figure 4.1: Observation of solute buildup: CCD-camera images of SCN with 0.1wt% Sulfonerhodamine Bis-(PEG 2000) (with $G = 28.7$K/cm) after the pulling motor is switched on at 16:00 minutes with $V_P = 0.33\mu$m/s. Time indicated in minutes:seconds:$\frac{1}{100}$sec.

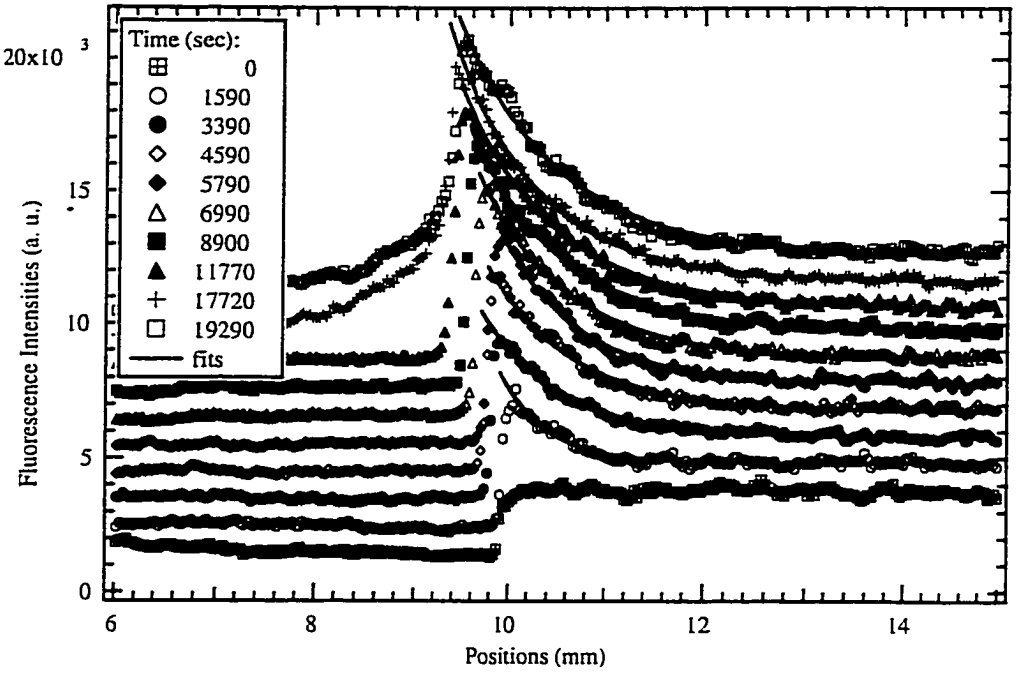

Figure 4.2: Experimentally observed solute concentration profile of SCN/C152 evolving with time after initiation of pulling with $V_P = 0.44\mu$m/s ($C_\infty = 0.3$wt%, $G = 15$K/cm) (symbols). Exponential fits to the data are shown as solid lines.

interface, and the fluorescence intensity was recorded with a photomultiplier. The observed buildup of $C(z,t)$ and the accompanying "recoil" of the interface position $z_0(t)$ with time are shown by the symbols in Fig. 4.2.

Even though in this experiment $V_P > V_C$, the planar interface remains stable for a long transient time. Fits to the WL Eq. 2.13 are also shown, with the resulting diffusion length $\ell(t)$, obtained from two such experiments, shown in Fig. 4.3. The evolution of $\ell(t)$ is in reasonable quantitative agreement with the WL calculations shown as the solid line in Fig. 4.3.

The steady state value of $\ell(t)$ is approached on the timescale of $\frac{2D}{V_P^2} \sim 4600s$, since the sample is pulled a distance $\ell(t \to \infty)$ in that time. The approach to

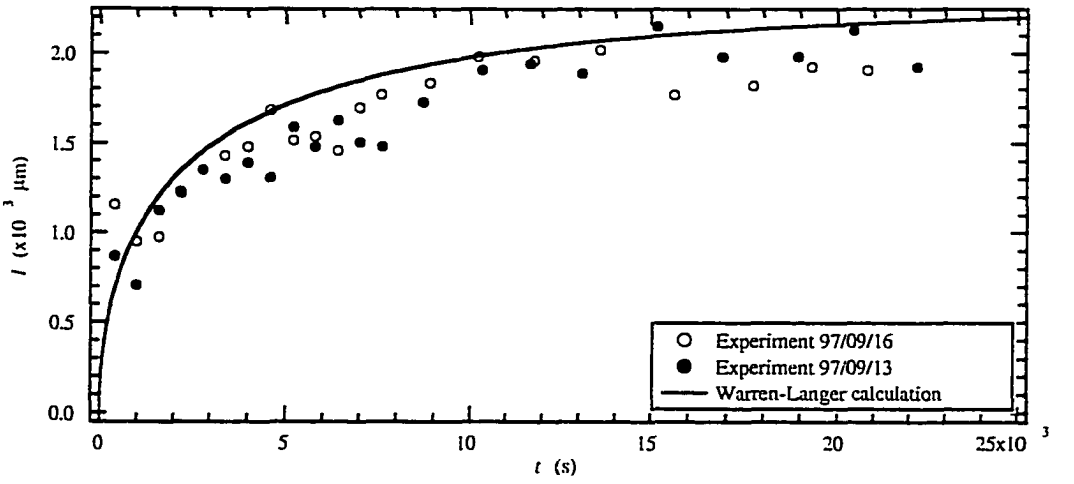

Figure 4.3: Diffusion length $\ell(t)$ for two experiments obtained from exponential fits (symbols) and from the Warren-Langer calculation with $V_P = 0.44\mu$m/s ($C_\infty =$ 0.3wt%, $G = 15$K/cm) (solid line).

steady state for the interface position $z_0(t)$ occurs much more slowly on a timescale of $\frac{D}{kV_P^2} \sim 46000s$ [113, 114]. (Even if the interface could could reject all solute in its way, it would take that long to accumulate the solute necessary for a steady state solute spike.) It is, therefore, possible to observe the approach to steady state for $\ell(t)$ in this experiment even though $V_P > V_C$. This experiment was also used to determine the diffusion coefficient D since $\ell(t \to \infty) = \frac{2D}{V_P}$.

The WL prediction for the interface position $z_0(t)$ is shown in Fig. 2.3. At low growth speeds ($V_P < V_C$) the time required for $z_0(t)$ to reach the steady-state position (Eq. 2.12) is unobservably long for our low k alloy, while at higher growth speeds, the instability intervenes before the steady-state value of Eq. 2.12 is reached. At speeds close to V_C after some time (on a longer timescale than the approach to a steady state $\ell(t)$, but before a steady state for $z_0(t)$ is reached) the position of the interface $z_0(t)$ stops following the WL prediction even though no

instability of the planar interface is observed. The fluorescence measurements indicate that this departure is probably due to solute trapping possibly arising from an instability in the third dimension that forms one cell across the small side of the sample. An indication of the solute trapping can be seen in the concentration profiles in Fig. 4.2 at $t = 17720s$ and $19290s$ as a strong increase of fluorescence intensity on the solid side of the interface. While the liquid ahead of the interface still has an exponentially decaying concentration profile with essentially unchanged $\ell(t)$, the interface position and the amplitude of the solute spike no longer follow the WL predictions. The influence of wall effects has been investigated previously through variations in sample width [113], but our procedure allows *in situ* observation and direct measurement of solute trapping at the walls. Before the clearly visible onset of the 3D instability, the initial transient can thus be safely treated by two-dimensional approximations. For higher speeds, wall effects start to occur at the same time as the initial instability. A detailed analysis of the influence of the third dimension using direct measurements can be found in chapter 8.

Figure 4.4 shows the measured interface position $z_0(t)$ vs t for a pulling speed $V_P \approx 6V_C$.

The interface initially moves back at the pulling speed V_P (indicated by the dashed line) only for unobservably short times since attachment kinetics are very rapid. Subsequently, $z_0(t)$ follows the WL prediction for a planar interface (shown by the solid line) until the interface position levels off due to solute trapping at $t \sim 7000s$. The first-order analytic approximation calculated in [39] (indicated

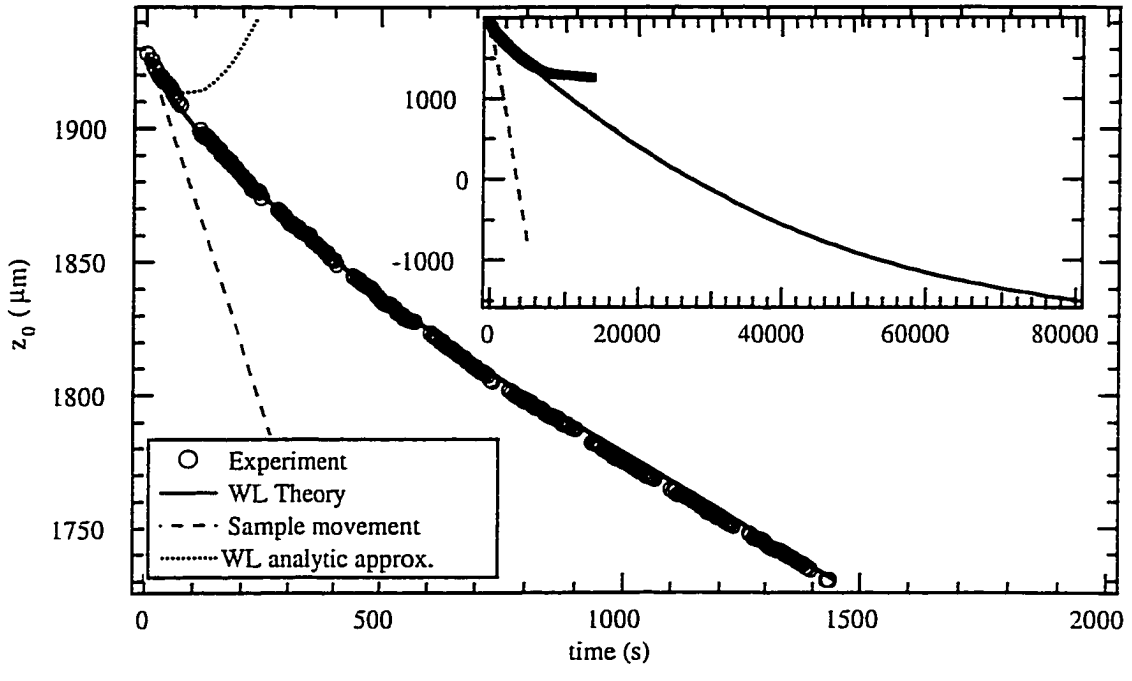

Figure 4.4: Planar interface position $z_0(t)$ vs t of a SCN/C152 sample (V_P = 0.549μm/s, C_∞ = 0.30wt%, G = 20.2K/cm). Comparison to WL calculation (—), WL analytic approximation ($\cdots$), and sample movement(- - -). The insert shows the long-time behavior where the WL-prediction breaks down due to solute trapping.

by the dotted line), breaks down too quickly to be observable or relevant for the initial instability.

4.2 Linear Growth Coefficients and the Marginal Stability Time t_i

The linear stability analysis of Mullins and Sekerka, as extended to the non-steady state situation by Warren and Langer, requires the evaluation of the time-dependent linear growth coefficients $a_q(t)$. While the $a_q(t)$ have been calculated theoretically, they have not previously been determined experimentally in directional solidification. The only way to study $a_q(t)$ in the past was to wait for the instability to develop spontaneously and then to measure the modulation amplitude as a function of time. That approach can only determine $a_q(t)$ for a single q, and only if a_q is positive.

We have developed a procedure to determine $a_q(t)$ for experimentally selected values of q in which we apply a row of small spots of UV illumination briefly to the crystal-melt interface to locally heat up the sample through the absorption of UV light by the C152. (The UV perturbation apparatus is described in chapter 3.3.2.) The UV perturbation of the interface position and concentration field are best seen in the Succinonitrile-Polymer system. Figure 4.5 shows CCD-camera images of SCN with 0.1wt% Sulfonerhodamine Bis-(PEG 2000) (with G = 28.7K/cm) 50:09 minutes after the pulling motor is switched on at $V_P = 0.33\mu$m/s.

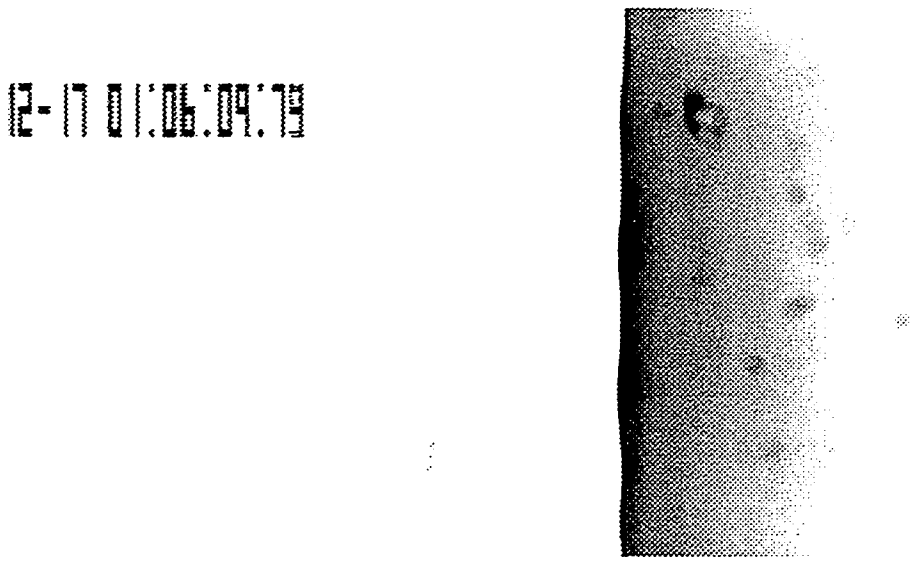

Figure 4.5: Spatially periodic UV perturbation of the planar interface and concentration field: CCD-camera images of SCN with 0.1wt% Sulfonerhodamine Bis-(PEG 2000) (with $G = 28.7$K/cm) 50:09 minutes after the pulling motor is switched on at $V_P = 0.33\mu$m/s.

Figure 4.6 shows the interface of a 0.30wt% SCN/C152 sample being pulled at 0.8μm/s in a temperature gradient of $G = 20.25$K/cm. Frame 2 ($t = 10.5$min) shows a row of UV spots with a spacing of $\lambda = 225\mu$m (visible as white circles) which was applied for one minute starting at $t = 10$min. Absorption by the C152 caused local heating, producing a sinusoidal modulation of the planar interface, which gradually decayed indicating that $a_q(t) < 0$.

The Fourier transform of the interface provided the time-dependent amplitude of the largest Fourier component of the modulation, at $\lambda = 225\mu$m. The time-dependent amplitude, shown by the symbols in Fig. 4.7, was fit to an exponential (a straight line on the semilog plot) for the range $t = 684$s to $810s$ which gave $a_q = -0.0136\text{s}^{-1}$. The WL analysis predicts that for this wavelength, $a_q(t)$ would

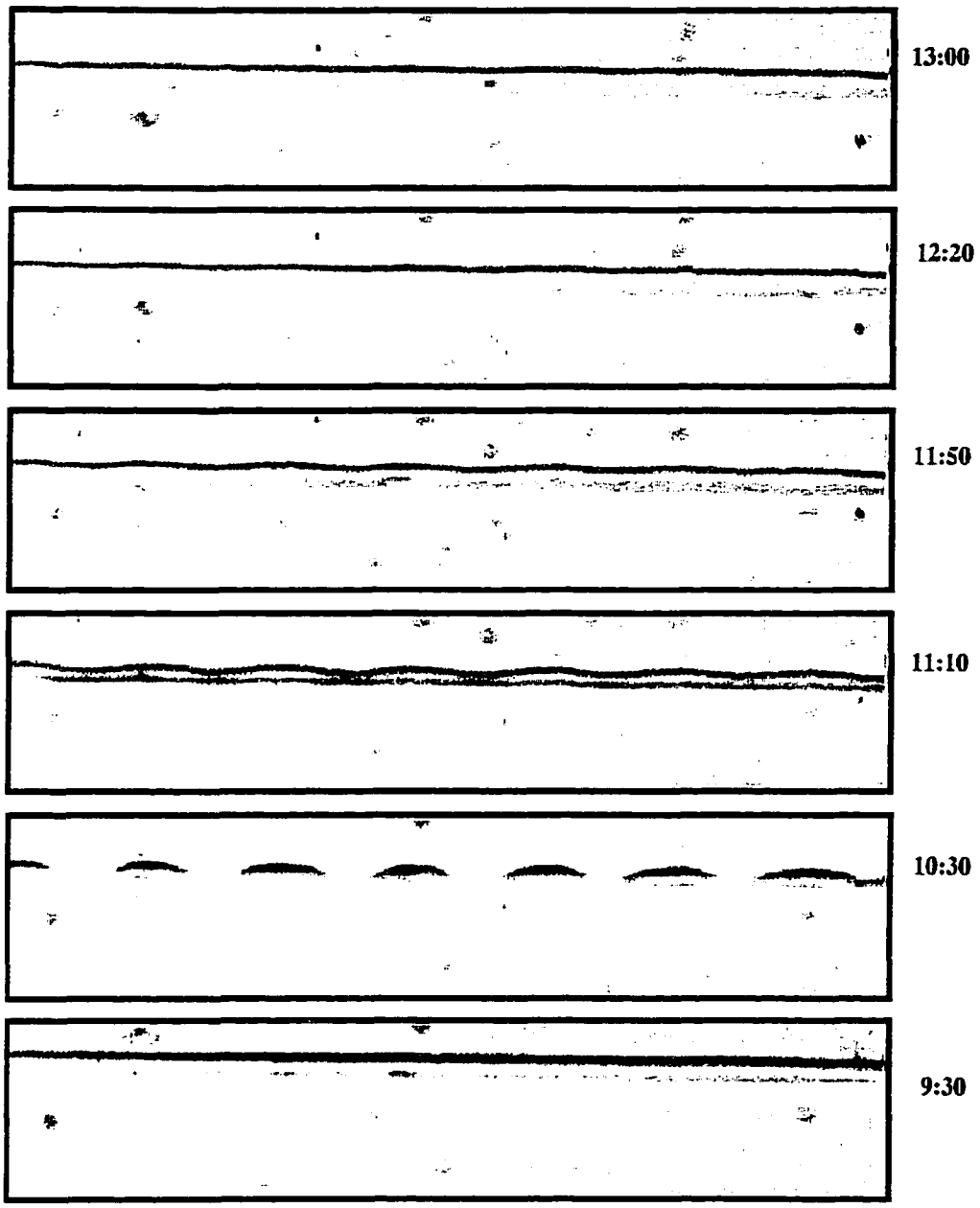

Figure 4.6: Initiation and decay of the modulation produced by a spatially periodic UV thermal perturbation with $\lambda = 225\mu$m for a planar interface (SCN/C152: $V_P = 0.8\mu$m/s, $C_\infty = 0.30$wt%, $G = 20.2$K/cm) (time increases from bottom to top).

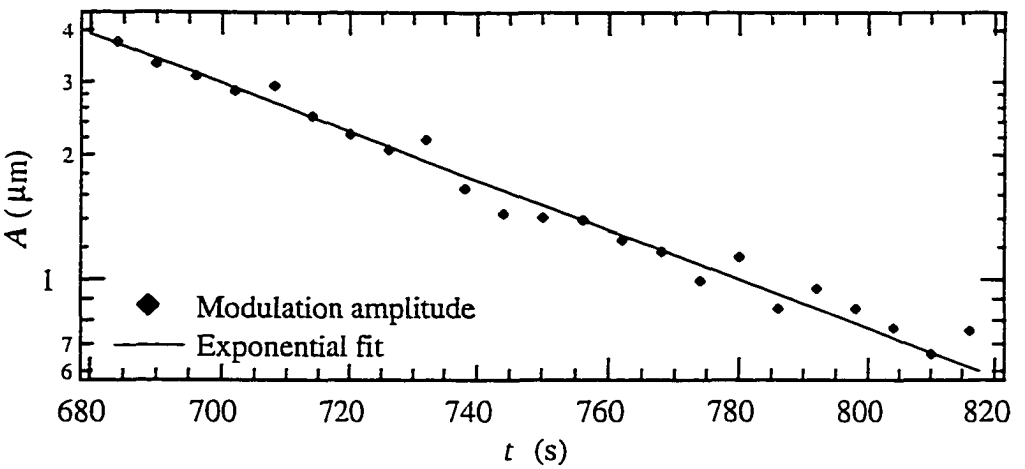

Figure 4.7: Amplitude of the largest spatial Fourier component of the interface modulation vs time, and exponential fit in the range $t = 684 - 810$s.($a_{q,fit} = -0.136\text{s}^{-1}$) (Modulation produced by a spatially periodic UV thermal perturbation with $\lambda = 225\mu$m for a planar interface (SCN/C152: $V_P = 0.8\mu$m/s ($C_\infty = 0.30$wt%, $G = 20.2$K/cm)).

increase from -0.0139s^{-1} at 684s to -0.0120s^{-1} at 810s.

To study the time dependence of $a_q(t)$, the measurement described above was repeated sequentially as soon as the modulation had decayed. Crystal growth was started at $t = 60$s with $V_P = 0.52\mu$m/s. The row of UV spots was applied for $60s$ to the solid-liquid interface at $t = 300$s, 900s, 1500s, 2100s, 2700s, 3600s and 4500s. The amplitude of the largest Fourier component of the planar interface modulation, shown in Fig. 4.8, was then fitted with an exponential after each perturbation.

At early times, the decay of the modulation amplitude can be fitted well with a single exponential. The linear approximation of Eq. 2.16 therefore describes interface stability accurately even though the amplitude of the applied modulation is orders of magnitude larger than thermal noise. As long as the modulation decays quickly, the time dependence of $a_q(t)$ can be neglected. However, as the solute

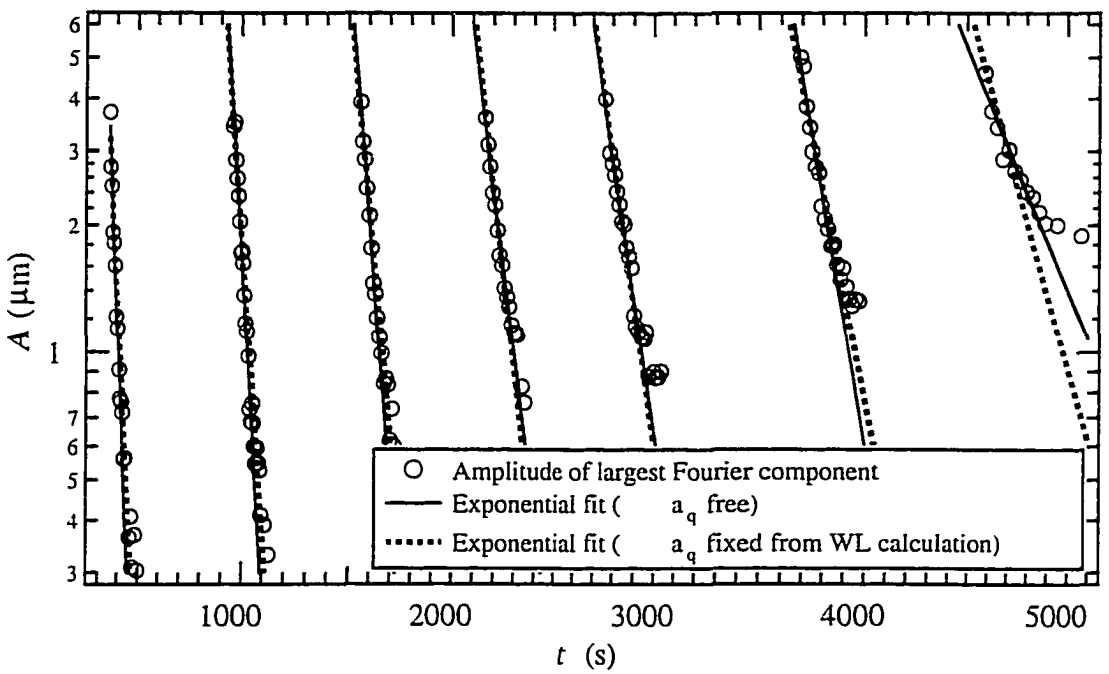

Figure 4.8: Amplitude of the spatial Fourier component with $q_1 = 0.0228\mu\text{m}^{-1}$ of the interface modulation (o) vs time, when a 60s perturbation with q_1 is applied at t_R = 300s, 900s, 1500s, 2100s, 2700s, 3600s, 4500s. Exponential fits to $A_{q_1}(t) = Ce^{-a_{q_1}(t_R)t}$ after each perturbation time t_R with $a_q(t_R)$ as a free parameter (—) and $a_q(t_R)$ given by the WL calculation ($\cdots$).

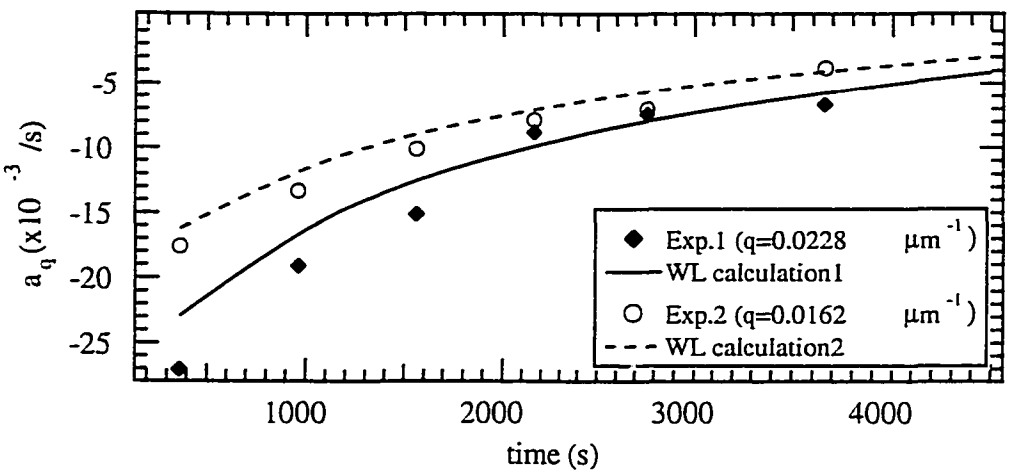

Figure 4.9: Time dependence of $a_q(t)$ from exponential fits to the amplitude of the largest Fourier component of the interface modulation when a 60s perturbation with $q = 0.0228\mu\text{m}^{-1}$ (•) or $q = 0.0162\mu\text{m}^{-1}$ (○) is applied at $t_R = 300\text{s}, 900\text{s}, 1500\text{s}, 2100\text{s}, 2700\text{s}, 3600\text{s}$ and comparison to WL predictions.

concentration builds up and $a_q(t)$ approaches zero at $t \sim 4500$s, the modulation decays slowly and a single exponential fit no longer works well.

The linear growth coefficient $a_q(t)$ for two experiments at $V_P = 0.52\mu$m/s with $q = 0.0228\mu\text{m}^{-1}$ and $q = 0.0162\mu\text{m}^{-1}$ obtained from the fits is plotted in figure 4.9 together with the WL predictions.

The good agreement between theory and experiment indicates that interface stability during the transient can be calculated using the WL approach. Even for $V_P > V_C$, as in this experiment, interface stability can be described well by a linear stability analysis and the planar interface remains morphologically stable until $a_q(t)$ changes over from negative to positive for some one q. In analogy to the steady-state marginal stability at V_C, we can introduce a marginal stability time t_i such that $a_q(t_i) = 0$ for some q. This t_i marks the onset of instability beyond

which the planar interface will spontaneously deform, and the interfacial pattern will then begin to evolve towards its final steady-state morphology.

4.3 Onset of the Initial Instability and Crossover Time

When the pulling speed V_P in a directional solidification experiment exceeds the critical value V_C, the planar interface eventually destabilizes and evolves into a cellular or dendritic pattern. The WL analysis [39] shows that the onset of morphological instability occurs at the marginal stability time t_i while the concentration field is still building up. The WL analysis also determines a crossover time t_0 when the modulation amplitude becomes comparable to the mean wavelength λ_0, as described at the end of section 2.2.2. To obtain predictions for t_0 and λ_0, the amplitude evolution is calculated for a large range of modes starting from thermal noise which is orders of magnitude smaller than an observable amplitude. When the pulling motor is started at $t = 0$ the interface initially remains planar until t_i, when the linear growth coefficient $a_q(t)$ crosses over from negative to positive for some q. Subsequently, the interface becomes morphologically unstable for a continuously expanding range of wavelengths. It takes longer, however, for the modulation to grow until it becomes observable (and nonlinear) at $t = t_0$.

Figure 4.10 shows WL theoretical results for the evolution of the modulation amplitude (assuming either thermal noise ($\cdots$) or a 100 times stronger noise term (-

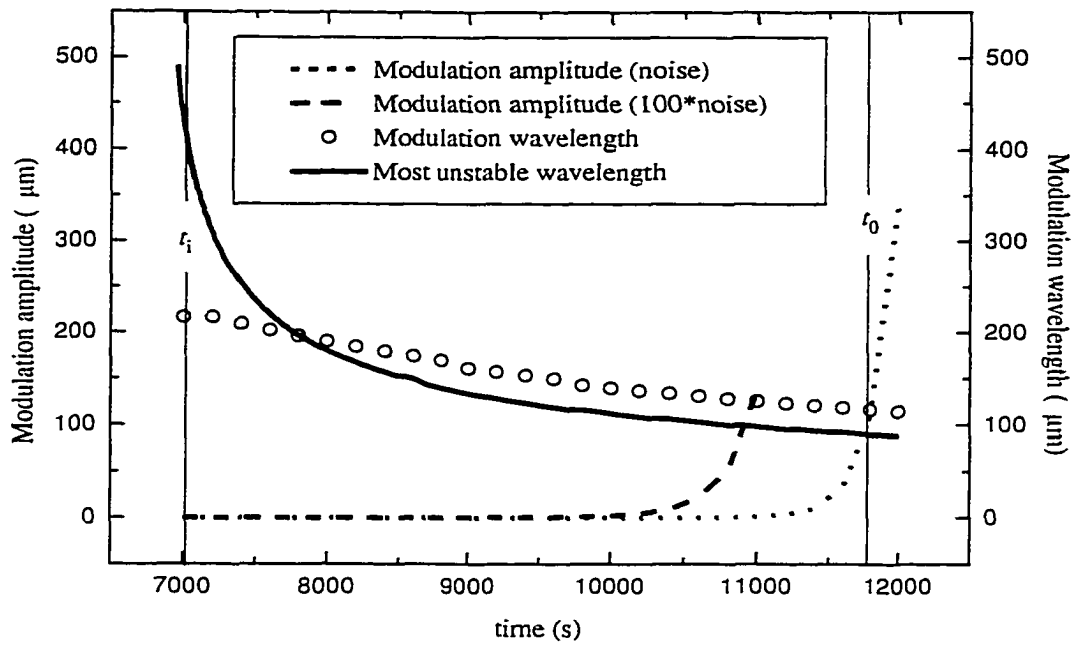

Figure 4.10: Warren-Langer theoretical results for the evolution of the modulation amplitude (assuming thermal noise (· · ·) or a 100 times stronger noise term (- - -)], the wavelength of this modulation (O), and $2\pi/q_{max}$, the wavelength of the most unstable mode (—), all calculated between the marginal stability time t_i and the crossover time t_0.

- -)], the predicted wavelength of the modulation (O), and $2\pi/q_{max}$, the wavelength of the most unstable mode (—), all calculated between t_i and t_0.

The crossover time t_0 and wavelength λ_0 are well defined since the modulation wavelength shifts only slowly while the modulation amplitude grows faster than exponentially making the two curves cross almost perpendicularly in Fig. 4.10. The crossing point determines t_0 and λ_0. A change in the noise level by a factor of 100 changes t_0 and λ_0 by only about 10%. The wavelength of the most unstable mode differs from the modulation wavelength, since the latter is influenced by the noise spectrum and by the previous evolution of the linear growth coefficients. The

wavelength of the most unstable mode decreases rapidly immediately after t_i, but decreases slowly near t_0.

The transition from negative to positive linear growth coefficient (for a selected q value q_1) at $t_i(q_1)$ during the buildup of solute ahead of the planar interface, and the delay between the marginal stability time t_i and a visible crossover from planar to cellular interface at t_0, can be determined experimentally. Figure 4.11 shows the amplitude of the largest Fourier component of the interface profile in experiments with the parameters $C_\infty = 0.22$wt%, $G = 15.7$K/cm and $V_P = 1.04\mu$m/s. In experiment A (X,O) the interface was first perturbed for 60s at $t = 600$s with $q_1 = 0.0226\mu\text{m}^{-1}$, and the modulation of the planar interface was observed to decay exponentially, indicating a negative linear growth coefficient. At $t = 1200$s the interface was perturbed again for 60s with the same q_1 and the modulation initially decayed, but then started to grow. The time $t_i(q_1) \sim 1800$s when the amplitude minimum occurs marks the transition from a negative to a positive linear growth coefficient for this q_1 indicating that the interface has become morphologically unstable. (Note that t_i, the time of marginal stability, corresponds to the smallest possible $t_i(q_1)$ for any q_1, so that $t_i \approx 1800$s.)

When the interface is not perturbed, as in experiment B (Δ), no modulation of the planar interface is observed at $t = 1800$s although the interface is already unstable. Interface modulation only starts to become visible at $t \sim 3000$s when the mode with $q = 0.0540\mu\text{m}^{-1}$ becomes the biggest mode in the Fourier spectrum of the interface profile and starts to grow exponentially. In experiment A, a halving

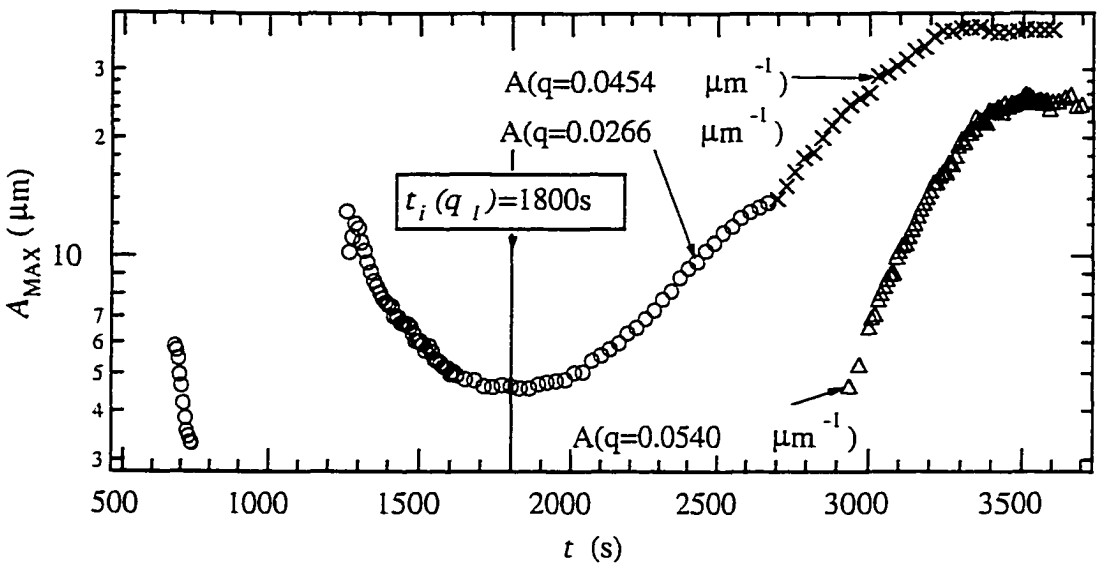

Figure 4.11: Amplitude of the largest Fourier component of the interface modulation during the planar-cellular crossover of a planar interface with perturbations applied at 600s and 1200s (X,O), and without perturbations (Δ).

of the wavelength of the largest Fourier component was observed to occur spontaneously at $t \sim 2700$s, making the wavelengths of the largest Fourier components for $t > 3000$s comparable in both the perturbed and unperturbed experiments. These experiments illustrate that while the planar interface becomes morphologically unstable for $t \sim t_i \leq 1800$s, this marginal stability occurs well before any instability can be observed in an unperturbed experiment.

We have systematically measured the crossover time $t_{0,exp}$ and wavelength $\lambda_{0,exp}$ for pulling speeds ranging over two orders of magnitude using a SCN/C152 sample with $C_\infty = 0.43$wt% and $G = 20.2$K/cm. Figure 4.12 shows the experimental $\lambda_{0,exp}$ (O), the WL calculation of λ_0 (—), the most unstable mode λ_{max} from a steady state Mullins - Sekerka calculation (—·) and the two marginally stable modes under the Mullins - Sekerka steady state assumptions (···). The WL calculation agrees

well with the observed crossover wavelength for all pulling speeds as previously found by WL [39]. While $\lambda_{0,exp}$ lies within the range of unstable modes predicted by the Mullins - Sekerka analysis, λ_{max}, the wavelength of the most unstable mode at steady state (indicated by the dashed line) is smaller than the observed wavelength for all pulling speeds studied by a factor ~ 5 [57]. In addition, figure 4.12 shows the mode which becomes marginally unstable first at t_i in the WL theory ($-\cdot$). The wavelength of this mode also differs from the experimental values by a factor of 2-3, indicating that the wavelength of the most unstable mode decreases during the delay from t_i to t_0 until the modulation becomes visible (see figure 4.10).

The experimental crossover time $t_{0,exp}$, measured over nearly three orders of magnitude in V_P , is shown in Figure 4.13. It agrees reasonably well with the WL calculation (full line) but is systematically slightly shorter. This difference could be due to the fact that the initial noise level is larger than the thermal noise WL assumed in their calculation, since an increased initial level of noise-induced modulations would decrease t_0 (see figure 4.10). One possible source for an increased initial noise level at the interface is the contact line between the SCN crystal and the glass capillary which can lead to a localized mechanical perturbation of the planar interface. This influence of the third dimension becomes less significant at higher pulling speeds, as discussed in section 8. Nevertheless, the WL theoretical marginal stability time t_i (dashed line) is considerably shorter than both the experimental and the theoretical t_0, except at the lowest pulling speed. These experiments show that the WL linear stability analysis is a useful method for cal-

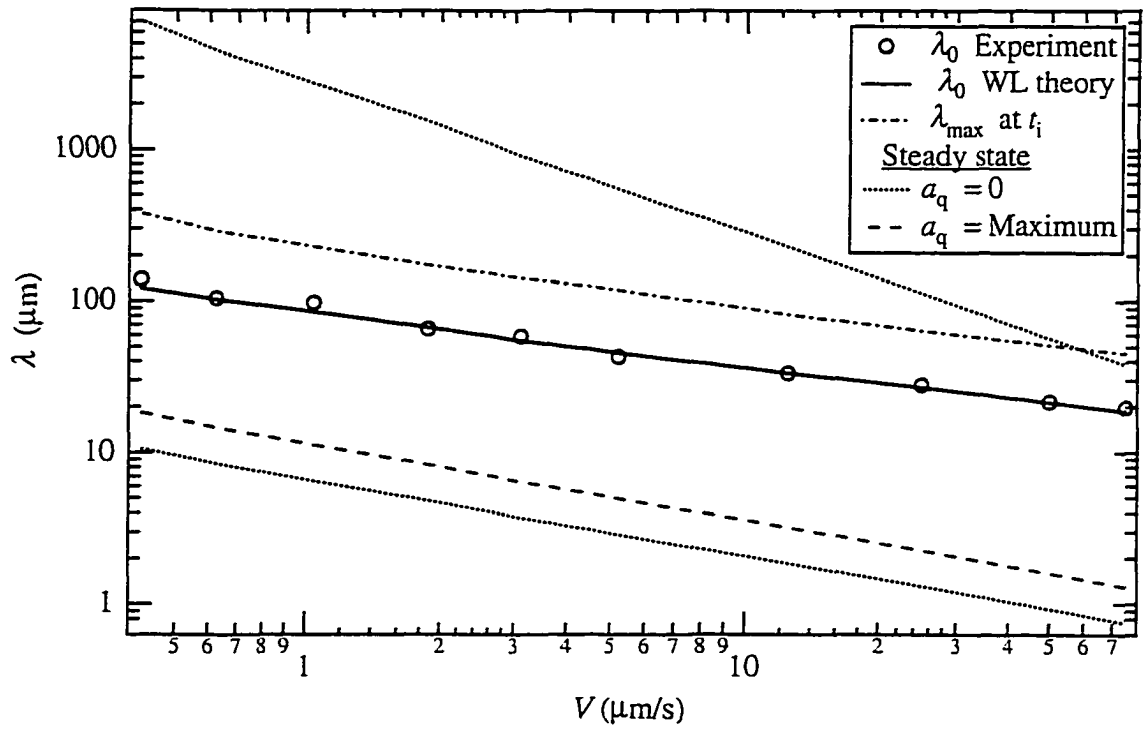

Figure 4.12: Comparison of the Warren-Langer theory and experiment for the crossover wavelength λ_0 as a function of pulling speed V_P for SCN/C152 (C_∞ = 0.43wt%, G = 20.2K/cm). Experiment $\lambda_{0,exp}$ (O), the WL calculation of λ_0 (—), the most unstable mode λ_{max} from a steady state Mullins - Sekerka calculation (–·) and the two marginally stable modes under the Mullins - Sekerka steady state assumptions (···).

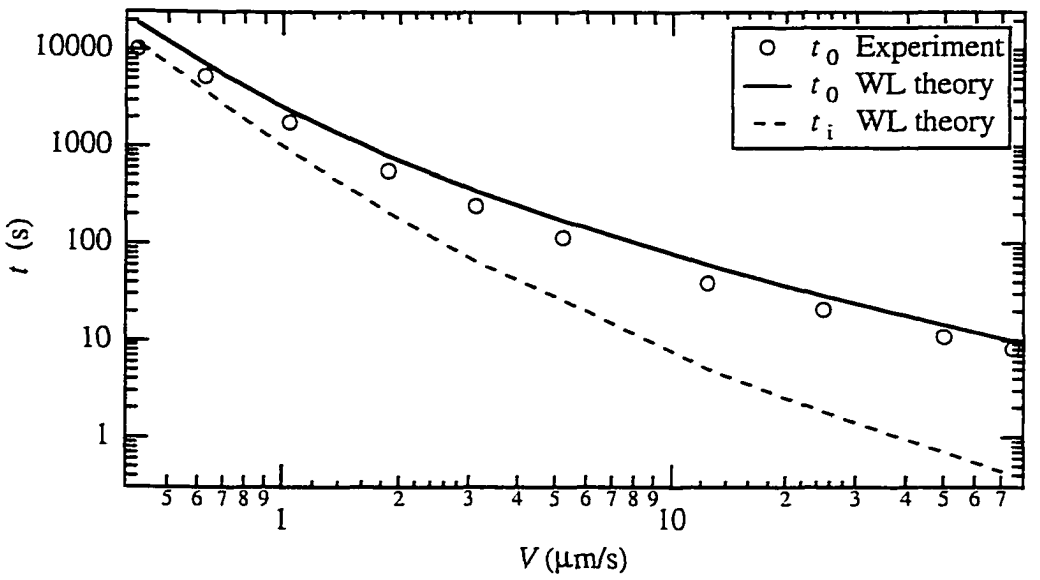

Figure 4.13: Comparison of the Warren-Langer theory and experiment for the crossover time t_0 as a function of pulling speed V_P for SCN/C152 ($C_\infty = 0.43$wt%, $G = 20.2$K/cm). Experiment $\lambda_{0,exp}$ (O) and the WL calculation of the crossover time t_0 (—) and the marginal stability time t_i (- - -).

culating the crossover wavelength $\lambda_{0,exp}$, and that $\lambda_{0,exp}$ is not very sensitive to the amplitude and power distribution of the initial noise at the start of the experiment. The most unstable mode predicted by the steady-state theory deviates significantly from the experimental data, indicating that the introduction of time dependence into the Mullins - Sekerka linear stability analysis by WL is clearly necessary. The other WL refinement of the Mullins - Sekerka analysis - the introduction of an initiation mechanism for the modulation together with the calculation of modulation amplitudes beyond t_i - is also necessary for the determination of λ_0, since the wavelength of the most unstable mode, both at t_i and t_0 (not shown), deviates from the experimental results as well. The marginal stability time t_i when one mode first becomes unstable provides a lower bound for the experimentally ob-

served planar-cellular crossover time $t_{0,exp}$, and the WL calculation of t_0 provides a good upper bound for the observed $t_{0,exp}$ since it assumes the smallest possible level of spontaneous perturbation (thermal noise).

4.4 Coarsening and the Approach to Steady State

The last stage of the development of a cellular or dendritic array is the coarsening of the initial shallow cellular structure with average wavelength $\lambda_{0,exp}$ into a final steady-state pattern. This stage, while crucial for the determination of the microstructure of the fully solidified alloy, is highly nonlinear and not well understood.

The initial cellular structure starts with an amplitude comparable to $\lambda_{0,exp}$ at the crossover time t_0 but quickly coarsens as cells overgrow their neighbors. Eventually, sidebranches start to appear behind the tips of the fastest growing cells which prevent other cells from growing further (see 1.4). Even though in the process the interdendritic spacing changes by approximately an order of magnitude, a reproducible selection of the final steady-state dendritic spacing is observed in experiments, where the pulling motor is started abruptly and kept at a constant pulling speed V_P.

Recent experiments, however, showed that the steady state growth conditions alone are not responsible for this selection [115]. A range of spacings was observed to be stable under the same steady state growth conditions, and the reproducible selection of one spacing out of this range of stable spacings was found to depend

on the experimental history (i.e. the sequence of pulling speeds preceding the final V_P). The Warren - Langer linear stability analysis for dendritic arrays (see section 2.5.2) showed that a uniform array at a given V_P is stable for a range of interdendritic spacings, and that outside of that range the array is most unstable against a doubling of the spacing [39]. Experiments on the range of stable dendrite spacings and the mechanisms limiting stability will be discussed in detail in chapter 5. For the coarsening process, important results from that chapter are:

- Reproducible selection of one array spacing has to occur during the planar-dendritic coarsening.

- Period doubling is the preferred way of coarsening[2].

To model the coarsening process, the position and wavelength of the modulated interface at the calculated crossover time is taken as the initial position and spacing of a 'dendritic' array. The rate of doubling of the spacing can be estimated from a modified Warren - Langer dendritic stability analysis [39]. The 'dendritic' array then evolves according to the calculated doubling rate until a steady state is reached. While this is a highly simplified model of the coarsening process, it is nevertheless capable of predicting the principal characteristics of the final steady-state array. In Figure 4.14 (adapted from [39]) the z-position of the plane of the dendrite tips (z_t/z_∞) is plotted schematically against the spacing between den-

[2]Period doubling was also observed to be the preferred coarsening mode in viscous fingering experiments [45].

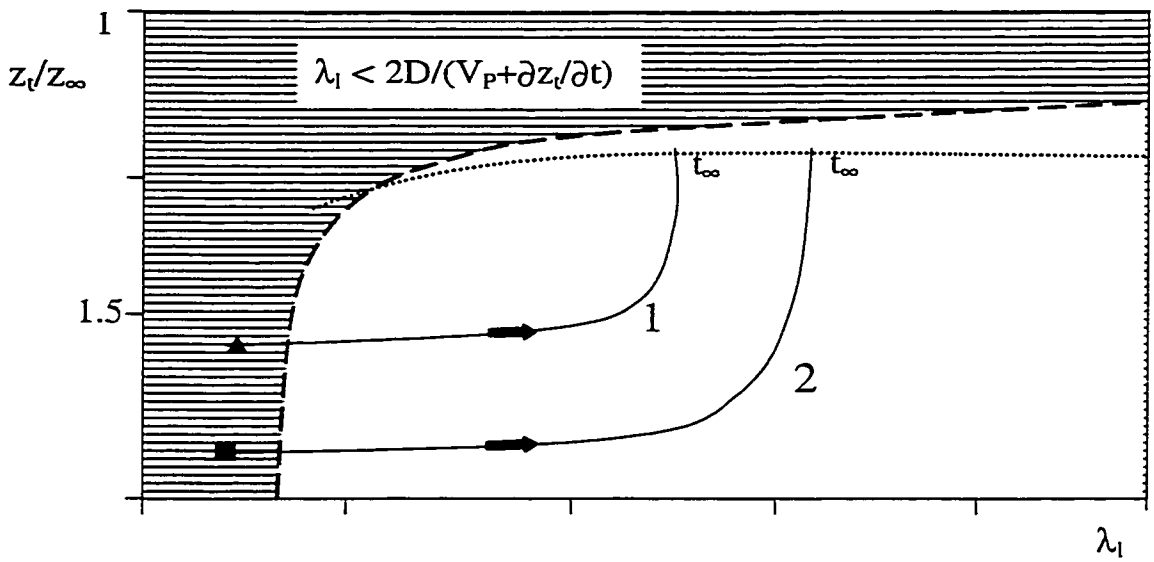

Figure 4.14: (Schematic) Warren-Langer calculation of the dynamics of the tip position z_0 as a function of interdendritic spacing λ_1. Full line 1 indicates the trajectory of the planar-dendritic transient. The dashed line denotes the limit of applicability of the theory. The dotted line marks possible steady state solutions for the dendritic array. Full line 2 shows another possible trajectory for different z_0 and λ_1 (adapted from [39]).

drites (λ_1). The solid line 1 denotes the calculated evolution of a dendritic array starting from the crossover wavelength λ_0 and position z_0 at the crossover time t_0 (denoted by the triangle). The WL dendritic stability analysis predicts that coarsening of the array spacing occurs faster than the approach to a steady state z-position, which occurs after the spacing has stabilized, as indicated by the sharp upward turn of the theoretical curve near the end of its trajectory. The steady - state position is at larger z (and therefore higher T) than the position during the crossover, indicating an increase in the crystallization temperature of the dendrite tips during the coarsening.

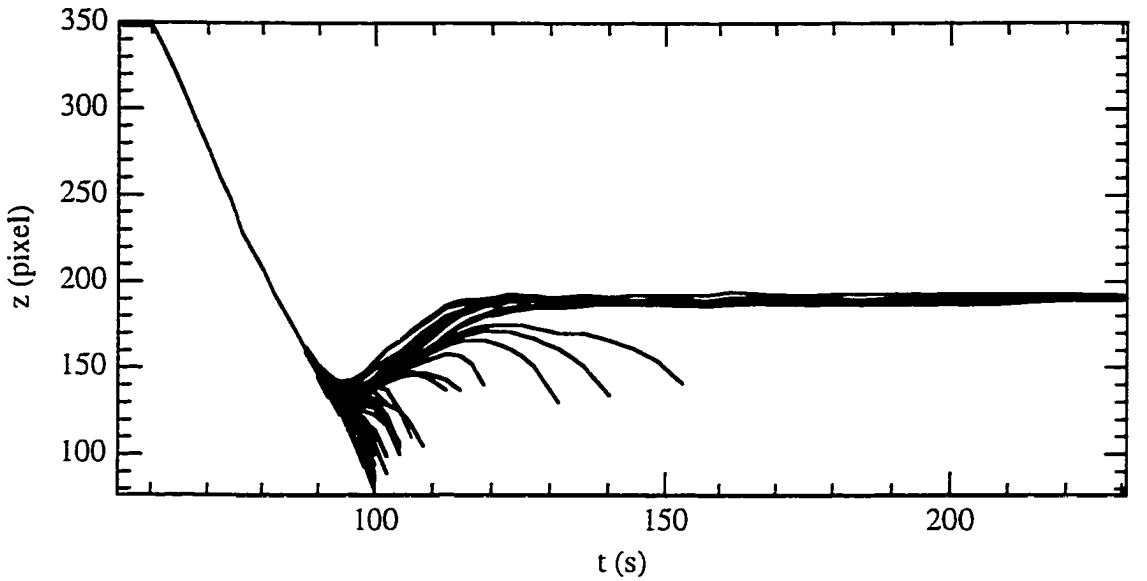

Figure 4.15: Position of the planar interface and positions of all dendrite tips during the cellular-dendritic coarsening. (SCN/C152 at $V_P = 24.91\mu$m/s, $C_\infty = 0.43$wt%, $G = 11.7$K/cm).

We have carried out preliminary experiments to measure the evolution of the dendrite tip positions and the spacing between dendrites during the coarsening. Since the temperature gradient in the experimental setup does not shift when the motor is started, we are able to measure the evolution of dendrite tip positions accurately. The spacing between dendrites, however, is not well defined since in the experiments the tips do not lie in one plane during the coarsening.

Qualitative comparisons to the WL predictions are still possible using the experimentally observed evolution of the individual tip positions as shown in Figure 4.15.

(After the crossover time, the lines separate to indicate the different positions of each dendrite tip.) Initially, the interface movement follows the WL calculation for a planar interface. The tip positions continue to move back when the instabil-

ity becomes observable, reach a minimum position and then move forward towards their final steady state position for a dendritic array without overshooting as predicted from the WL analysis. Dendrites that advance slowly are overgrown during the coarsening (indicated by lines that terminate) and never reach the steady-state position. Most of this coarsening takes place before any of the dendrite tips start to advance towards larger z, in agreement with the WL predictions, although some coarsening still takes place after all eventually surviving dendrites have reached their steady state z-position at $t \sim 120$s. All of the overgrown dendrites have already fallen behind at this time, and eventually stop growing and move back towards smaller z at the pulling speed.

One underlying assumption of the WL theory is that the coarsening dynamics are sensitive to the crossover wavelength and z-position. This dependence was studied in a series of experiments where the initial pulling speed was set to different values. before an instability occurred the pulling speed was switched to the same final value in all experiments and the subsequent initial instabilities and coarsening dynamics to a dendritic array were measured. Different crossover wavelengths and z-positions at the same final motor speed were observed and the coarsening was found to result in different final dendritic spacings.[3] A smaller z-position at the crossover time leads to a larger steady - state dendritic spacing as shown schematically in figure 4.14, by the line 2. While different interdendritic spacings can thus

[3]Using the same experimental procedure, Li *et al* [114] found that the cellular spacing also depends on the pulling speed history.

be reached during the coarsening under the same steady state conditions, the dendrite tip radius remains unchanged, dependent only on the steady state conditions. By selecting a sequence of pulling speeds to exploit the dynamics of the coarsening process, it is therefore possible to select (to a certain degree) these important characteristic lengthscales of the steady-state dendritic array independently.

4.5 Conclusions

We have investigated the evolution of a dendritic pattern in directional solidification experiments with the alloy SCN/C152, starting from a planar solid-liquid interface. Our experiments show that changes in the crossover wavelength λ_0 can affect the steady - state interdendritic spacing even though the wavelength of the pattern changes by approximately one order of magnitude during the coarsening. The focus of our experiments, therefore, was a detailed understanding of the initial instability from the initial recoil of the planar front after crystal growth is started until an instability becomes observable.

Initially, the planar interface remains morphologically stable until the marginal stability time t_i is reached. Planar interface stability was tested directly through applied spatially periodic UV perturbations which induce sinusoidal modulations of the interface profile. The growth or decay of the modulation amplitude (after the perturbation is switched off) allows for a measurement of positive or negative linear growth coefficients for a large range of wavevectors. This quantitative determination of interface stability shows that the interface becomes continually less

stable after crystal growth is started as the solute concentration builds up ahead of the advancing interface. The measured linear growth coefficients are in good agreement with the WL time-dependent linear stability analysis.

At t_i a transition from a negative to a positive linear growth coefficient is observed as perturbation-induced modulations start to grow. In unperturbed experiments, however, no instability is observable at t_i since the instability takes time to evolve far enough to become observable, starting from an unobservably small amplitude of noise-induced modulations. The evolution of the solute concentration field during the initial planar phase was also measured. The solute profile in the liquid ahead of the interface can be described well by an exponential with a time-dependent characteristic length in reasonable quantitative agreement with the WL calculations.

The measured wavelength at crossover (when instabilities become observable in an unperturbed experiment) is in good agreement with the WL time-dependent linear stability analysis and the crossover time shows fair agreement with the WL analysis. This indicates that the time dependence of the solute field and a reasonable estimate for the initial noise level must be included in the Mullins - Sekerka linear stability analysis in order to yield agreement with experimental data, while nonlinear terms are not necessary in the stability analysis.

Chapter 5

STABILITY OF DENDRITIC ARRAYS

What determines the interdendritic spacing λ_1 in an array of dendrites? Since microscopic solvability succeeded to describe the growth of a single dendrite tip, one can hope to understand their simplest pattern, a dendritic array. The interdendritic spacing λ_1, which is often more important in metallurgy than the shape of a single dendrite, will be the focus of this chapter.

5.1 Previous Studies on Dendritic Arrays

Detailed studies by Trivedi and coworkers, who started crystal growth from a planar front with constant pulling speed V_P, indicated that in steady state λ_1 is reproducibly determined by the growth conditions and changes smoothly with pulling speed V_P [31] or solute concentration C_∞ [32]. Such observations sug-

gested the existence of a dynamical selection mechanism for λ_1. Phenomenological model equations of the selected interdendritic spacing were subsequently developed among others by Trivedi [35], Lu and Hunt [36], and Kurz and Fischer [16]. The dendritic spacings obtained from these models show reasonable agreement with experimentally observed steady state dendritic spacings, when crystal growth is started from a planar front with constant pulling speed. However, no theoretical explanations for a dynamical selection mechanism were found.

Warren and Langer (WL) carried out a linear stability analysis of an array of dendrites as described in section 2.5.2, using microscopic solvability theory to describe individual tip shapes and calculating the interaction between tips from the solute diffusion field. WL found that no dynamical selection mechanism should exist, but a range of interdendritic spacings are allowed, and a period doubling instability limits the range for small spacings.

Subsequently, Huang *et al* [37] showed that if directional solidification is initiated at some V_P' until a steady state array develops and the pulling speed is then changed from V_P' to V_P, different values of λ_1 are found for the same final V_P, depending on the choice of V_P'. They showed that, for a given V_P, there is a range of λ_1 values observed whose lower limit lies close to the Warren-Langer prediction. Early experiments by Somboonsuk and Trivedi [116], where large changes in V_P were applied during the experiments, had already indicated that, if any selection mechanism for the dendritic spacing existed, it was very weak. In a more recent experiment Han and Trivedi [38] showed that once a dendritic array has been

established, V_P can be increased considerably without significantly changing λ_1.

In a recent study by Bouchard and Kirkaldy [41], experimental data of dendritic spacings in a variety of materials were compared to different phenomenological models. When the crystal growth speed remained unchanged during the experiment, the models work. Under unsteady state conditions on the other hand, when the crystal growth speed changed during an experiment, no agreement between the experimental data and the models was found for λ_1. The models, which were developed from experiments where V_P was not changed during crystal growth, thus seem to work just for that particular experimental history.

These experiments clearly demonstrate that λ_1 is **not** uniquely determined by the current growth conditions, and thus that no dynamical selection mechanism for λ_1 exists. The reproducible selection, observed in all experiments, therefore has to depend on the experimental history (the sequence of pulling speeds preceding the final V_P).

Fortunately one does not have to start from scratch to model an array of dendrites subjected to changes in pulling speed, because the other parameters of the array were found to be not dependent on the experimental history. The same study by Bouchard and Kirkaldy [41] that found history dependence in the dendritic spacing λ_1 also found that models describing the secondary spacing work under both steady state and unsteady state conditions. The radius of a dendrite tip also appears to depend only on the current growth conditions [1, 116].

In a real cast steady state growth conditions are usually not maintained for long,

as the cooling rate often varies throughout the cast. Since no dynamical selection mechanism exists, the phenomenological models can not easily be modified for non-steady state conditions. Instead, the dendrite spacing present when the dendritic array forms, the range of stable dendrite spacings and the instability mechanisms limiting that range are the important parameters for realistic simulations of cast processes.

5.2 Observation of the Period - Doubling Instability

[1]In collaboration with B.Q. Shi and J.A. Warren a new experimental directional solidification study was carried out, designed to quantitatively test the Warren-Langer prediction of a spatial period-doubling bifurcation shown in Fig. 2.6. Experiments were performed on Succinonitrile doped with $C_\infty = 0.43$wt% Coumarin 152 at $G = 11.7$K/cm.

The dendrite tip positions and the dendrite tip radius were extracted with better than pixel resolution from the videotapes using an earlier version of the pattern recognition algorithm described in section 3.5.3. To determine the interdendritic spacing, a rule about when to stop counting a dendrite has to be included. As shown in figure 4.15, dendrites stop growing completely once they have fallen behind sufficiently. In this experiment, when a dendrite tip fell back by two tip radii

[1]This section was adapted from my publication [1].

from the front of the array, it was no longer included.

The experiments followed a protocol suggested in [39]. The pulling speed V_P was set at 49.82 μm/s and maintained until a steady-state dendritic array consisting of $\sim$ 12 dendrites was established. The experiments were started from a grainboundary free planar interface, which leads to dendritic arrays with very uniform spacing in steady state. V_P was kept constant for 120s and was then decreased by 1.25μm/s every 30s.[2] As V_P was decreased, λ_1 remained nearly constant at $\sim$ 170μm until, at $V_P = 17.4\mu$m/s the array became unstable; every other dendrite fell back, and a doubling of the interdendritic spacing occurred. Figure 5.1(a) shows part of the array at $t = 420$s, fig. 5.1(b) at 1020s during the doubling instability, and fig. 5.1(c) at 1200s, after the spatially period-doubled array has restabilized. The time evolution of part of the array is presented in Fig. 5.2. Doubling did not always occur uniformly for the whole array. There was sometimes a time delay between the initial termination of growth for some dendrites and completion of the transition, probably due to slightly different local dendritic spacings. Dendrites that stopped growing became smooth as seen in Fig. 5.1(b).

Figure 5.2(a) shows V_P as a function of time with the instability indicated by a vertical arrow. Figure 5.2(b) shows the mean spacing $< \lambda_1 >$ with the rms spread in λ_1 indicated by the error bars.[3] Note that immediately after the doubling there

[2]The smallest step possible with our computerized motor drive and the gearhead used.

[3]Due to a slight tilt of the array the averages were taken over a shifting group of dendrites in the field of view which leads to small jumps in the spacing.

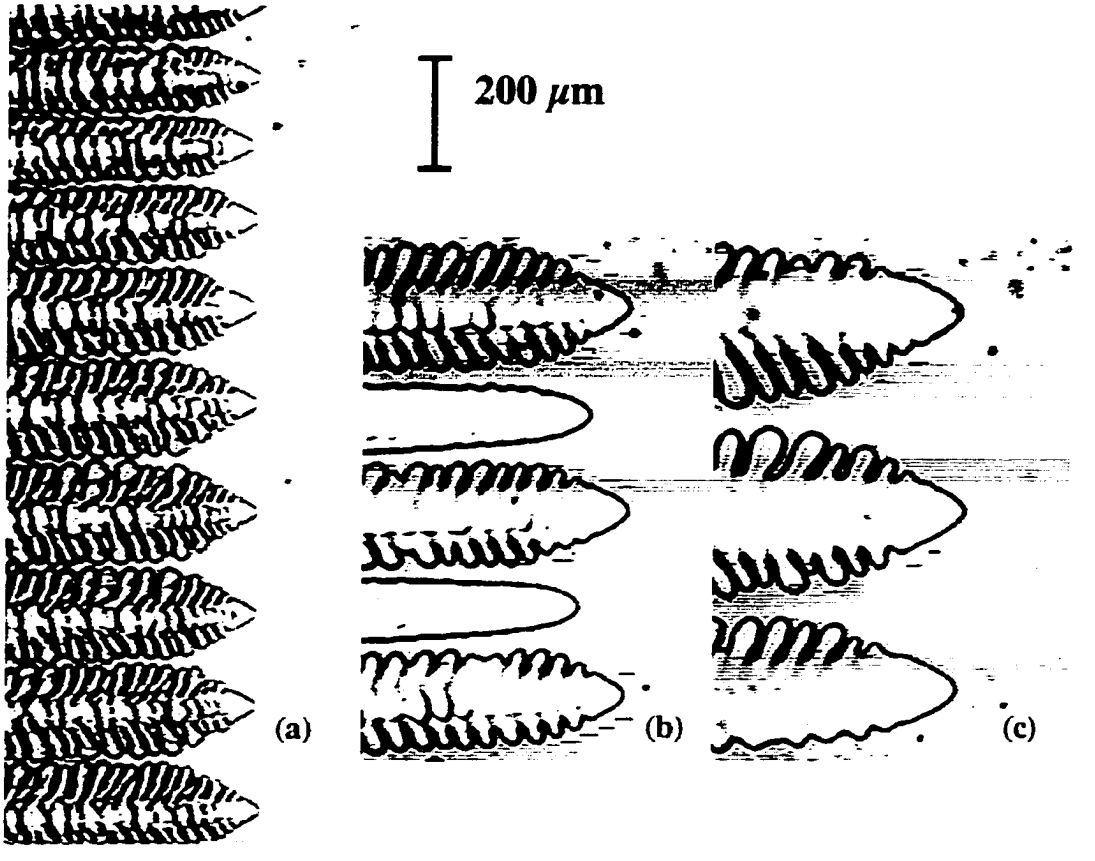

Figure 5.1: Images of the central region of the dendritic array (a) before, (b) during, and (c) following the spatial period doubling instability.

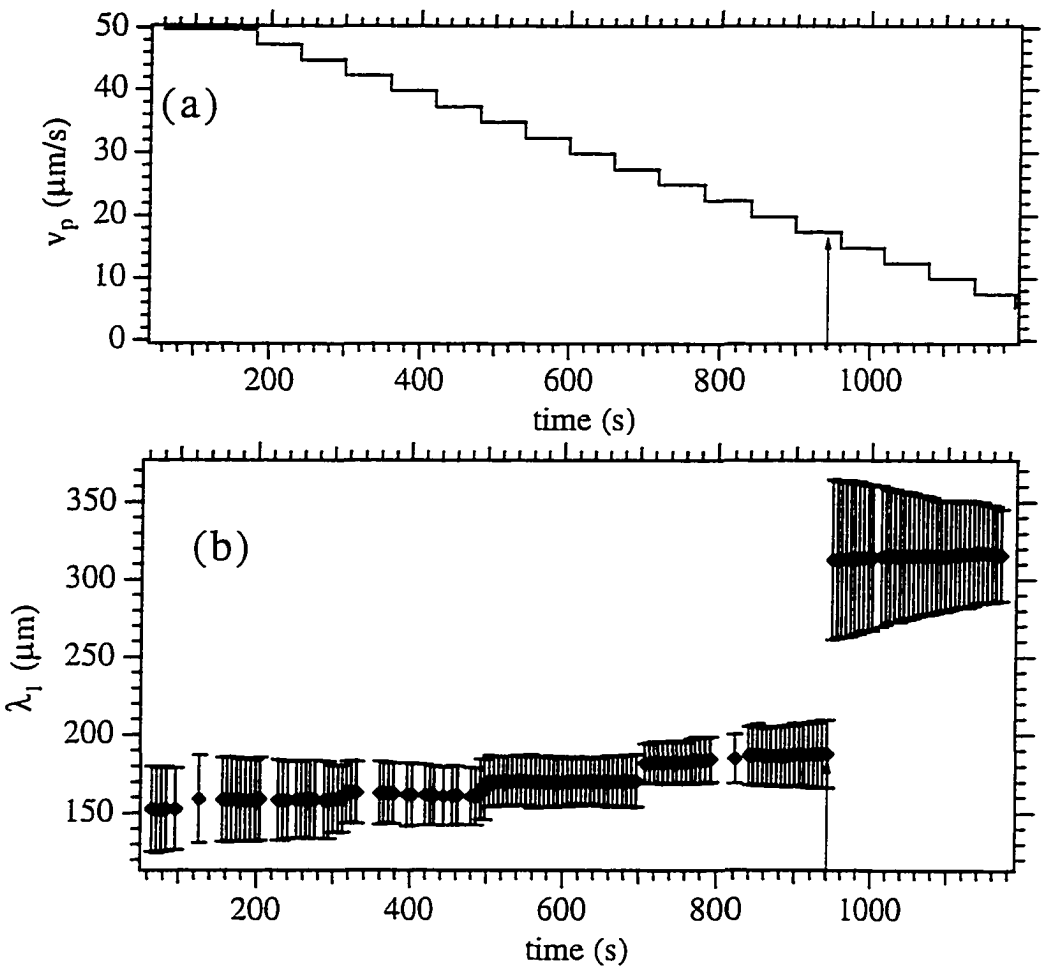

Figure 5.2: Dynamics of the dendritic array spacing under continuously decreased V_P. (a): Time dependence of the pulling speed V_P. (b): Mean value ($\diamond$) and rms spread (error bars) of λ_1 vs time.

is a large spread in λ_1 which gradually decreases by lateral shifting adjustments of the dendrite tips. This mechanism was previously reported by Han and Trivedi [38].

In order to test for quantitative agreement with the Warren-Langer predictions, the thermodynamic parameters of our SCN/C152 alloy are required. With the values listed in chapter 3.2.1, and with $\lambda_1 = 170\mu$m, the Warren-Langer analysis [40] produced the quantitative results for SCN/C152 similar to the one shown in Fig. 2.6. The stability limit against a spatial period-doubling transition is predicted to occur at $V_P = 13.7\mu\text{m/s}^4$, close to the experimentally observed value of 17.4μm/s. While uncertainty in the thermodynamic parameters and approximations in the theory suggest that the close quantitative agreement found here requires further study, it seems reasonable to conclude that the lower bound to the range of pulling speeds for which an array of given λ_1 is stable is determined by the spatial period doubling mechanism predicted by Warren and Langer.

5.3 Direct Measurement of Dendritic Array Stability

While the experiments in section 5.2 clearly established that period - doubling is the instability mechanism for an array of uniformly spaced dendrites of spacing λ_1, those measurements derived pattern stability from the observation of instabilities.

[4]The material parameters used are listed in chapter 3.2.1,which are improved over the estimates used in [1]

Similar to earlier measurements of planar interface stability described in chapter 4, instabilities are small close to the marginal stability limit and may not be captured by this kind of measurement, since the instability takes a long time to become observable. The pulling speed V_P at which a period - doubling instability is observed, can therefore only set a lower limit for the critical pulling speed $V_{PD}(\lambda_1)$, where the array of spacing λ_1 becomes morphologically unstable for a period - doubling instability.

In addition, some experiments on a dendritic array with nonuniform spacing showed that only the dendrite with the smallest nearest neighbor spacing stops growing (see [117], fig. 106), when the speed is reduced slowly. Is this apparent dependence on the local spacing consistent with period - doubling as the most unstable mode?

In this section we present direct measurements of the stability of a uniformly spaced dendritic array, including measurements on the influence of individual spacings near the onset of the instability. Dendritic array stability was determined through spatially periodic UV thermal perturbations of every other dendrite tip. The experiments, carried out in collaboration with J.M.A. Figueiredo and O.N. Mesquita, are still in progress, only preliminary results are reported here.

The experiments are carried out on one SCN/C152 sample with a C152 concentration of $C_\infty = 0.43$wt% in a thermal gradient of $G = 11.7$K/cm. The motor is started at $V_P = 19.8\mu$m/s and a uniformly spaced array of dendrites with spacing $\lambda_1 \approx 180\mu$m is established.

Unfortunately, while the dendrites are parallel to the z-axis, they are rotated by an angle of $\sim 20° - 30°$.[5] The tip positions on the other hand are in the same focal plane. The sidebranches therefore do not grow at each other. Preliminary unpublished experiments, shown in section 6.3, indicated that in this rotated geometry smaller dendrite spacings are obtained. This dependence on the sidebranch orientation is one probable cause for the quantitative difference of the results in this section to the measurements in the preceding section that were carried out more than two years earlier on the same sample at the same temperature gradient, but yielded larger steady state spacings. Contamination or natural degradation of the material is another possibility, but the dendrite tip radius and the spacing between sidebranches did not change noticeably between both experiments, only the dendrite spacing changed. Therefore only a qualitative comparison to the Warren - Langer linear stability analysis was carried out here, but the uncertainty in sample parameters does not affect the important results on the nature of the instability and the behavior near marginal stability.

Two methods were used to improve the uniformity of the array. In many experiments, one row of UV spots with the same spacing as the dendrite tips was focused along the tips, such that the spots were offset with the tips by half the dendrite spacing. This method ("Oscar's comb") speeds up the lateral adjustment of tip

[5]The rotation angle can be calculated approximately from the position of two sidebranch tips that grow at a 90° angle, if the sidebranches are close enough to the dendrite tip to not touch the capillary wall yet.

positions observed in unperturbed experiments and yields very uniform arrays, but requires a fairly uniform array to start with. To obtain lateral adjustment toward a fairly uniform array, the pulling speed was lowered in some experiments to just above the period - doubling instability, since the natural lateral adjustment process is faster at lower speeds for the same spacing. After a fairly uniform spacing developed the speed was increased again to its previous value.

When the uniform array of spacing λ_1 has reached steady state (i.e. neither the radius ρ nor the z-position of the dendrite tips shifts), a row of high intensity UV spots with a uniform spacing $\lambda = 2\lambda_1$ is applied to the tip of every other dendrite for a time T_P. This melts every other dendrite back by an average amount $\bar{\xi_T}(T_P)$ relative to the tips that are not perturbed directly, creating a spatially periodic modulation of the dendrite tip positions with wavelength λ and amplitude $\bar{\xi_T}$. When the UV light is switched off, the directly perturbed dendrites catch up with the rest of the array (if the array is stable against the period - doubling instability). After steady state is reached again, the pulling speed V_P is reduced in small steps. After each step, as soon as the new steady state is reached (with the same dendrite spacing as at higher speed), the UV perturbation is applied. This process is repeated until an instability is observed, which changes the spacing between dendrites.

Figure 5.3 shows one perturbation measurement. The steady state array of dendrites at [1:59:59] (time in [hour:minute:second]), is perturbed for one minute (at [1:06:00], not shown). The UV perturbation, appearing as bright circles on top

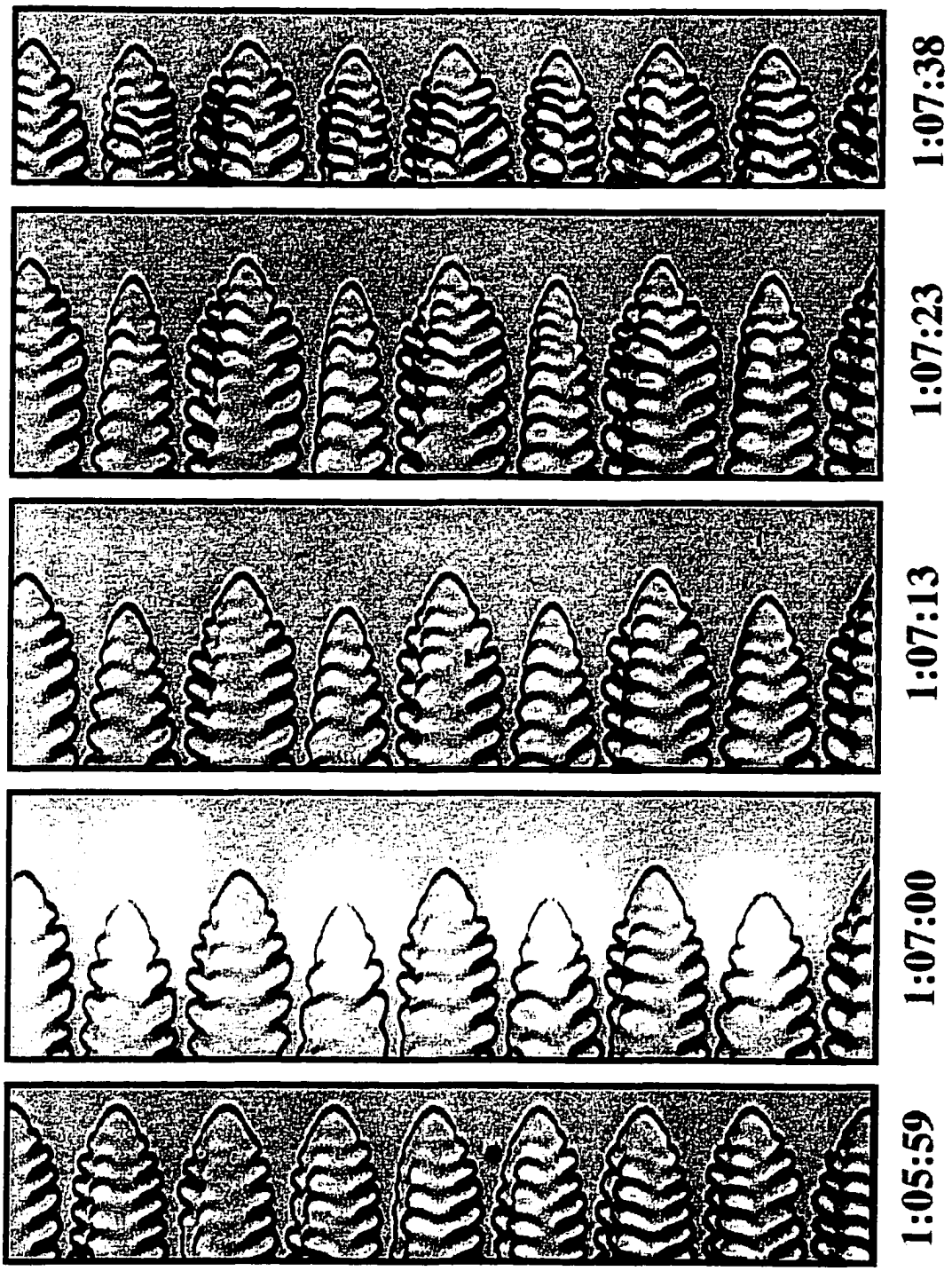

Figure 5.3: Image sequence (time in [hour:min:sec]): Growth and decay of spatially periodic modulations of the tip positions in a uniformly spaced dendritic array. Modulations created through a one minute UV-thermal perturbation applied at 1:06:00. (SCN/C152: $V_P = 8.2\mu$m/s, $C_\infty = 0.43$wt%, $G = 11.7$K/cm.)

of every other dendrite, create a spatially periodic modulation of the tip positions [1:07:00]. After the perturbation is switched off (at [1:07:00], not shown), the perturbed tips start to catch up quickly with the rest of the array at [1:07:13] and [1:07:23], and all dendrites reach steady state at [1:07:38].

The decay of the modulation amplitude $\bar{\xi_T}(\lambda, t)$ can be described in weakly nonlinear approximation as:

$$\frac{d\bar{\xi_T}(\lambda,t)}{dt} = a_0(\lambda)\bar{\xi_T}(\lambda,t) + a_1(\lambda)\left|\bar{\xi_T}(\lambda,t)\right|^2\bar{\xi_T}(\lambda,t) \tag{5.1}$$

In linear approximation, $\bar{\xi_T}$ decays exponentially with a decay rate $a_0(\lambda)$, which is the rate calculated in the Warren - Langer linear stability analysis for a dendritic array (see section 2.5.2).

Superimposed on this modulation with $\lambda = 2\lambda_1$ is a uniform meltback of all dendrites ($\lambda = \infty$) caused by fast diffusion of the absorbed heat during UV illumination. In first approximation we assume that the two modes of the perturbation with $\lambda = 2\lambda_1$ and $\lambda = \infty$ are independent. This yields results very consistent with the weakly nonlinear analysis, but eventually the interaction between modes may have to be included.

Figure 5.4 shows a semilog plot of the modulation amplitude, i.e. the difference between perturbed and unperturbed dendrite tip positions $\bar{\xi_T}(2\lambda_1, t)$, after a 20 second perturbation was applied to every other tip at $V_P = 9.86\mu$m/s. The spacing between dendrites in this experiment was $\lambda_1 \approx 150\mu$m. The modulation amplitude decays exponentially with a negative linear growth coefficient of $a_0(\lambda = 2\lambda_1) = -0.072\text{s}^{-1}$.

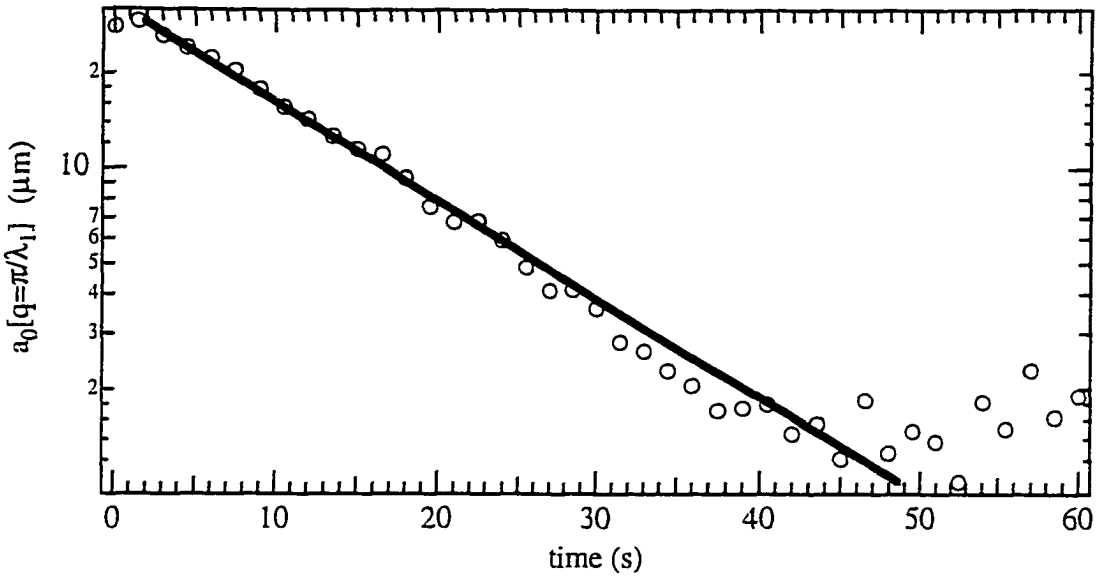

Figure 5.4: Average difference in the dendrite tip position between perturbed and unperturbed dendrites vs time (o), and exponential fit (—) in the range $t = 0 - 52$s ($a_0(\lambda = 2\lambda_1) = -0.072\text{s}^{-1}$). Modulation produced by a spatially periodic UV thermal perturbation with $\lambda \approx 300\mu$m applied for 20 seconds, which melted back every other dendrite tip. (SCN/C152: $V_P = 9.86\mu$m/s, $C_\infty = 0.43$wt%, $G = 11.7$K/cm.)

The negative linear growth coefficient of a period doubling modulation for that same array of dendrites was obtained at many different V_P, as described above. Figure 5.5 shows the growth coefficient as a function of pulling speed. From this plot we can estimate that marginal stability against period doubling ($a_0(\lambda = 2\lambda_1) = 0$ is reached at $V_P \approx 4\mu$m/s. A preliminary unperturbed experiment showed that an array of that spacing does indeed become unstable at approximately $V_P \approx 4\mu$m/s.

The growth coefficients for each individual dendrite tip of this uniformly spaced array were also measured for some data points. They were found to be approximately the same, within the uncertainty of the individual fits.

In these experiments the period doubling instability occurred close to the cel-

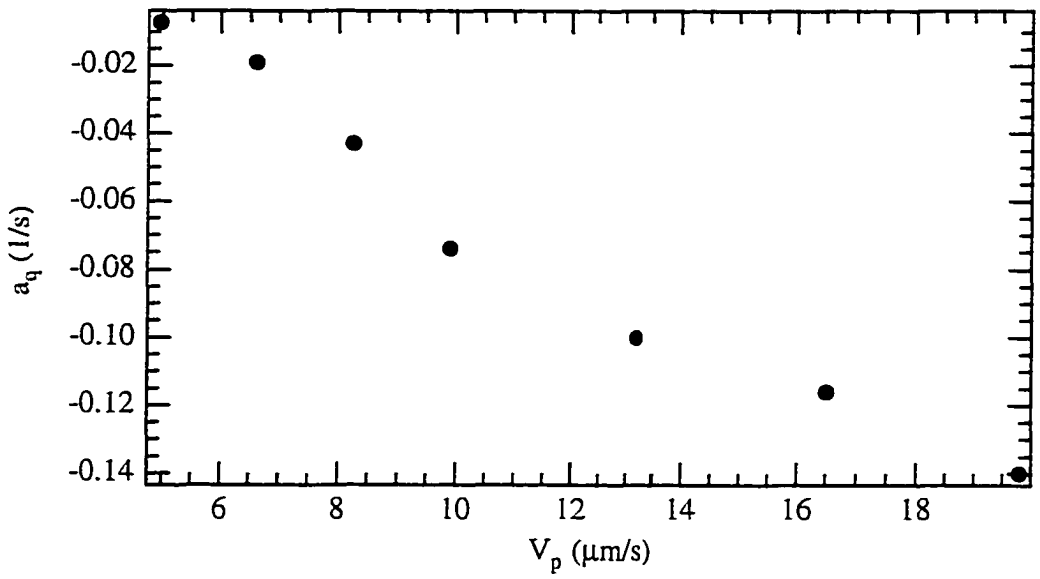

Figure 5.5: Negative linear growth coefficient vs V_P for an interdendritic spacing of $\lambda \approx 150\mu$m. $\omega(\lambda = 2\lambda_1)$ is measured from the decrease in difference in dendrite tip position after every other dendrite tip is melted back. (SCN/C152: $C_\infty = 0.43$wt%, $G = 11.7$K/cm.)

lular regime, so all measurements near marginal stability are in the cell to dendrite transition region. Near marginal stability the linear coefficient becomes small and nonlinear terms should be included in the analysis. When the third order term is included in equation 5.1, one obtains:

$$\bar{\xi_T}(\lambda, t) = \left(\sqrt{\left(\frac{a_1(\lambda)}{a_0(\lambda)} + \bar{\xi_T}(\lambda, 0)^{-2} \right) e^{-2a_0(\lambda)t} - \frac{a_1(\lambda)}{a_0(\lambda)}} \right)^{-1} \tag{5.2}$$

At this speed close to linear marginal stability, small changes in individual spacing between dendrites become important, as they slightly shift the marginal stability point. The quantitative analysis of nonlinear effects was therefore carried out at $V_P = 9.86\mu$m/s on three individual dendrite tips in a perturbed array whose nearest neighbor spacing deviated from one another by less than 2%. Figure 5.6 shows the absolute difference in position of each of those three dendrite tips relative

to its nearest neighbors. The curves where offset on the time axis to show, that the relaxation follows the same curve, independent of amplitude. Exponential fits (- - -) to the smallest amplitude tip (O) gave a relaxation rate of $a_0 = 0.091\text{s}^{-1}$. The full third order function (Eqn. 5.2)(—) can be fit well to both large amplitude modulations (×, +) and to the small modulation and yields $a_0 = -0.090\text{s}^{-1}$ and $a_1 = 1.1 \times 10^{-5}\mu\text{m}^{-2}\text{s}^{-1}$. This gives a threshold perturbation amplitude of $\sqrt{a_0/a_1} \approx 100\mu\text{m}$. Indeed, a subsequent larger perturbation created a modulation amplitude of $\sim 130\mu\text{m}$ that did not decay but lead to an instability.

We conclude, that period doubling in dendrites close to the cellular regime is subcritical. The subcritical range is large, since the forced transition was observed at more than twice the speed of an spontaneous transition. Our measurements also indicate that the decay of modulation amplitudes that reach up to 50% the dendrite spacing can be described well by a linear approximation. A third order analysis is needed only for large amplitudes close to the instability.

The subcritical nature is illustrated in figures 5.7 and 5.8, which show two consecutive perturbations applied at the same pulling speed $V_P = 4.95\mu\text{m/s}$. The first perturbation (fig. 5.7) was brief (1 min), creating a small modulation amplitude. The second perturbation (fig. 5.7) was longer (2 min), creating a larger modulation amplitude. While the small amplitude decayed, the large amplitude induced a period doubling instability from an almost cellular array with barely visible sidebranching to a well developed period doubled dendritic array.

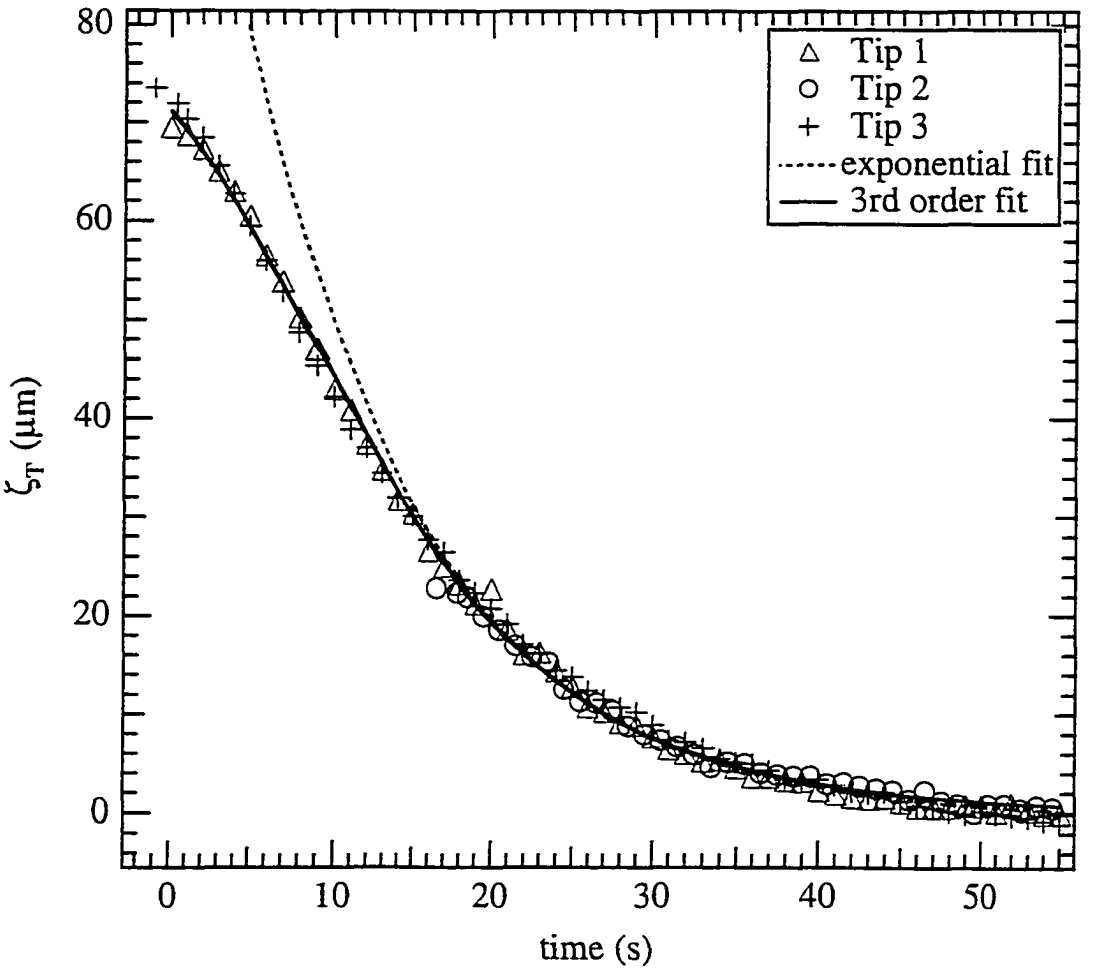

Figure 5.6: Nonlinear fitting of the modulation amplitude: Exponential fits (- - -) to the smallest amplitude tip (O) (relaxation rate of $a_0 = 0.091\text{s}^{-1}$) and third order fit (—) to both large amplitude modulations (×, +) and to the small modulation ($a_0 = -0.090\text{s}^{-1}$, $a_1 = 0.00011\mu\text{m}^{-2}\text{s}^{-1}$). (SCN/C152: $C_\infty = 0.43$wt%, $G = 11.7$K/cm, $V_P = 9.86\mu$m/s.)

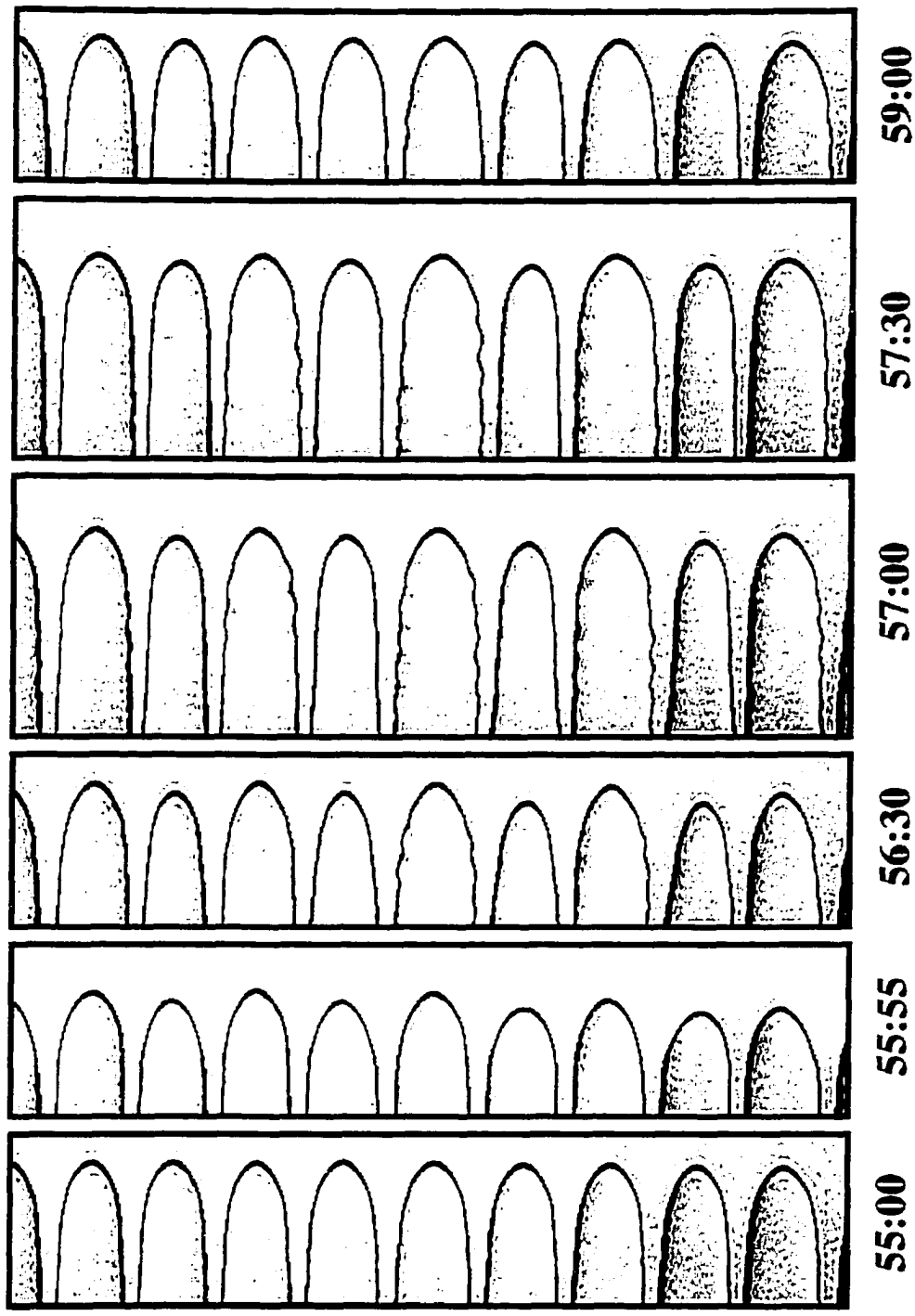

Figure 5.7: Image sequence: Growth and decay of small spatially periodic modulations of the tip positions in a dendritic array. (Modulation created through a UV-thermal perturbation applied at 55:00 min for 1 min.) (SCN/C152: C_∞ = 0.43wt%, $G = 11.7$K/cm, $V_P = 4.95\mu$m/s.)

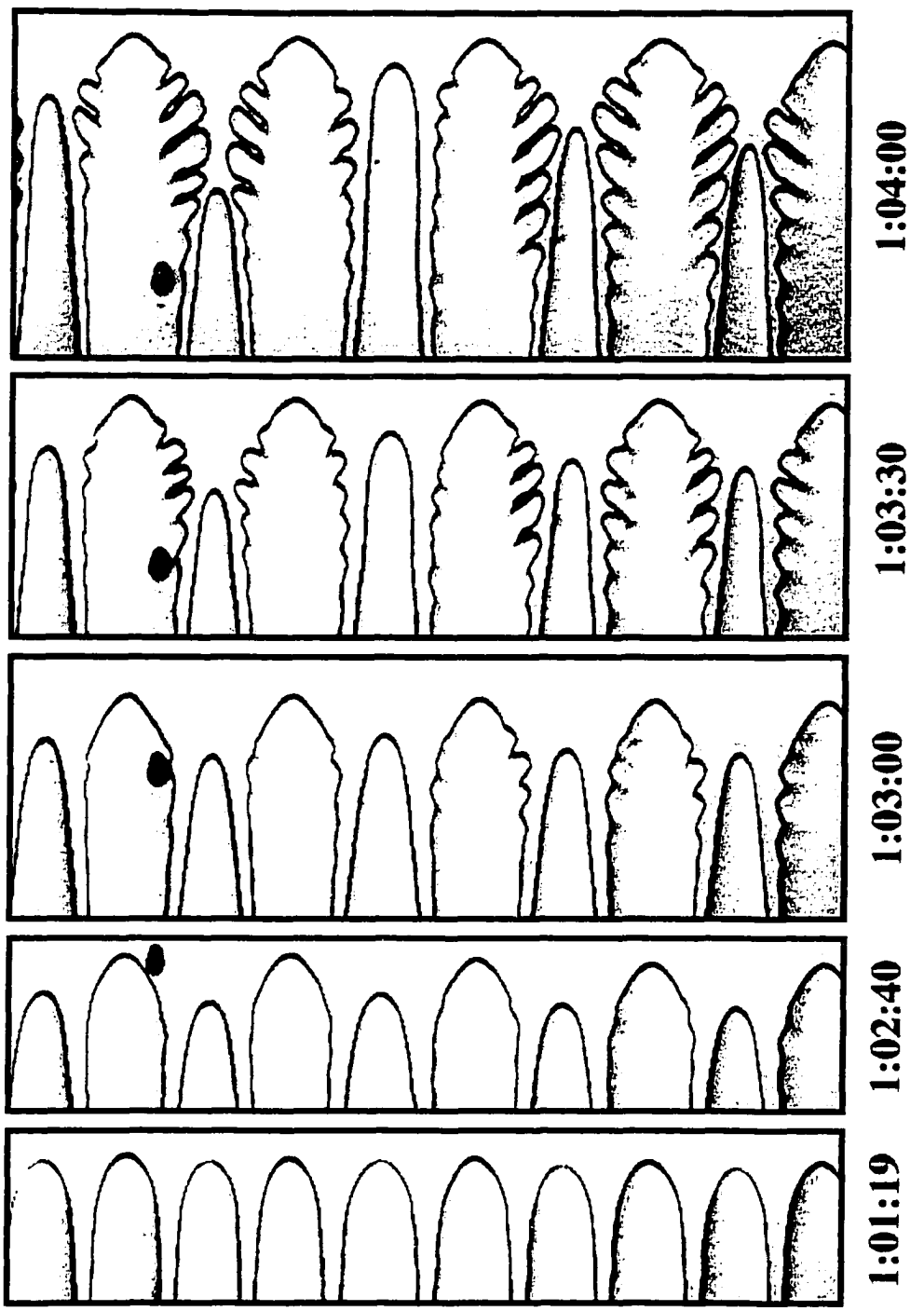

Figure 5.8: Image sequence: Period doubling induced through large spatially periodic modulations of the tip positions in a dendritic array. (Modulation created through a UV-thermal perturbation applied at 1:01:00 min for 2 min.) (SCN/C152: $C_\infty = 0.43$wt%, $G = 11.7$K/cm, $V_P = 4.95\mu$m/s.)

5.4 Nonuniform Arrays of Dendrites

The individual tips in an array of dendrites interact through the solute diffusion field. The diffusion length $\ell = 2D/V_P$, however, is smaller than the spacing between dendrite tips. At most, the diffusion length becomes roughly equal the dendrite spacing near the cell - dendrite transition, where some of the experiments were carried out. In a uniformly spaced array, this short diffusion length appears to favor a period doubling instability rather than a longer wavelength instability, where for example every third dendrite falls back, since the dendrites can only interact very weakly over longer distances.

In addition, a short diffusion length also means that the interaction between dendrites is very localized. The separation from its nearest neighbors therefore should be an important parameters for the stability of any one dendrite. For arrays of dendrites with very nonuniform spacing[6], this can lead to the elimination of the dendrite with the smallest spacing relative to its neighbors. Figure 5.9 shows individual dendrite spacings in an initially very nonuniform array of dendrites, when V_P is decreased in continuous small steps. The spacings for two experiments (+,O) that followed the same protocol overlap. It can be noticed that the smallest dendrite spacings disappear first, indicating the meltback of the dendrite with the nearest neighbors. The range of dendrite spacings covers a factor of two and is

[6]Grainboundaries, present at the planar interface during the start of growth, give cells next to the grainboundary an advantage in the coarsening process, which leads to a nonuniform spacing between dendrites when the array is established.

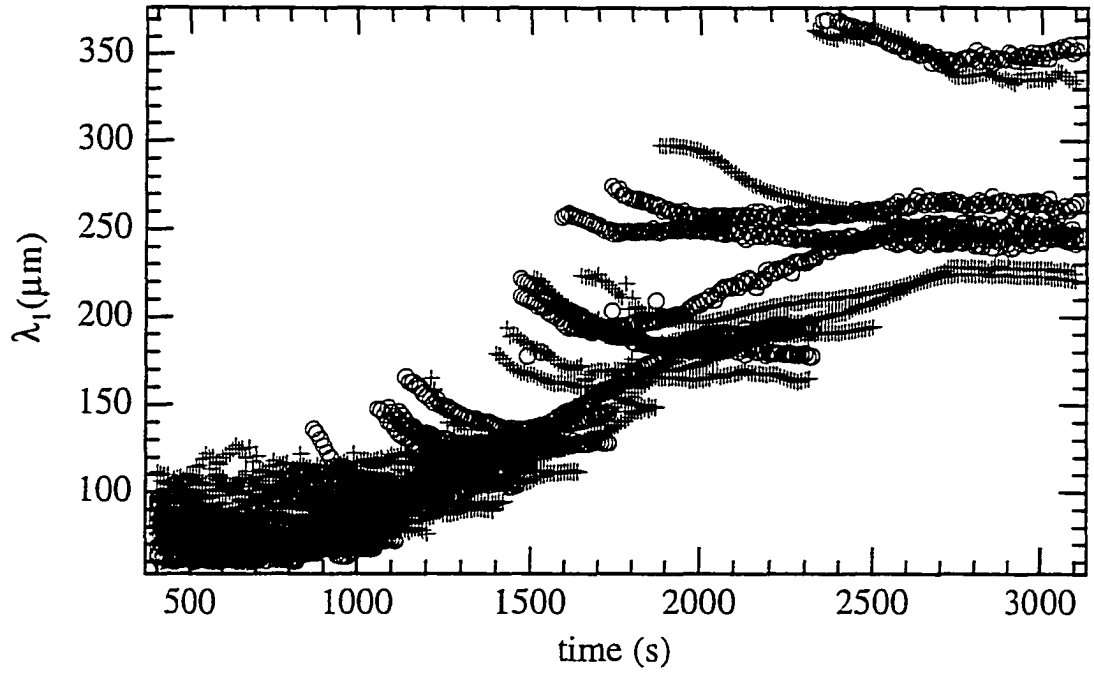

Figure 5.9: Individual dendrite spacings in a nonuniform array under rapid decrease in V_P in two experiments (+,O) with the same protocoll. (SCN/C152: C_∞ = 0.37wt%, $G = 5.4$K/cm, $V_{P,Start} = 49.8\mu$m/s.)

reproducibly mapped out in both experiments.

Chapter 6

CELL TO DENDRITE TRANSITION

One unsolved problem in directional solidification of binary alloys is the nature of the cell to dendrite transition and the observed associated increase in spacing at the transition from cells to dendrites (as observed e.g. by Trivedi [31]).

At intermediate crystal growth speeds V_P, when the solid-liquid interface pattern consists of cells, the cell spacing decreases roughly as $V_P^{-1/2}$ [118] with increased pulling speed (measured in experiments, where the motor was started at V_P and the cell spacing was recorded). At high crystal growth speeds dendrites are observed with dendritic spacings roughly decreasing as $V_P^{-1/4}$ [118] (also obtained in experiments where crystal growth is started at V_P), but in the cell to dendrite transition region an increase in spacing is observed in many experiments [35, 117]. The nature of the transition is not fully understood, but in some experiments

both cells and dendrites were observed simultaneously, indicating that there is a continuous transition between cells and dendrites.

In this chapter we will review the current understanding of the cell - dendrite transition and report new experimental data that might help to explain its nature. In particular, the role of sidebranches in the observed increase in spacings at the cell - dendrite transition will be examined.

6.1 Current Understanding

The cell to dendrite transition is determined in most experiments from the visibility of sidebranching [38, 31] or from the persistence of sidebranch features in the bulk [119]. Kurz and Fisher's [16] equation ($V_{\text{Cell}-\text{Dendrite}} = V_C/k$) provides a rough estimate for the transition. However, it is observed that the transition point is history dependent and shows hysteresis [83]. This indicates that the dynamics play an important role in the cell to dendrite transition. Trivedi *et al* [31, 38] found that the cell to dendrite transition depends only on the local spacing between cells. A sufficiently large spacing between cells allows sidebranches to occur, so that a nonuniform array of cells can show both cellular and dendritic features [38].

New numerical simulations by Kopczyński and Rappel [85] use a quantitatively accurate phase-field model [120, 85] to simulate the start of directional solidification for a large number of cells from a planar front until steady state is reached. The steady state cell and dendrite spacings reached in these simulations exhibits the experimentally observed scaling of λ_1 vs V_P, but shows no increase in spacing at

the cell - dendrite transition. Dendrites are discerned from cells by Kopczynski *et al* through the tip shape, since the simulations did not include thermal noise, which leads to dendrites without sidebranches.

These simulations together with experiments reported in the following sections suggest, that sidebranches not only result from an increased spacing as observed by Han and Trivedi [38] but could be triggering the increase in spacing.

6.2 Forced Cell-Dendrite Transition

In the first experiment the cell to dendrite transition is triggered through UV-thermal perturbations, similar to the new experiments shown in figure 5.8. The SCN/C152 sample with $C_\infty = 0.43$wt% is used in a temperature gradient $G = 20.2$K/cm. A cellular array is formed by setting the pulling speed to $V_P = 41.6\mu$m/s for 10 min. until a steady state dendritic array forms and reducing the speed to $V_P = 6.24\mu$m/s, still above the spontaneous period - doubling instability so that a steady state cellular array with $\lambda_1 \approx 92\mu$m forms. To verify that the cell walls are stable against sidebranching a UV-thermal perturbation is applied to the tip region of the stable row of cells for 1s every 10s. Figure 6.1(a) shows the unperturbed cellular array after 51 min. and figure 6.1(b) the array during the periodic perturbations (at 61 min.). Sidebranch modulations, triggered by the periodic perturbations, are observable close to the tip, but decay as they move into the groove.

To induce a period doubling instability a higher intensity UV spot is applied

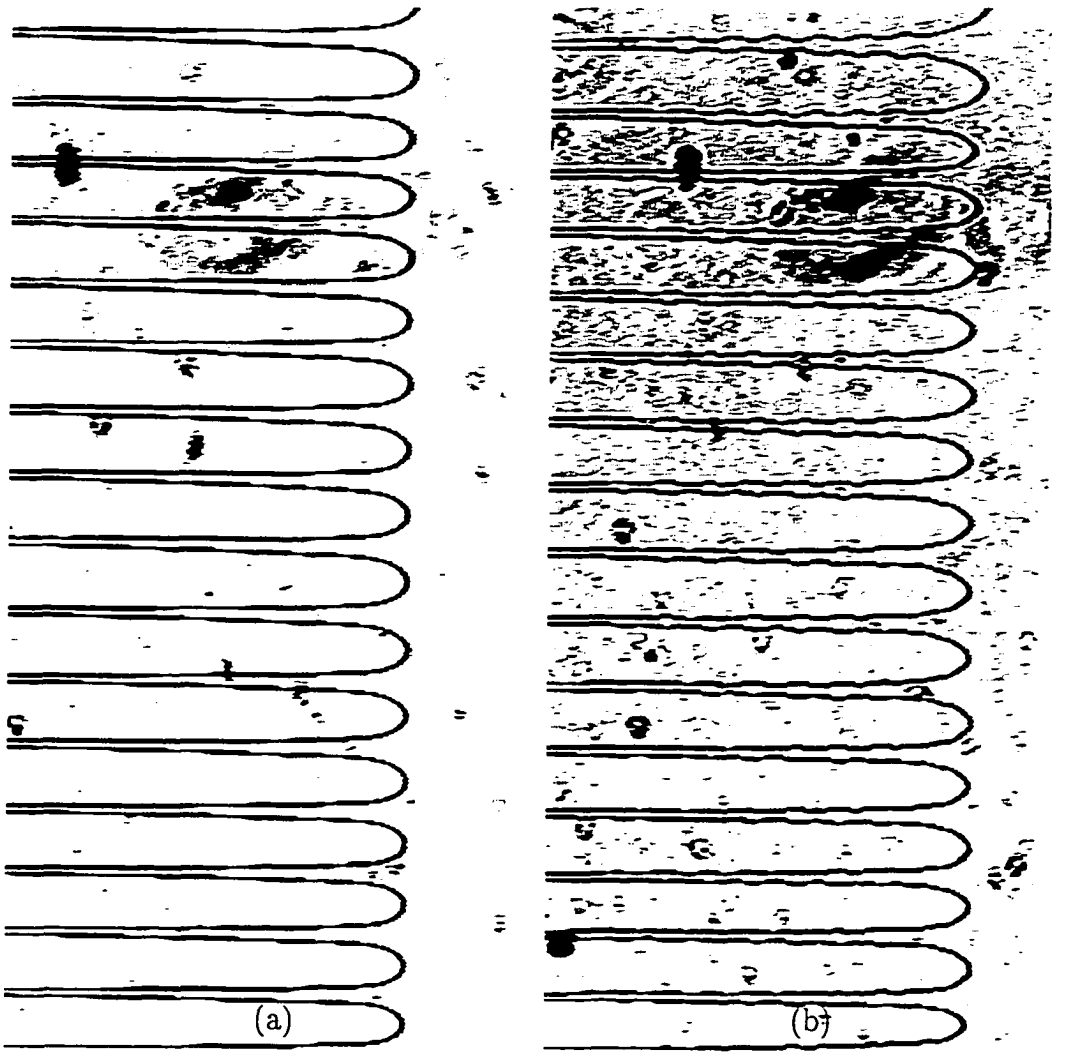

Figure 6.1: Stability of the cell walls against perturbations. Array of cells of SCN/C152 ($C_\infty = 0.43$wt%, $V_P = 6.24\mu$m/s and $G = 20.2$K/cm). (a) unperturbed and (b) with a 1s perturbation applied every 10s.

to every other cell tip thereby melting it back sufficiently to be overgrown by the neighboring cells, similar to figure 5.8.

This results in a doubling of the spacing. The new spacing is observed to be stable and the cells exhibit natural sidebranches triggered by noise without external periodic perturbations, which qualifies the pattern as dendritic under most definitions. The difference between both stable patterns (under the same

steady-state growth conditions) is that for dendrites the tip region is unstable against thermal perturbations while it is stable for cells.

This experiment shows that both cells and dendrites are stable under the same solidification conditions. In addition, these experiments could be used to quantitatively determine the stability of the cellular sidewalls against perturbations when the spacing between cells is small.

6.3 "Sidebranch Free" Dendritic Arrays

In our experiments we attempt to test whether the existence of sidebranches can explain the observed increase in spacing at the cell to dendrite transition. Since we can not eliminate thermal noise experimentally to obtain dendrites without sidebranches, we have to find another way to eliminate the effect of sidebranching on the interdendritic spacing. Experiments are usually carried out on a row of dendrites, where the sidebranches face each other and the sidebranch pattern looks like $(+ + +)$ if it is growing at the observer. In order to eliminate the effect of sidebranches on the interaction between neighboring cells, we rotated the crystalline axis by 45 degrees so that the sidebranch pattern looks like $(\times \times \times)$ if it is growing at the observer. The crystalline axis was rotated by selecting a grain with that orientation during the grain selection procedure described in section 3.2.2. The sidebranches now grow into the wall not toward each other, so while they are not eliminated they no longer interact strongly with any other dendrite.

Fig. 6.2 shows a $(+ + +)$ pattern and fig. 6.3 a $(\times \times \times)$ pattern, both at the

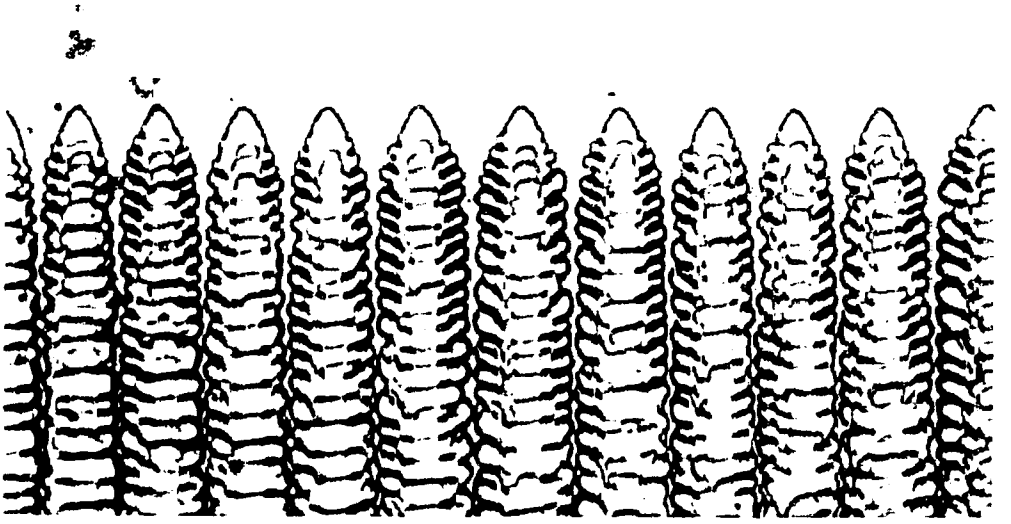

Figure 6.2: Array of $(+++)$ dendrites ($G = 20.2$K/cm, $C_\infty = 0.43$wt%, $V_P = 24.9\mu$m/s)

same V_P. While a closer analysis of the images shows that the dendrite tip radius and the sidebranch spacing is approximately the same in both experiments, the interdendritic spacings are very different.

One of the causes for the different spacings appears to be the influence of sidebranching on the coarsening dynamics. Figure 6.4 shows a $(+++)$ array during the initial coarsening 29 seconds after the motor is started. One can observe that sidebranches overgrow some cells during the coarsening. In the $(\times\times\times)$ the influence of sidebranches on the coarsening dynamics is minimized, since sidebranches can not hinder neighboring cells from growing during the coarsening process. Figure 6.5 shows the initial coarsening after 29 sec. at the same time and under the same conditions as in figure 6.4.

For both the $(+++)$ and the $(\times\times\times)$ geometry the motor is started abruptly at different V_P and the initial instability time, the initial instability wavelength

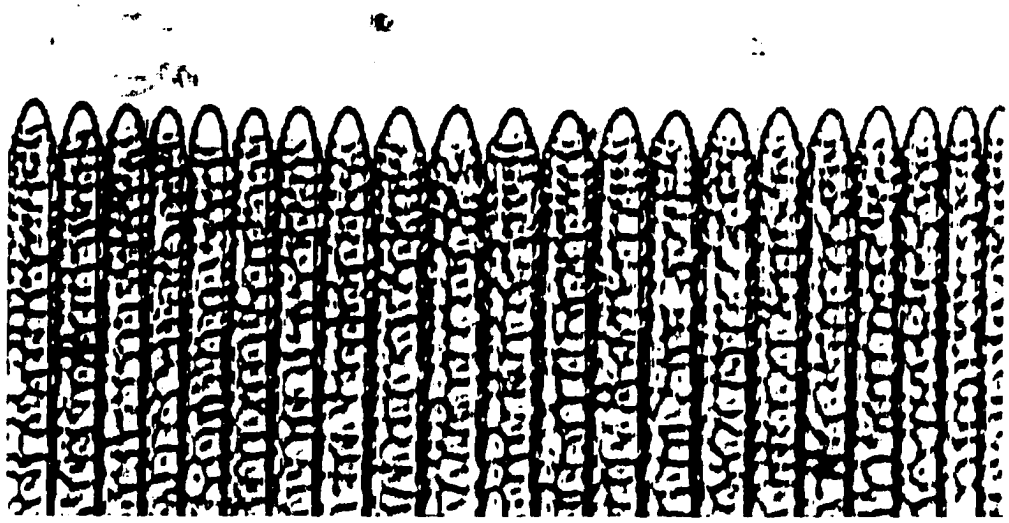

Figure 6.3: Array of ($\times$ $\times$ $\times$) dendrites (same conditions as in figure 6.2).

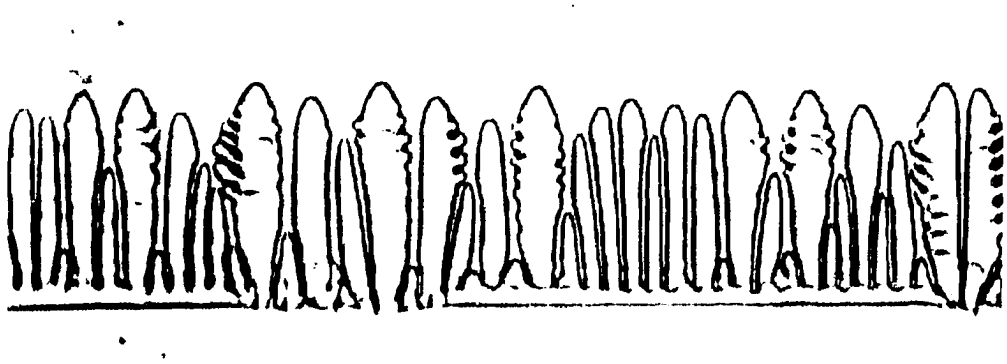

Figure 6.4: (+++) dendrites: Overgrowth of cells by sidebranches during the initial coarsening 29 seconds after the motor is started. ($G = 20.2$K/cm, $C_\infty = 0.43$wt%, $V_P = 24.9\mu$m/s)

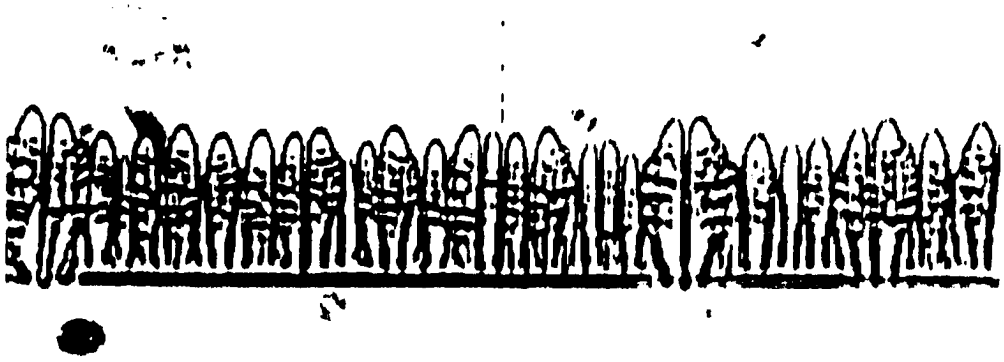

Figure 6.5: $(\times \times \times)$ dendrites: Overgrowth of cells by sidebranches during the initial coarsening 29 seconds after the motor is started. (same conditions as in figure 6.4).

and the final steady state spacing λ_1 are recorded.

The initial instability wavelength and time show no signs of dependence on the crystalline orientation within the accuracy of the experiment. The cellular and dendritic spacings, shown in figure 6.6, on the other hand show an increase in spacing by a factor of ≈ 2 at the cell to dendrite transition (at $\approx 3 - 5\mu$m/s) for $(+++)$ dendrites as previously reported by Trivedi. For $(\times \times \times)$ dendrite no such increase is observed.

6.4 Conclusions

A smaller dendrite spacing is observed for $(\times \times \times)$ dendrites under otherwise identical conditions with $(+ + +)$ dendrites. In agreement with phase field computer simulations without sidebranch interaction by Kopczinski and Rappel [85] no increase in spacing was observed at the cell to dendrite transition.

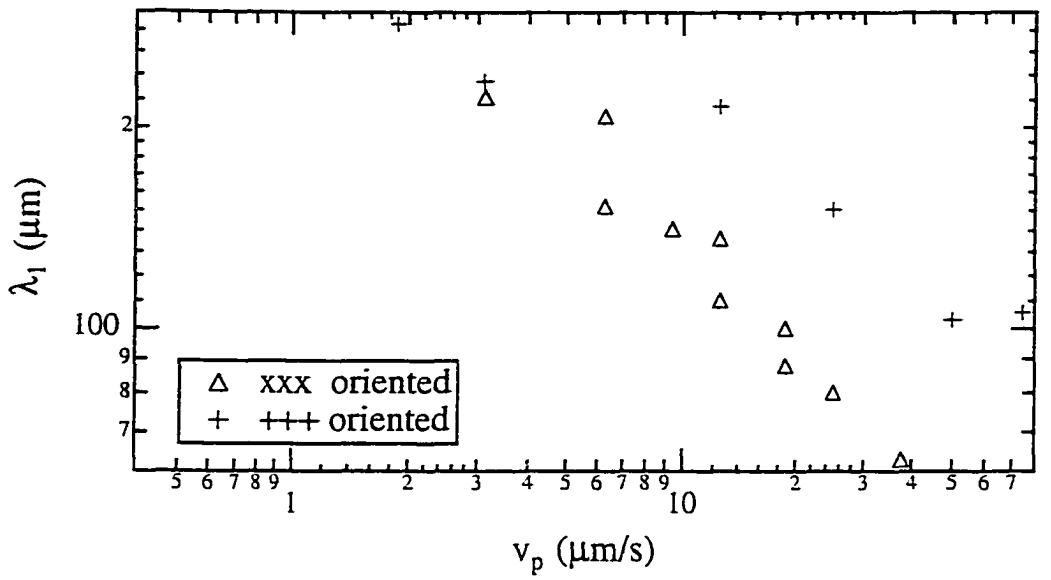

Figure 6.6: Steady state cellular ($< 3-5\mu$m/s) and dendritic spacing as a function of pulling speed V_P. $(+++)$ dendrites show an increase in spacing $(\triangle)$ at the cell-dendrite transition, while $(\times \times \times)$ dendrites $(+)$ show a continuous decrease in spacing.

Sidebranch overgrowth of neighboring cells during the coarsening appears to be a possible mechanism for the observed increase in spacing at the cell to dendrite transition. Sidebranches might have to be included in models of the coarsening dynamics to obtain realistic predictions of dendritic spacings on quasi two-dimensional experiments.

These results also raise the question, whether surface tension anisotropy and sidebranching have to be included in a dendritic array stability analysis.

For three dimensional samples, this result implies that during the coarsening dynamics an array with the smallest interaction between sidebranches, i.e. rows of $(+++)$ dendrites, offset by half a dendritic spacing, should be favored. Figure 6.7 shows a crossection through a three dimensional sample taken from a metallic

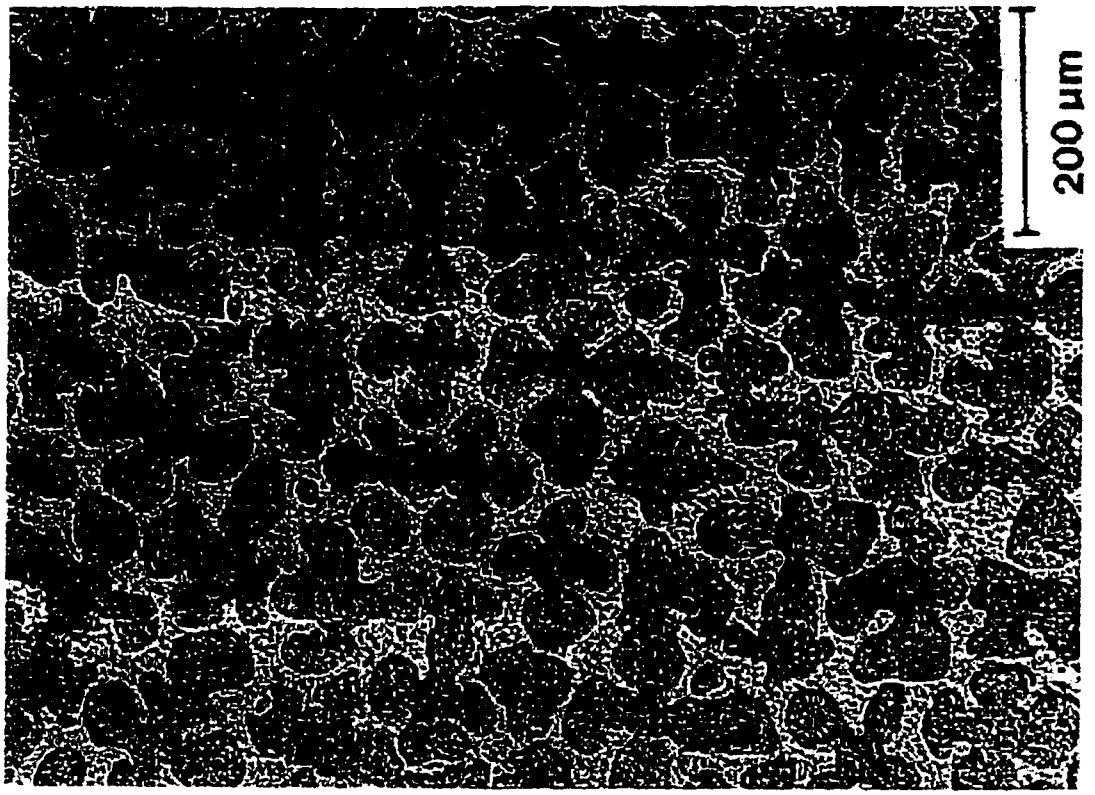

Figure 6.7: Cross section of a dendritic array (from [121]).

alloy (from [121]). Sidebranches are indeed not growing at each other in most cases in this image.

Missing in these experiments is the reversal of the grain orientation back to a $(+++)$ array, to verify beyond comparisons of dendrite tip radii and instability wavelengths, that the sample did not change between the experiments. Therefore the conclusions can only be preliminary, even though they are supported by the simulation results.

Chapter 7

DOUBLET CELLULAR PATTERN

[1]The formation of doublet patterns at the solid-liquid interface of a growing crystal was studied in directional solidification using the new optical perturbation technique described in section 3.3.2. The interface was forced into a range of stable patterns and also into transient unstable patterns in order to analyze the stability range and dynamical evolution of doublet cellular structures both in experiments (on our model alloy SCN/C152) and in numerical simulations carried out by Kopczyński, Rappel and Karma presented in appendix C (utilizing the computationally robust phase-field symmetric model with reformulated asymptotics and vanishing kinetics [120, 85]). The doublet cells were recently predicted from boundary integral calculations and were also found in unperturbed experiments. In

[1]This chapter was adapted from [4]

this study, arrays of doublets with a desired spacing are triggered experimentally through a brief pulse of a spatially periodic perturbation, applied to the planar interface during the planar-cellular transient for a range of spatial periodicities and growth velocities. In turn, numerical simulations allow Kopczyński *et al* to generate doublets for different wavelengths at fixed pulling velocities, identify basic stability limits and perform selection runs initiated by either spatially periodic or random perturbations.

7.1 Introduction

The experiments described in the previous chapters of this thesis and other recent experiments suggest that many observed interface patterns are history dependent and that a given interface pattern can be stable for a range solidification conditions. As outlined in chapter 1, pattern formation experiments therefore have to address separately the questions, how a stable pattern can be created, over what range of solidification conditions it is stable, and which instability mechanisms limit this range.

Interesting patterns for this study are asymmetric doublet states, which were recently found in different pulling speed regimes in addition to the well known symmetric patterns (planar, cellular and dendritic). At intermediate velocities cellular doublets were observed to occur spontaneously by Jamgotchian, Trivedi and Billia (JTB)[20]. At high velocities dendritic doublets were observed in experiments [17] and also found in simulations [18, 19].

In this chapter we study, through phase-field model computer simulations and experiments, the stability and selection of doublet cellular patterns in the pulling speed regime close to that in which doublets were observed by JTB.

JTB observed that doublet cells can occur spontaneously for a small range of velocities between those producing small amplitude cells and deep cells. This symmetry-broken doublet pattern is characterized by alternating deep and shallow grooves and asymmetric cell tip shapes with the tip closer to the shallow groove. A qualitative explanation for the upper and lower stability limits was proposed by JTB. On the low pulling speed side, small amplitude cells tend to have flat tips that are prone to tip splitting, a mechanism that JTB found experimentally as limiting the region of stability. On the high pulling speed side the grooves become deeper so the relative difference in groove depth becomes smaller which makes the cell tips more symmetric. The experiments of JTB measured doublet stability by determining which patterns are selected spontaneously as a function of pulling speed, but could not explore patterns not selected during the evolution from a planar front.

Kopczyński and Rappel [62, 122] carried out boundary integral calculations for the symmetric model of binary alloy directional solidification and examined different possible solutions. In addition to stable symmetric cells, these calculations revealed the existence of steady state branches of doublets and higher order multiplets that bifurcate off the main cellular branch. The qualitative shape of the calculated doublet structure was found to be similar to the doublets observed

by JTB. While the boundary integral calculations indicated the existence of a range of steady state patterns for doublets, they did not determine their stability against perturbations, or show under which conditions doublets can evolve from a planar interface. In addition, the results of the boundary integral calculations suggested that qualitatively different patterns (single cells, doublets, and higher order multiplets) might be stable under the same solidification conditions.

The aim of the present study is to separate the questions of pattern selection and pattern stability in both experiments and numerical simulations by measuring the range of spacings for which stable doublets can exist, and by finding the instability mechanisms limiting that range for a given pulling speed. The possible existence of qualitatively different stable steady-state patterns under the same growth conditions is also explored in experiments and in simulations.

The maximum range of stable doublet patterns and the nature of the limiting instabilities were determined by forcing the interface into stable (or temporarily unstable) patterns for a range of spacings by applying a brief pulse of a spatially periodic perturbation to the planar interface during the planar-cellular transient. The evolution of these forced patterns was then measured both in the simulations and in the experiments.

We find that stable doublets can be triggered for a range of spatial periodicities and growth velocities and that in this range both doublets and single cells can be created as stable patterns under the same steady state growth conditions. For perturbation wavelengths or growth velocities outside of the range in which

stable doublet patterns are obtained, the forced doublet patterns are dynamically unstable and decay. Measuring the response of the interface to spatially periodic perturbations allows us to study the dynamics of doublet formation in detail, to measure the limits of stability, and to observe the dynamics of the decay of unstable doublet structures. Phase-field model simulations and experiments show remarkable qualitative agreement in the dynamic evolution, steady state structure, and in the mechanisms limiting doublet stability for small or large spacings. The agreement indicates that the common features of the experiments and the simulations must play an important role in determining pattern stability and selection.

7.2 Experiments

7.2.1 Experimental Procedure

Before each experiment the oriented single crystal sample is held at rest in the directional solidification apparatus for 20-100 hours to allow equilibration of the concentration profile. All experiments are carried out by starting the VCR and elapsed time counter and switching on the pulling motor after 60 seconds. The shutter for UV illumination is opened during the experiment at specified times for one minute with the row of UV spots aligned along the solid-liquid interface. After one minute the concentration field has adjusted to the thermally induced modulations. The characteristic diffusion length ΔZ_1 is approximately equal the perturbation wavelength and the characteristic length of the concentration spike

ΔZ_2. ($\Delta Z_1 = \sqrt{4Dt} = 329\mu$m, $\Delta Z_2 = D/V_P = 450\mu$m at $V_P = 1\mu$m/s). Due to fast thermal diffusion the relaxation of the temperature profile modulation is neglected in the analysis and only a modulated concentration profile is assumed.

Figure 7.1 shows, from bottom to top, a typical evolution the interface pattern for a sample concentration $C_\infty = 0.30$wt% and a temperature gradient $G =$ 16K/cm, when the motor is started after one minute with a pulling speed $V_P =$ 1.0μm/s ($V_P = 13.4V_C$, V_C is the pulling speed corresponding to the Mullins-Sekerka onset). The times indicated on this figure are taken from the elapsed time counter, so that 1:00 corresponds to the time when the pulling motor is switched on. Initially the interface is planar and shows no sign of an instability (9:30 minutes) since it takes time for the destabilizing solute concentration spike to build up ahead of the interface. At 10:00 minutes the UV illumination shutter is opened for 1 minute and a perturbation with $\lambda_P = 256\mu$m is applied to the solid-liquid interface. The UV intensity adds to the regular illumination intensity and is visible as a row of white spots (10:30 minutes). The modulated interface shape persists after the perturbation is switched off (11:30 minutes). Subsequently, the interface curvature in the grooves gradually gets larger while it gets smaller in the cell tip region (28:00 minutes). Eventually the tip region of each cell splits into three cells (32:00 minutes). The middle cell of each triplet has a smaller amplitude and is overgrown by its neighboring cells. The groove between the two remaining cells becomes deeper than the grooves from the original modulation leading to an asymmetric doublet cellular structure in steady state (40:00 minutes). The final

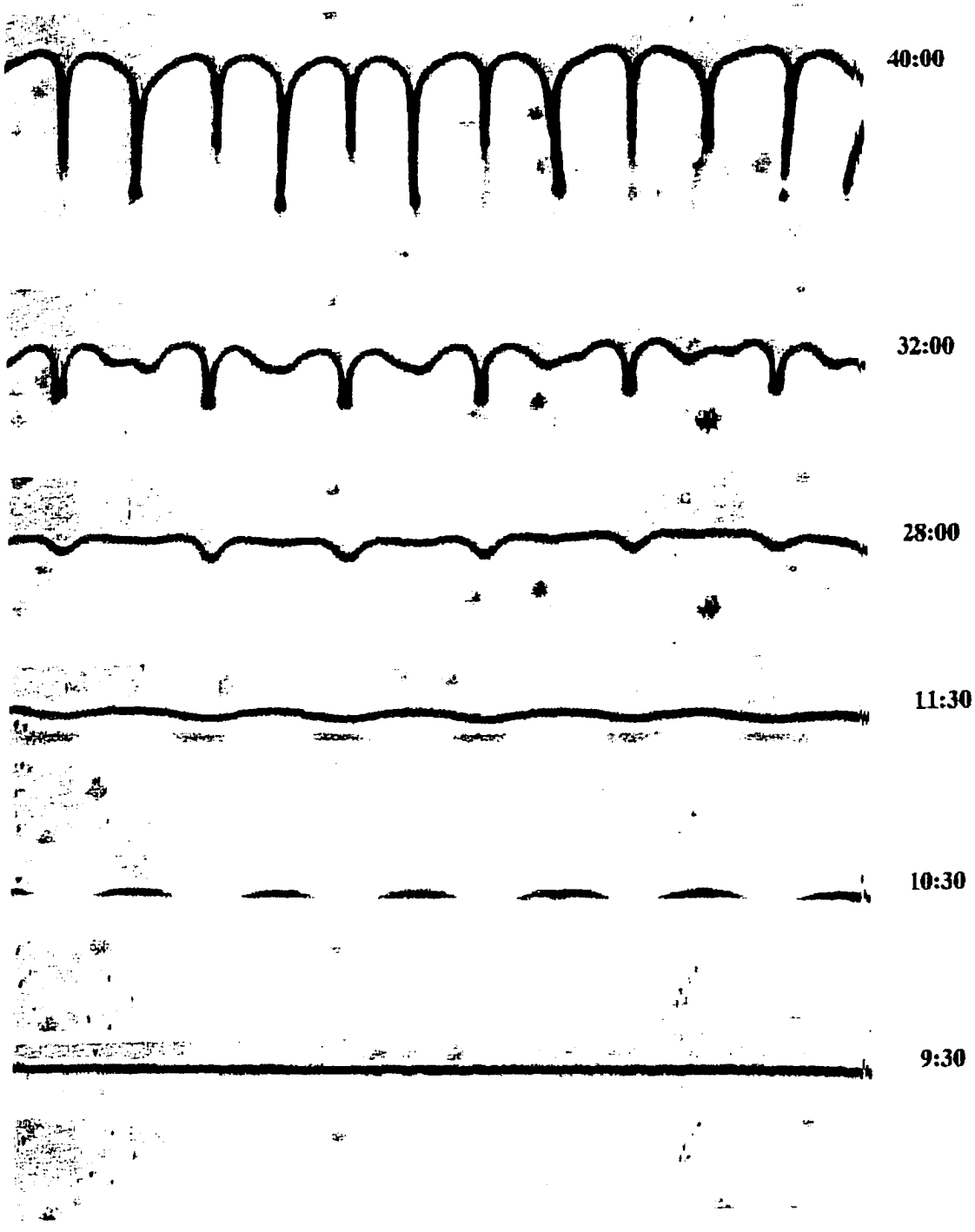

Figure 7.1: Image sequence of the evolution of a forced doublet structure (SCN-C152, $C_\infty = 0.30$wt%, $\lambda_P = 256\mu$m, $V_P = 1.0\mu$m/s ($V_P = 13.4V_C$), $G = 16$K/cm). From bottom to top: 9:30 min. planar transient; 10:30 min. UV perturbation; 11:30, 28:00 and 32:00 min. coarsening; 40:00 min. steady state forced doublets.

steady state spacing of the doublets is determined by the wavelength of the applied perturbation.

7.2.2 Experimental Results

Using the perturbation technique described above to obtain doublets, we first compare this forced doublet evolution to unperturbed experiments, then determine the parameter region where doublets are stable, and finally analyze the limiting instabilities.

A comparison between a perturbed and an unperturbed experiment, both under the same growth conditions (C_∞ = 0.30wt%, V_P = 1.0μm/s (V_P = 10.6V_C) and G = 20.2K/cm), shows the dynamics of forced doublet formation in detail. In experiment 1 the motor is started at $t = 0s$ (when the elapsed time counter reads (60s) and one minute perturbations are applied at t = 240s and t = 840s with $\lambda_P = 286\mu$m ($k_P = 0.022\mu\text{m}^{-1}$).

Figure 7.2 shows (from bottom to top) the interface profile extracted with our image analysis program every 120 seconds starting at t = 720s during the evolution from a sinusoidal modulation and following the steady state doublet cellular array. Figure 7.3 shows the Fourier transform of the interface for wavevectors between 0.01 and 0.1μm^{-1} extracted every 60 seconds starting at t = 960s highlighting the evolution of the doublet structure until a steady state is reached.

As seen in figure 7.2 the perturbation applied at t = 240s leads to an approximately sinusoidal modulation of the planar interface with $\lambda_P = 286\mu$m. The

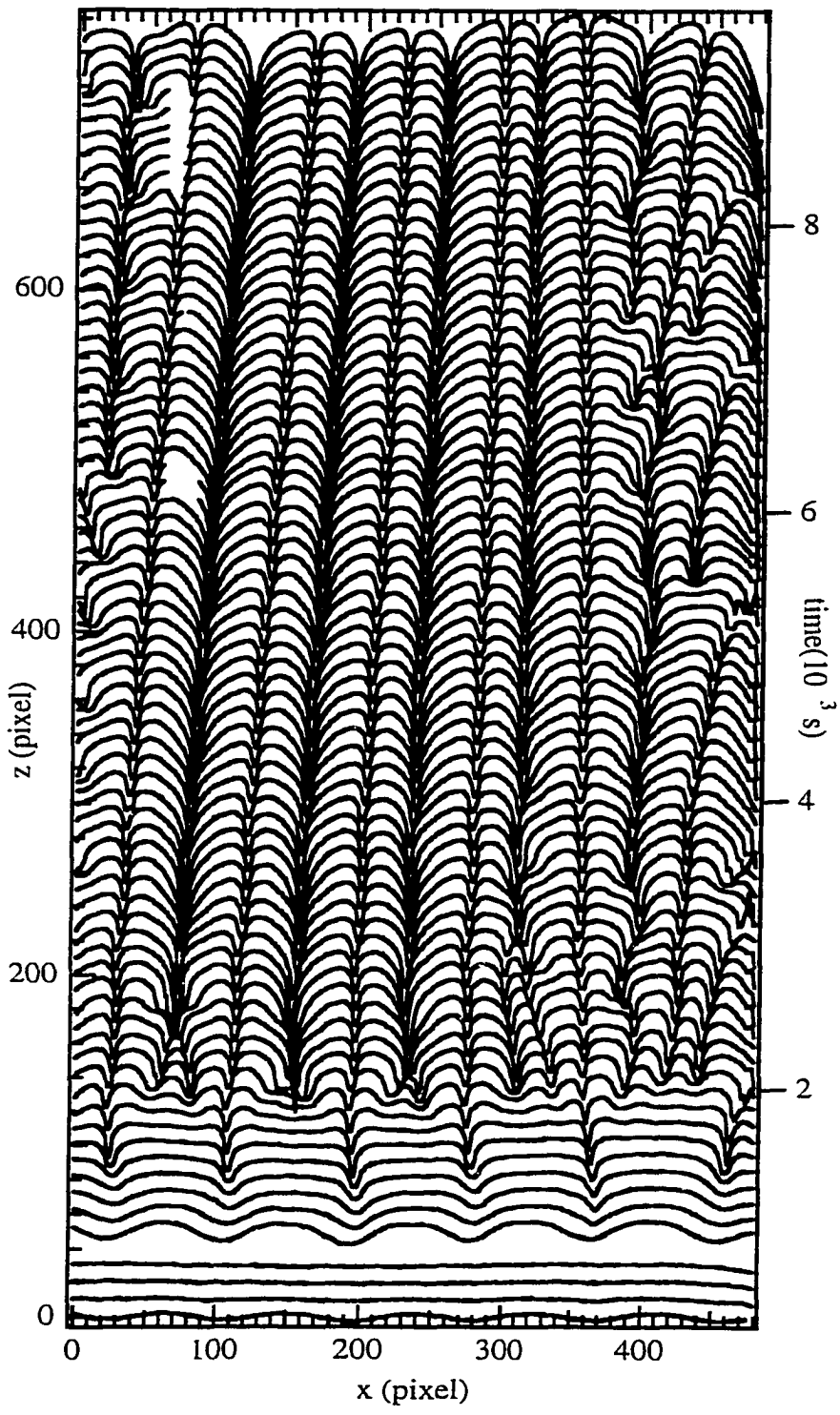

Figure 7.2: Extracted interface shapes for SCN-C152 (C_∞ = 0.30wt%, λ_P = 286μm, V_P = 1.0μm/s (V_P = 10.6V_C), G = 20.2K/cm). Evolution to doublets from bottom to top: Perturbation at 240s decays, perturbation at 840s evolves into doublets. Initial grooves become shallow grooves of doublets. (x-axis: 1pixel = 3.29μm; z-axis: 1pixel = 3.17μm)

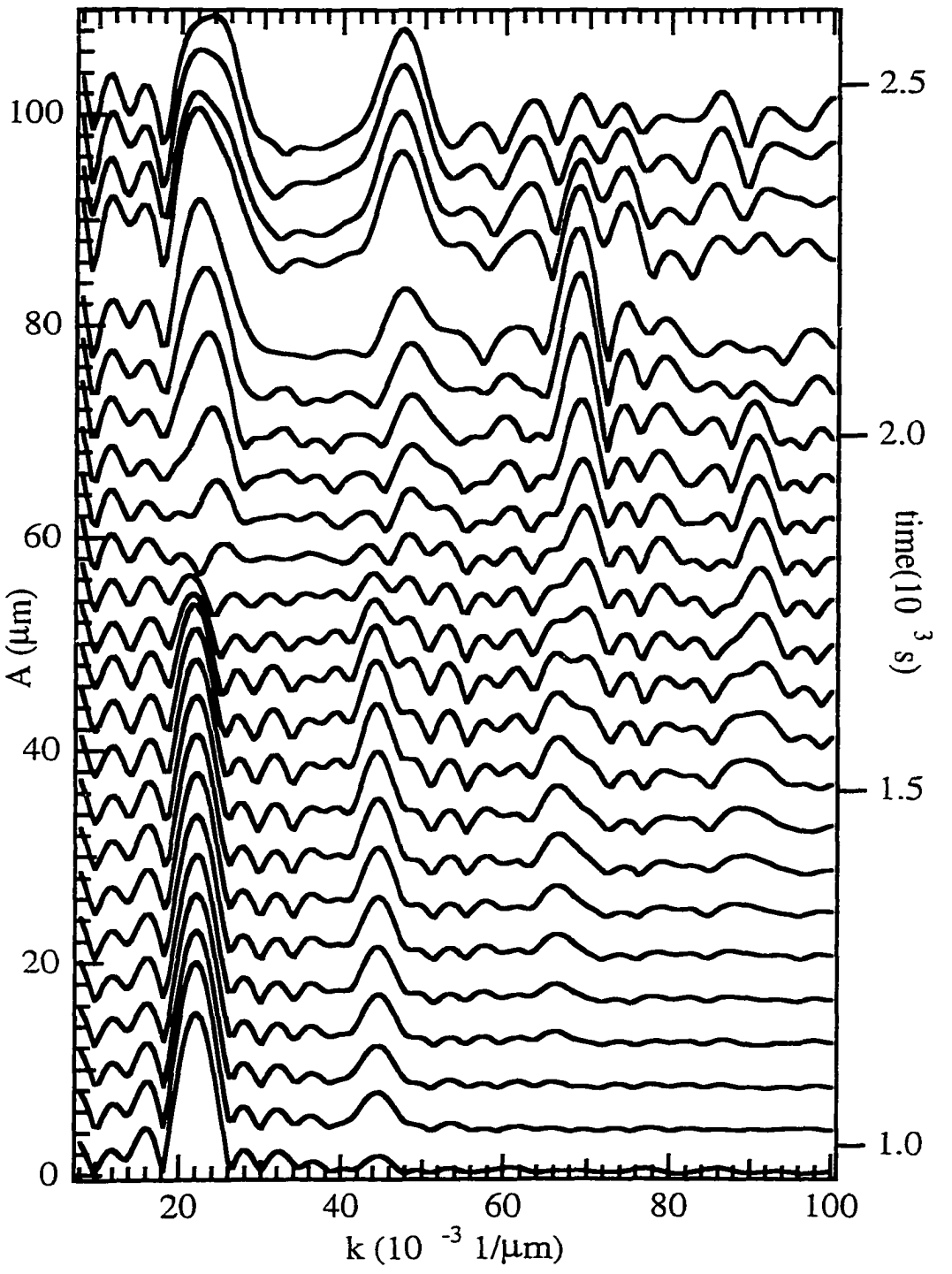

Figure 7.3: Fourier transform of the interface profiles during doublet formation (same experiment as in fig. 7.2: $C_\infty = 0.30$wt%, $\lambda_P = 286\mu$m ($k_P = 0.022\mu$m^{-1}), $V_P = 1.0\mu$m/s ($V_P = 10.6V_C$), $G = 20.2$K/cm). Doublets evolve through growth of second, third and fourth harmonics of the applied perturbation wavelength.

amplitude of the interface modulation decays exponentially after the perturbation is switched off, indicating that the planar interface is still stable. The reason is that the destabilizing concentration spike ahead of the solid-liquid interface takes time to build up so that the planar interface remains stable against perturbations for some time after crystal growth is started, as described in chapter 4.3. The perturbation applied at $t = 840$s again modulates the planar interface profile with $\lambda_P = 286\mu$m. The amplitude of the modulation initially decreases again but now goes through a minimum and starts to grow. This indicates that the interface is stable against perturbations of wavelength $\lambda_P = 286\mu$m at $t = 840$s when the perturbation is applied, but becomes unstable before the modulation amplitude has decayed completely. During the decrease of the modulation amplitude with wavelength $\lambda_P = 286\mu$m the interface changes its shape as the region between grooves flattens ($t = 900$s until $t = 1500$s in fig. 7.2). As a result the Fourier amplitudes of the harmonics of $\lambda_P = 286\mu$m grow visibly ($t = 900$s until $t = 1500$s in fig. 7.3). Eventually the flat region between grooves goes unstable at $\lambda_P/3 = 95.3\mu$m in most regions ($t = 1800$s in fig. 7.2) as the amplitude of the third harmonic starts to increase rapidly, reducing the other Fourier components, especially $\lambda_P = 286\mu$m (fig. 7.3). The middle cell of each triplet falls back quickly during coarsening and a doublet pattern is established after ~ 3000s. The initial modulation wavelength determines the doublet spacings, and the grooves of the initial modulation evolve into the small grooves of the steady state doublets. This asymmetric doublet pattern exhibits two characteristic peaks in the Fourier transform and remains stable

for the entire experimental run of more than 5 hours. Since the width of the sample is not much larger than the extracted interface portion, perturbations caused by the finite sample width can become visible on either side of the analyzed interface section. In this case the influences of the sample wall are visible in figure 7.2 for $x > 400$pixel and lead to a slow sideways drift of the stable doublet pattern and some narrowing of the doublets without destroying the pattern.

The evolution of the unperturbed interface is observed in experiment 2 under conditions otherwise identical to experiment 1. The interface shape, extracted every 120s starting at $t = 720$s is shown in figure 7.4. At $t = 840$s (when the UV perturbation was applied in experiment 1) the unperturbed interface is still planar. At $t \approx 2000$s an initial spontaneous instability becomes visible with $\lambda_U \approx 91\mu$m, approximately 1/3 of $\lambda_P = 286\mu$m in experiment 1. The evolution in experiment 1 from λ_P to $\lambda_P/3$ thus involves the harmonic of the applied perturbation wavelength closest to the 'natural' initial instability wavelength $\lambda_U \approx 91\mu$m in agreement with the experiments described in section 4.3.

In this unperturbed experiment the cellular pattern does not settle down but continuously evolves through tip splitting and cell overgrowth eventually showing signs of a rather inhomogeneous and slowly developing doublet structure at $t =$ 6000s. The evolution is slower than observed by JTB, possibly because no grain boundaries (which can initiate doublet formation) are present in any of the samples we used.

These experiments show that stable forced doublets (experiment 1) of a se-

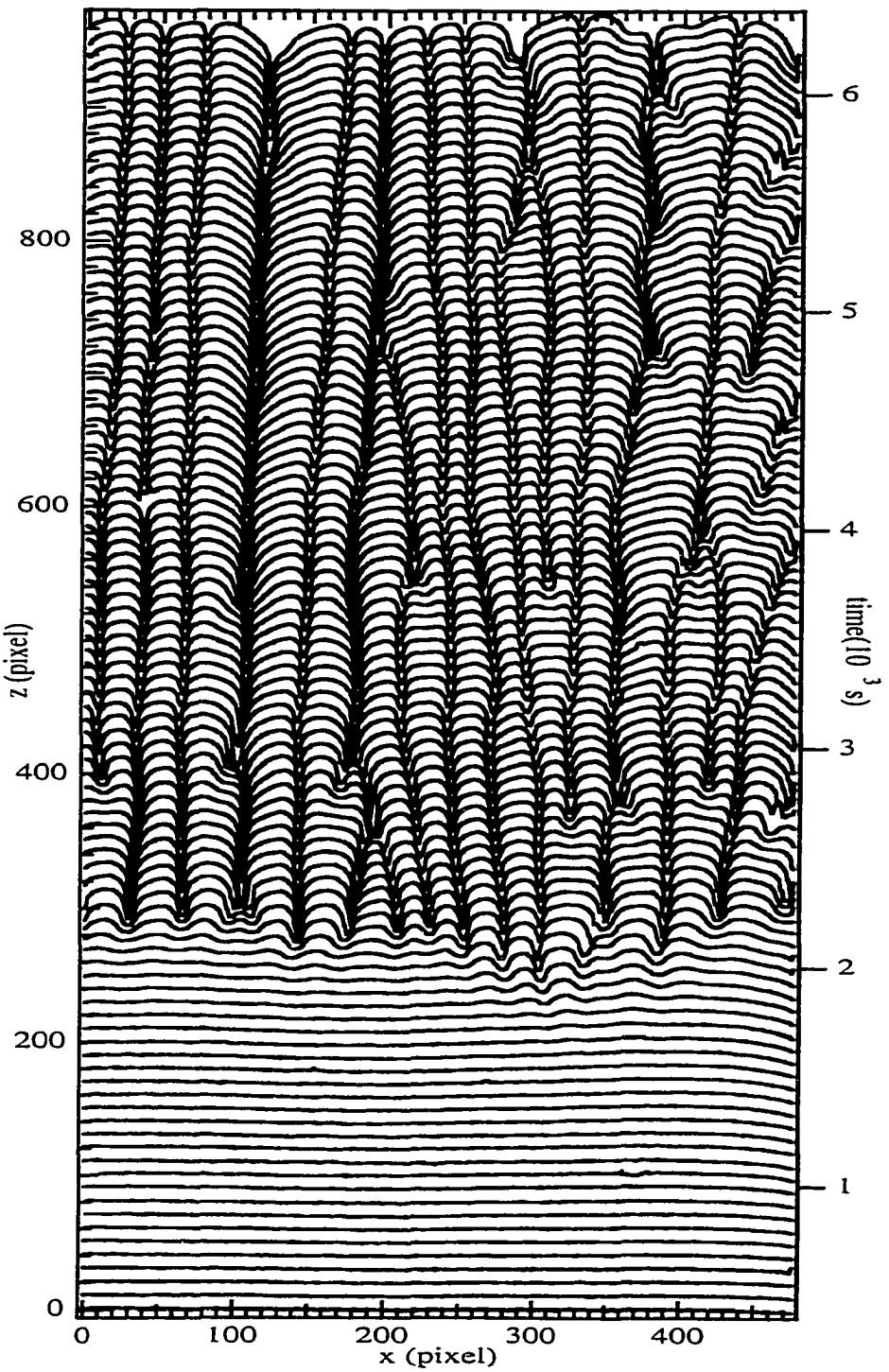

Figure 7.4: Extracted interface structure for SCN-C152 (C_∞ = 0.30wt%, V_P = 1.0μm/s ($V_P = 10.6V_C$), G = 20.2K/cm). Unperturbed 'standard' experiment. Interface extracted every 120s starting at t = 720s. (x-axis: 1pixel = 3.29μm; z-axis: 1pixel = 3.17μm)

lected wavelength can be created under growth conditions for which there is a 'weak' tendency to create doublets spontaneously (experiment 2). While spontaneous doublets may occur gradually in unperturbed experiments after some time, they can be induced directly through a spatially periodic perturbation of suitable wavelength (which sets the doublet spacing), applied before the planar interface goes unstable. Fourier analysis of the pattern shows significant amplitudes only for harmonics of the perturbation wavelength during the formation of the doublet pattern.

To estimate the parameter region where forced doublets are stable we carried out a series of four experiments each at two temperature gradients, all with $C_\infty = 0.30$wt% at $V_P = 0.8\mu$m/s. In three experiments different perturbation wavelengths ($\lambda_P = 246\mu$m, $\lambda_P = 282\mu$m and $\lambda_P = 318\mu$m) were applied and one experiment was carried out without perturbation.

At $G = 20$K/cm ($V_P = 8.6V_C$) in the unperturbed experiment, parts of the interface slowly evolve into doublets which shows a 'weak' tendency towards a stable doublet state. For $\lambda_P = 246\mu$m and 282μm stable doublets develop while for $\lambda_P = 318\mu$m the interface shows doublets only initially which decay after $t \approx 9000$s evolving into an unstable pattern with no indication of settling down.

The unperturbed experiment at $G = 16$K/cm ($V_P = 10.7V_C$, a lower G is equivalent to higher speed) shows no settling down of the pattern (chaotic pattern) resembling the pattern evolution found by JTB for a speed above the range where doublets are observed (see fig. 12 in JTB [20]). With $G = 16$K/cm only the

perturbation with $\lambda_P = 282\mu$m produces a strong doublet state; the perturbation with $\lambda_P = 246\mu$m produces a weak doublet state showing almost single cells, and for $\lambda_P = 318\mu$m no settling down of the pattern is observed. The range of stable doublet spacings thus appears larger for growth parameters where some doublets are observed in an unperturbed experiment. Outside of that parameter region creation of doublets is still possible, but is limited to a small range of stable doublet spacings. The results are summarized in table 7.1.

Perturbation	$G = 20$K/cm	$G = 16$K/cm
unperturbed	some spontaneous doublets	chaotic pattern
$\lambda_P = 246\mu$m	doublets	weak doublets
$\lambda_P = 282\mu$m	doublets	doublets
$\lambda_P = 318\mu$m	slowly decaying doublets	chaotic pattern

Table 7.1: Observed interface pattern for unperturbed and perturbed interfaces with three different perturbation wavelengths at two temperature gradients. ($C_\infty = 0.30$wt%, $V_P = 0.8\mu$m/s ($V_P = 9.0V_C$))

The mechanisms limiting the range of stable doublet spacings are illustrated in figures 7.5 and 7.6, which are taken from a set of experiments with $C_\infty = 0.20$wt%, $G = 15.8$K/cm and $V_P = 1.0\mu$m/s.

The mechanism limiting doublet pattern stability in the large wavelength limit is shown in figure 7.5. After a perturbation with $\lambda_P = 308\mu$m is applied at $t =$ 1200s the interface initially evolves into a doublet pattern. This pattern exhibits a 'breathing' instability from the start which is visible as an oscillation of the deeper

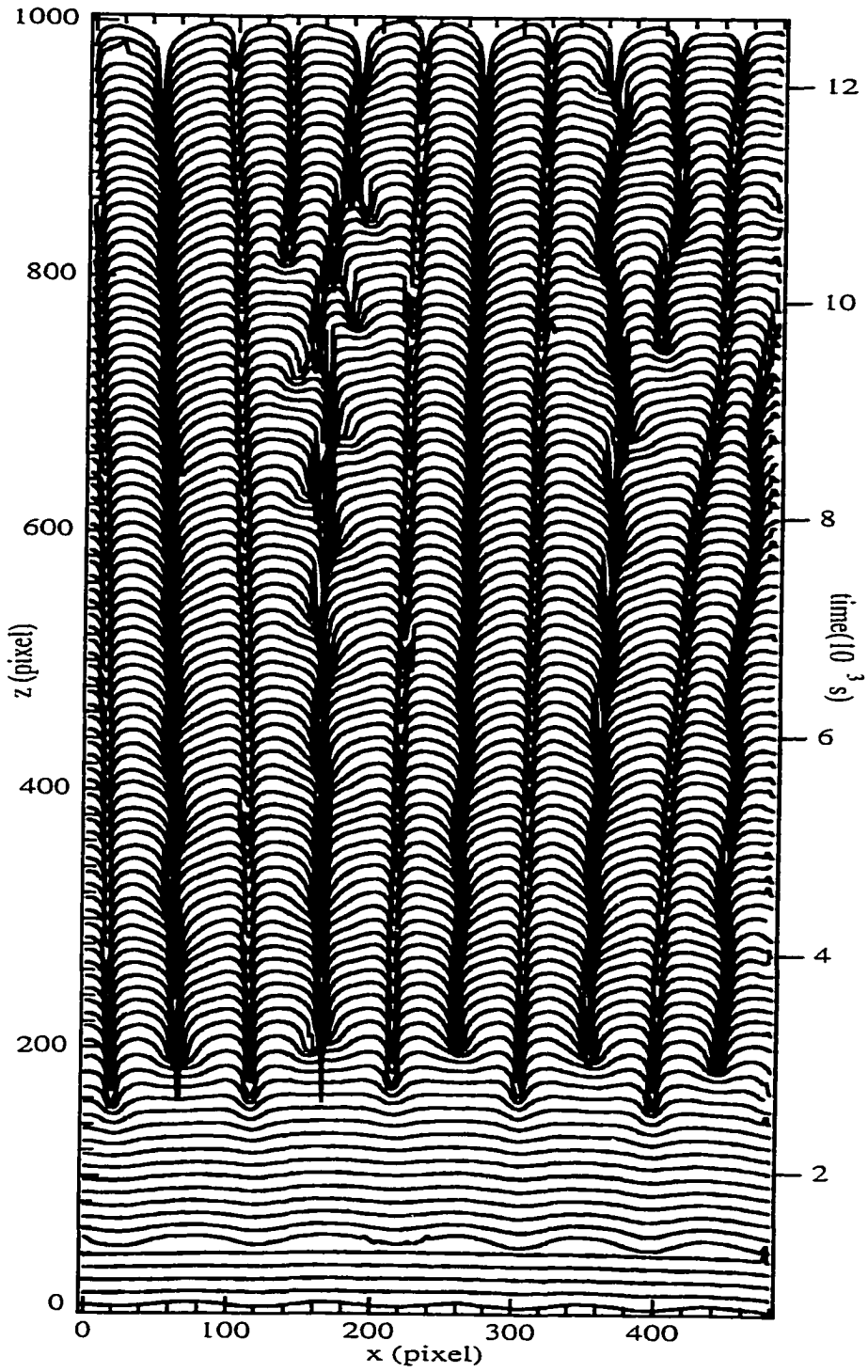

Figure 7.5: Breathing instability of a doublet structure in the large perturbation wavelength limit for SCN-C152 (C_∞ = 0.22wt%, λ_P = 308μm, V_P = 1.0μm/s (V_P = 9.9V_C), G = 15.8K/cm). Interface extracted every 120s starting from t = 720s. (x-axis: 1pixel = 3.29μm; z-axis: 1pixel = 3.17μm)

(darker) grooves. Eventually one of the oscillations leads to the birth of a new cell at $t = 10000$s creating a triplet.

Figure 7.6 shows the evolution of the pattern in the small perturbation wavelength limit, when a perturbation with $\lambda_P = 236\mu$m is applied at $t = 1200$s. Initially a doublet state with comparatively small asymmetry develops (see figure 7.7a), but at $t \approx 6000$s an oscillatory instability becomes observable which leads to broadening of every other cell (see figure 7.7b) and eventually to the falling back of one of the cells. The pattern does not appear to stabilize, even after 12000s. The Fourier transforms of the interface profiles, shown in figure 7.8, indicate that a new dominant mode develops with a wavelength smaller than half the doublet spacing.

While the oscillatory motion is limited to deep grooves in the large wavelength limit, the positions of all grooves oscillate in the small wavelength limit. This oscillatory instability in the limit of small doublet spacings appears to be similar to recent experimental observations [84] of oscillatory instabilities for cell spacings too large for stable single cells.

When the perturbation wavelength is even smaller, stable single cells can be obtained. Figure 7.9 (taken from another set of experiments with $C_\infty = 0.22$wt%, $V_P = 1.0\mu$m/s ($V_P = 13.9V_C$), $G = 11.3$K/cm) shows two experiments under the same growth conditions but with different perturbation wavelengths (in 7.9(a) $\lambda_P = 246\mu$m; in 7.9(b) $\lambda_P = 318\mu$m) applied at $t = 1800$s before the planar interface goes unstable. Figure 7.9(a) shows the evolution of the interface towards

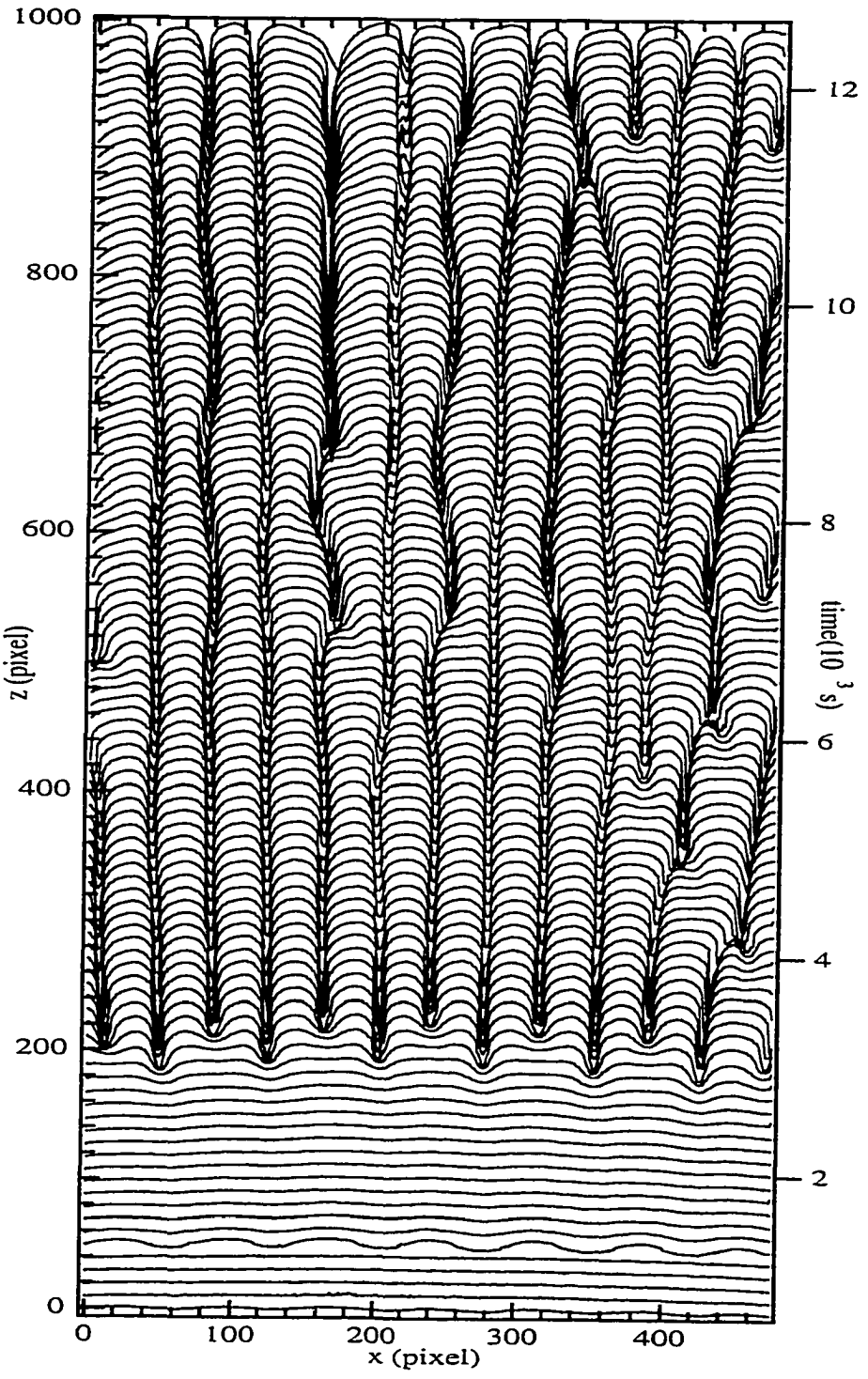

Figure 7.6: Oscillatory instability of a doublet structure in the small perturbation wavelength limit for SCN-C152 (C_∞ = 0.22wt%, λ_P = 236μm, V_P = 1.0μm/s (V_P = 9.9V_C), G = 15.8K/cm). Interface extracted every 120s starting from t = 720s. (x-axis: 1pixel = 3.29μm; z-axis: 1pixel = 3.17μm)

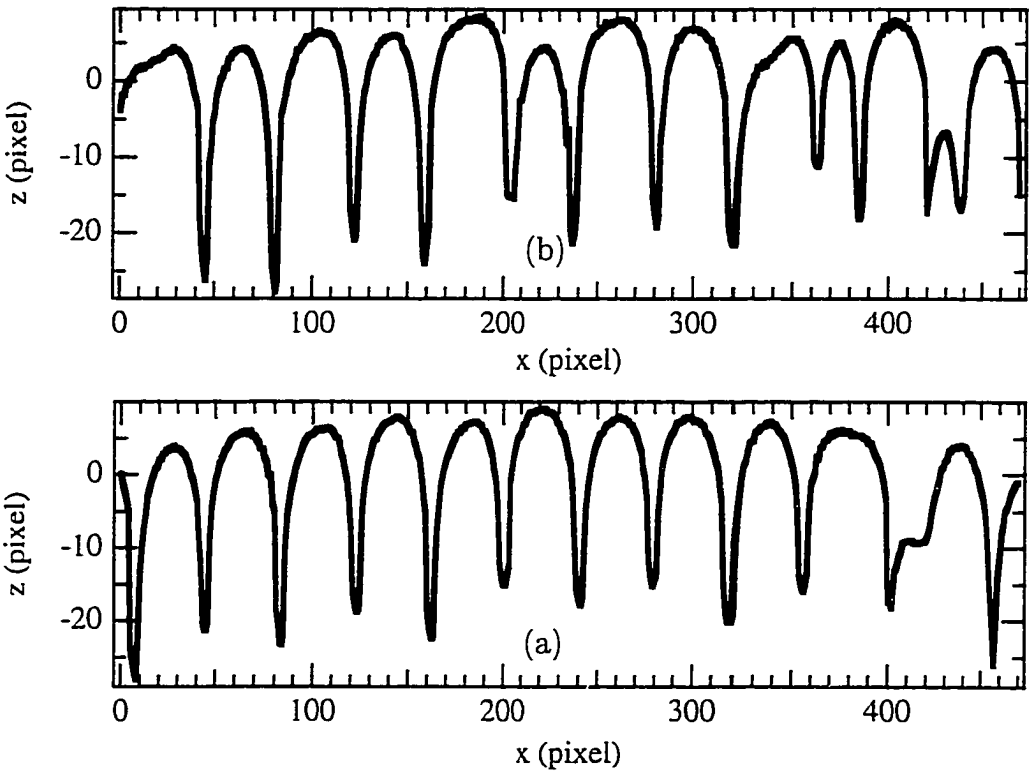

Figure 7.7: Interface profiles before and during an oscillatory instability of a doublet structure in the small perturbation wavelength limit for SCN-C152 (C_∞ = 0.22wt%, λ_P = 236μm, V_P = 1.0μm/s (V_P = 9.9V_C), G = 15.8K/cm). (a) Doublet cells at t = 4980s and (b) oscillatory instability at t = 6300s. (x-axis: 1pixel = 3.29μm; z-axis: 1pixel = 3.17μm)

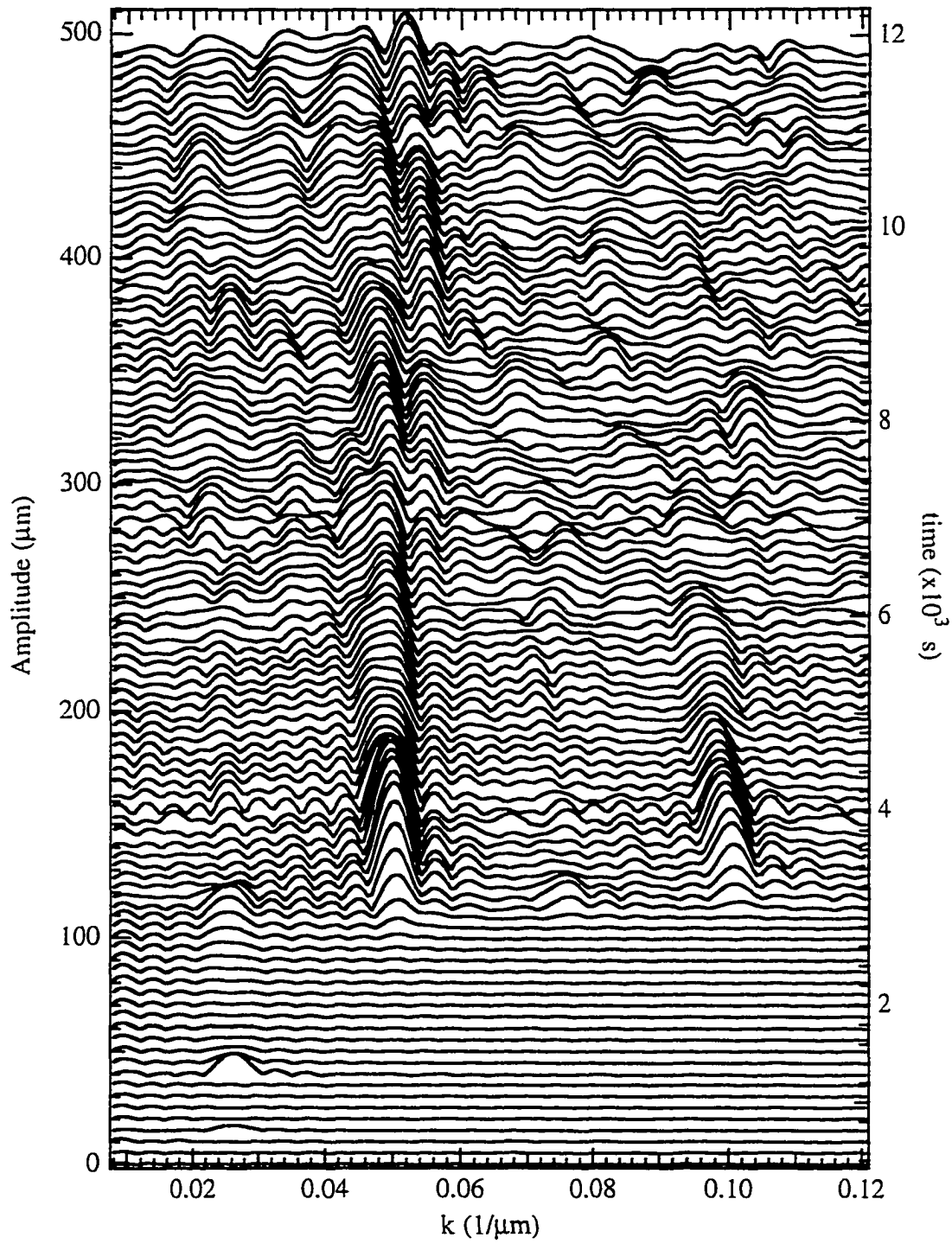

Figure 7.8: Fourier transform of the interface profiles of figure 7.7

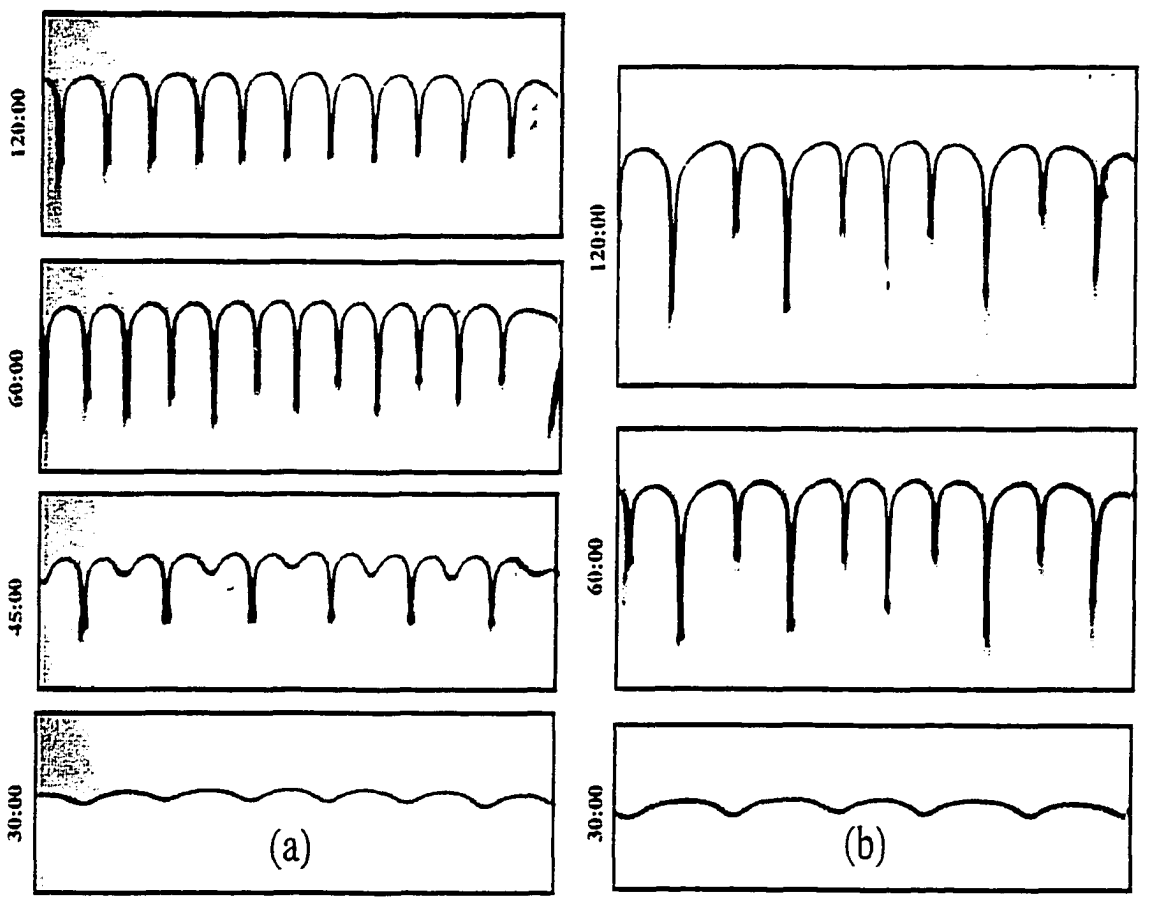

Figure 7.9: Image sequence of the evolution to steady state doublets and single cells under the same steady state growth conditions (SCN-C152: $C_\infty = 0.22$wt%, $V_P = 1.0\mu$m/s ($V_P = 13.9V_C$), $G = 11.3$K/cm). (a) Small wavelength perturbation $\lambda_P = 246\mu$m: Transient doublets and steady state single cells. (b) Large wavelength perturbation $\lambda_P = 318\mu$m: Steady state doublets.

steady state single cells when a small wavelength perturbation ($\lambda_P = 246\mu$m) is applied. The tips of the initial cellular modulation go unstable at $\lambda_P/2$ (45:00 min). A transient doublet structure is observed (60:00 min). The doublets decay into a steady state single cell structure (120:00 min) with uniform wavelength. (This evolution is qualitatively very similar to results of numerical simulations carried out close to V_C (Figure 3 of [92]).) Figure 7.9(b) shows the evolution of the interface towards steady state doublets when a large wavelength perturbation ($\lambda_P = 318\mu$m) is applied. Now the doublet structure that is again observed at 60:00 min remains stable in steady state (120:00 min). This experiment thus shows that both singlet and doublet patterns can be stable under identical growth conditions as suggested by the boundary integral calculations.

7.3 Discussion

The dynamical evolution of doublets and the instability mechanisms found experimentally as discussed in the preceding section, are in good qualitative agreement with computer simulations using an improved phase-field model. The simulation method and the numerical results are important for the conclusions and are presented in appendix C. The text of appendix C was written by Kopczyński, Rappel and Karma as part of our collaborative publication [4].

Both experiments and simulations show that a brief periodic perturbation with a well-defined wavelength, applied before the planar interface instability has set in, can result in an interface consisting of stable doublets. The perturbation brings the

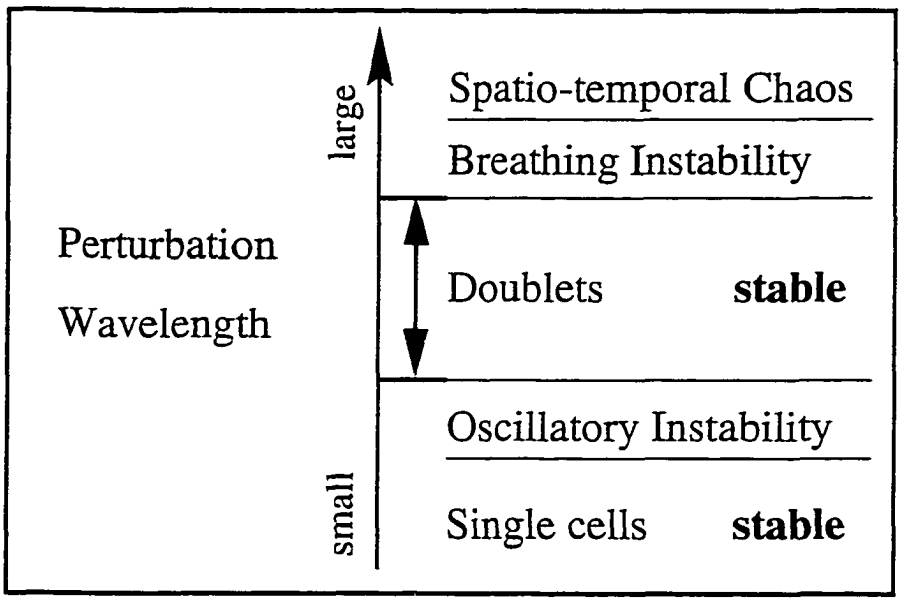

Figure 7.10: Patterns observed in experiments and simulations as a function of the perturbation wavelength.

system into its steady doublet state rapidly and selects a uniform doublet spacing. Experiments and simulations further indicate that the doublet pattern is stable for a range of doublet spacings and growth speeds. The experiments indicate that the range of spacings is largest in the region where some doublets appear transiently without a perturbation.

Outside of the range of stable doublet spacings, different transient and stable patterns are observed. Fig.7.10 summarizes the patterns observed as a function of the perturbation wavelength. Transient doublets are observed in experiments and the simulations adjacent to the range of stable doublets. In the long wavelength limit a breathing instability is observed (which eventually leads to the 'birth' of new cells in some experiments and simulations). In the small wavelength limit an oscillatory instability is observed which eventually leads to the overgrowth of

some cells in both the experiments and the simulations. The range of perturbation wavelengths where transient doublets are observed is narrow. For smaller wavelengths transient doublets are only observed briefly and the steady state interface consists of an array of regular cells. For wavelengths far larger than the stable doublet range the interface displays spatio-temporal chaos from the start without transient doublets.

In the absence of a perturbation, the system never reaches stable uniform rows of doublets in experiment or simulations and displays only inclusions of transient doublets and other multiplet states. This indicates that the stable doublet state is not accessible in the noise initiated evolution from a planar interface, but can be accessed in experiments and the simulations through a spatially periodic perturbation of the planar interface during the initial transient. The 'natural' initial instability wavelength of the planar interface (observed in unperturbed experiments) still influences the dynamics of doublet formation, but the perturbation wavelength sets the steady state doublet spacing.

Triplets or higher order multiplets, found in boundary integral calculations, were only transiently present in experiments and simulations and are either dynamically unstable, have a small stability region, or can not be triggered by sinusoidal modulations.

The dynamics of decay of transient doublets, observed in experiments and simulations just outside the range of stable doublets, indicate that doublets are most unstable against a perturbation wavelength of the doublet spacing (twice of

the symmetric cell spacing).

In contrast to earlier phase field models, this form of the phase-field model gives quantitatively accurate results (as verified in [120, 85]). Unfortunately, at this point they can not be compared quantitatively to the experimental results, since the simulations employ the symmetric model of binary alloy solidification with a constant miscibility gap while the experimental system is best described by the one-sided model with constant segregation coefficient. In addition, in the simulations the ratio of capillary length to thermal length (d_0/l_T) is three orders of magnitude bigger than in the experiments. Despite the differences, for all steady state patterns and dynamical instabilities, the phase-field simulations and the experiments show excellent agreement. This indicates that the ratio between V_P and V_C and the surface tension anisotropy, which are comparable in experiments and simulations, are important parameters for pattern selection and pattern stability.

The new pattern selection method presented in this chapter, based on applying a brief spatially periodic perturbation to the solid-liquid interface of a solidifying sample, alters the natural selection process, provides a direct experimental way of accessing patterns not selected during the evolution from an unperturbed planar interface, and permits exploring the stability of cellular patterns over a large range of spacings.

Chapter 8

EFFECT OF THE THIRD DIMENSION

While most theoretical analysis discussed in chapter 2 assumes a two dimensional sample[1], experiments are always carried out on three dimensional samples. In bulk samples, the third dimension adds patterns with a more complex morphology as the primary spacing between cells or dendrites alone is not sufficient to characterize the pattern. Above the critical pulling speed, small pockets of solute rich environment develop. At intermediate speeds long grooves develop between the pockets forming irregular cells. At higher speeds a regular array of hexagonal cells forms, independent of the crystalline orientation [119].

In thin samples, the contact angle between the solid-liquid interface and the

[1]with the exception of the Warren-Langer dendritic stability analysis, where the dendrite tips are assumed to be three dimensional

glass container introduces deviations from a planar interface shape in the third dimension. This effect of the third dimension is analyzed in new experiments as described below.

8.1 The 3D Effect in quasi-2D Experiments

The contact angle between the solid-liquid interface and the glass capillary introduces a small modulation of the planar interface shape close to the wall. The bending at the wall introduces very short wavelength modulations of the planar front, but in addition also a long wavelength component given by the sample dimensions. Since the amplitude of thermal noise has to be amplified by approximately ten orders of magnitude to become observable [39] as an initial instability of a planar front, the influence of the meniscus on the observed instability has to be examined carefully. Not too close to the critical pulling speed V_C, the Warren-Langer linear stability analysis of the planar interface [39] (see section 2.2.2) shows that both the instability wavelength and the instability time are insensitive to changes of the amplitude of initial modulations by orders of magnitude (see figure 4.10). In addition, in the deep cellular or dendritic regime the cell or dendrite spacings are usually chosen to be equal to or smaller than the sample thickness. The initial instability wavelength is smaller than the sample thickness in these cases, so that both the meniscus along the x-axis and along the y-axis have a comparable effect.

Near the critical pulling speed V_C however, the instability evolves slowly and different initial amplitudes can become significant. In addition, the modulation

created by the contact angles with the glass across the thin dimension of the sample is now often comparable in wavelength to the mode that goes unstable first. Therefore the instability may first become observable along the (thin) y-axis. This instability in turn lowers the solute concentration at the front of the interface and can prevent the instability from occurring along the x-axis as well. This 3D - instability can therefore not be detected in most experiments.

A variation of the critical pulling speed and instability wavelength with sample thickness was observed experimentally be deCheveigne *et al* [113] and explained theoretically by Caroli *et al* [123]. The 3D instability, i.e. the development of one cell *only* in the thin dimension of a sample, was recently observed for the first time in metallic alloys using X-ray tomography [124].

While the contact angle with the sample container is responsible for these effects, the confinement of the concentration field also influences the final steady state pattern. The cellular spacing was found to be thickness dependent [125] and the cell-dendrite transition was also observed to depend on the sample thickness [125].

8.2 New Experiments on the 3D Instability

The instability along the (thin) y-axis can be made visible in our SCN/C152 samples through simultaneous illumination of the sample with visible and UV light. The regular light shows the front point of the solid-liquid interface and the UV light visualizes the regions of high concentration. Due to a small segregation coefficient of 0.05 the end of the high concentration region indicates the back of the

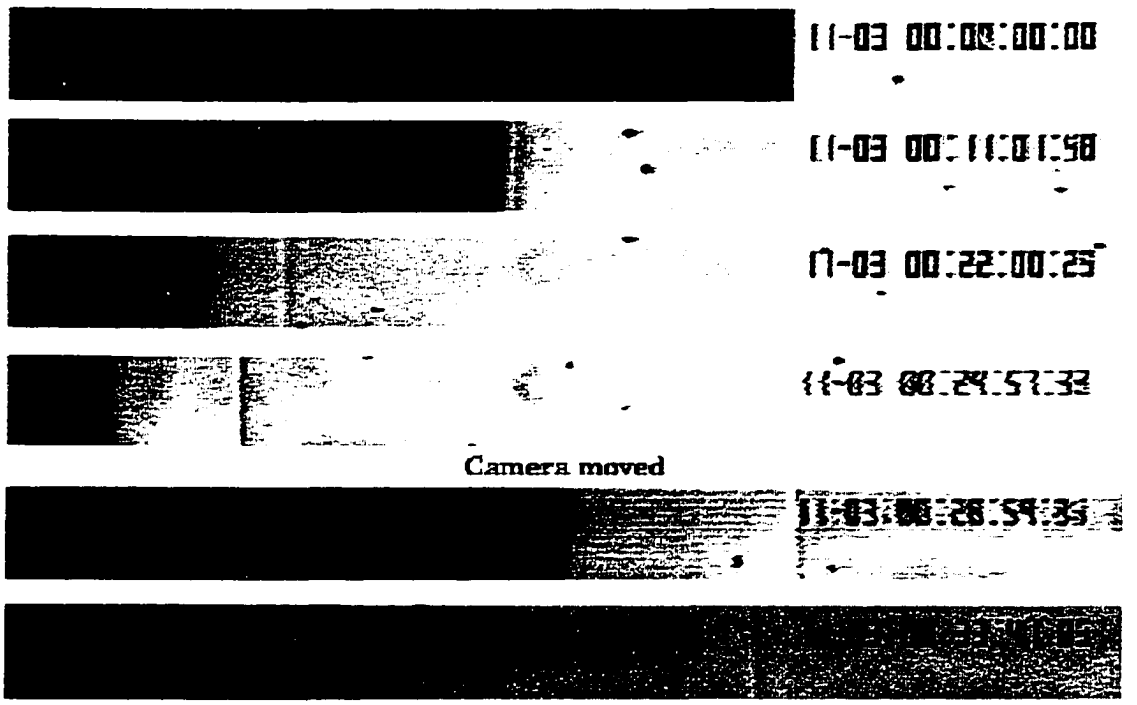

Figure 8.1: Images of a planar interface instability occurring *only* along the (short) y-axis. Observation through simultaneous UV and regular illumination. The UV illumination visualizes the concentration field, the regular illumination visualizes the front of the solid-liquid interface. The instability occurs between 11 min and 22 min.

solid-liquid interface.

Figure 8.1 shows a segment of a planar interface under simultaneous UV and regular illumination after the motor is started. After 11 minutes a crossover from dark to light and a thin line slightly ahead indicates that the solid - liquid interface is slightly curved. Between 11 minutes and 22 minutes an instability occurs along the y-axis and solute invades further behind the planar front. No instability is observed along the x-axis.

Figure 8.2 shows a plot of the extracted position of both the planar front and the point up to which solute invades, taken from another experiment. The onset

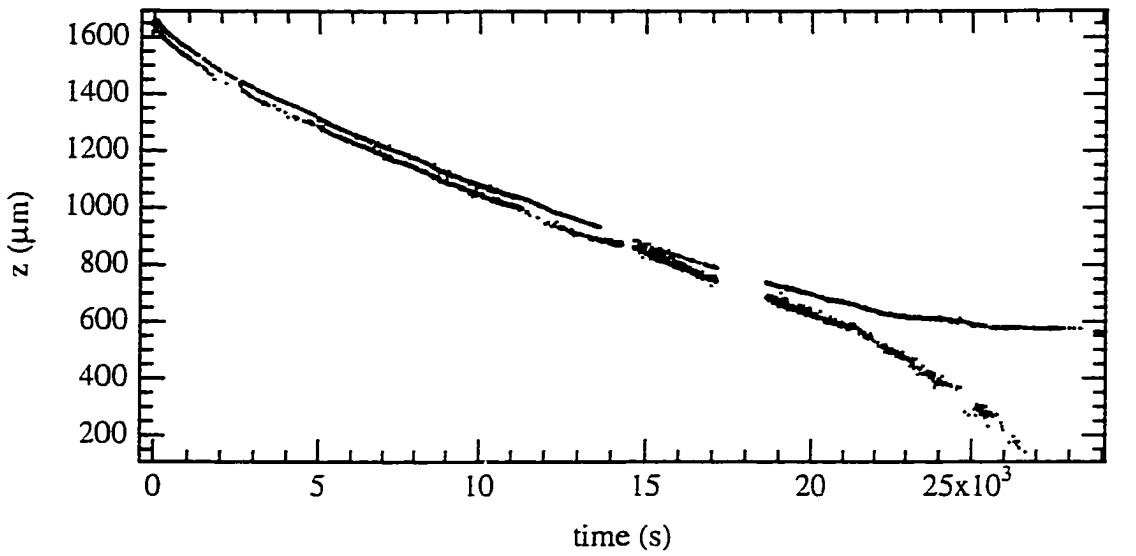

Figure 8.2: Measurement of the onset of curving along the y-axis of a planar interface. Both the front and the back of the interface are shown, recognized in images through large changes in greyscale. The onset of an instability at $t \approx 20000$s is clearly visibly.

of an instability is clearly observable at $\approx$ 20000s while no instability occurs along the x-axis (not shown).

These measurements demonstrate that an instability along the y-axis alone can occur at low pulling speeds. Measurements of the solute concentration profile through scanning (shown in figure 4.2) had also indicated the onset of an instability along the y-axis.

Solute trapping is a possible explanation for these observations, but preliminary calculations showed that the time, when the instability occurs in experiments, lies between t_i and t_0 of the Warren - Langer linear stability analysis, indicating a morphological instability that starts from a comparatively large amplitude.

Appendix A

Programs for Pattern Recognition

Many image analysis program packages, e.g. NIH image, include pattern recognition algorithms. However, these algorithms detect interface shapes only with one pixel accuracy or less and are not optimized for recognizing specific features or locations of known shapes (i.e. cells or dendrites) with the highest possible accuracy.

Most image analysis was therefore done using our own program **get5.3** (get5.3d for dendrites). The program and its subroutines were written in C under MPW Shell 3.0 and run on a Macintosh IIci with a Data Translation 2255 Quickcapture frame grabber board. It builds on programs developed by Lloyd Williams, Martin Muschol and others in this laboratory and on a Fourier transform subroutine by J.M.A. Figueiredo.

In short, get5.3 follows the steps outlined in section 3.5.1 to extract interface features from video images. First, the program extracts selected portions from

video or camera images and writes the image regions (in MCID format) as separate files into the folder *image*. Then, for each image, the program saves all possible interface points[1] in the folder *int-extr*, selects the most likely interface shape from all possible interface points through pattern recognition algorithms, saves the shapes in the folder *int*, and saves the Fourier transforms of the line shapes (or the tip positions of dendrite tips for get5.3d) in the folder *fourier*.

The program runs as a tool within MPW Shell 3.0 and is started with the command:

get5.3 datazip:exp97 *-e 1 -f 1*

All files and folders used by the program have to be in the main folder (here: datazip:exp97) on the Desktop. Options *can* be appended to the command as shown here in italic. The options are explained below.

An input file (*getinterface.in*) contains formatted information about the location and width of the extracted image, the thresholding mechanism (TM), the threshold amplitude (TA) and the time between scans.[2]

The thresholding method TM = 0 is used to detect dark interfaces on a lighter background (as in figure 1.3), while selection of the thresholding method TM = 1 allows detection of interfaces marked by transitions from bright to dark (as in figure 4.1). In order to find the interface, the program scans each line of the image (along the z-axis) and searches for three or more pixel greyscales (or greyscale

[1]Interface points are found through local thresholding and parabolic fitting of the greyscale.

[2]If getinterface.in does not exist, get5.3 interactively creates the file for later use.

differences, if TM = 1 is selected) above a threshold. If TM = 0 is selected, the threshold is computed for each line as the average greyscale of that line plus TA ($10 - 40$ are good values for TA), if TM = 1 is selected, the threshold is computed from the average absolute differences between pixel greyscales in the line plus TA ($0 - 5$ are good values for TA).

A parabola is fitted to all values above threshold and the parabola tip is defined as the exact position of the interface. Almost all front interface points are found with this procedure, but usually also points from overgrown cells, sidebranches or dustspots. In the last step a pattern recognition algorithm determines, which points most probably constitute the interface. Finally, macros in the template *interface-new* will conveniently read all output data and create layouts for plots (in *Igor*).

The following options can be set in get5.3 (All options are preset to 1 unless otherwise noted):

- -e (0)1 : (dont't) extract images from framegrabber board. If the folder *images* contains the first image, this option is preset to 0.
- -a (0)1 : (dont't) extract possible interface points from images.
- -r (0)1 : (dont't) recognize most probable interface shape.
- -f (0)1 : (dont't) fourier transform the interface shape.

All definitions of data structures in headers and important program parts are listed below.

1. Get5.3.h: Main Program Header

```
// Header file to be used with get5.3.c
// created 5/10/97 by Wolfgang Losert
#ifndef PRGNAME
  #define PRGNAME "getinterface"
  #define VERSION "5.3"
  #define MINUS -1
  #define HORTH 640
  #define VERTH 480
  #define VER_MAG 3.29
  #define HOR_MAG 3.16
  #define BUFSIZ_OUT 256
  #define BUFSIZ_BIN 262144        // buffer for binary output
  #define BUFSIZ_DAT 8192          // buffer for data text output
  #define MAXFEAT  100             // maximum width of one feature
  #define RADIUS_MAX 50.           // max radius of fitted greyscale peak
  #define RADIUS_MIN 0.001         // min radius of fitted greyscale peak
  #define MAXINTENSITY 1000.0      // maximum intensity of fitted greyscale peak
  #define MAXPEAK  15              // Maximum number of preliminary peaks
  #define  MINFIT 3                /* Minimum number of points for a fit */
  #define MAX_FILELENGTH 90        // maximum file length
#endif
typedef struct _input_str {
  int      width;
  int     threshold;
  int      thresflag;
  int      end;
  int      start;
  int     length;
  long int   time_nom;
  long int  time_real;
} input_str;
typedef  struct _peak_str  {
  int        num;
  int        select;
  float      i[MAXPEAK];
  float       z[MAXPEAK];
  float      r[MAXPEAK];
} peak_str;
typedef  struct _para_str  {
  int        length;
  int        ext_data;
  float      dz_max;
  float      dz_mult;
  float      dz_ini;
  float      dz_start;
  float      r_max;
  float      r_min;
  float      r_mult;
  int        maxdust;
} para_str;
```

2. Get5.3.c: Main Program (important definitions are shown).

```
//  get5.3.c  by Wolfgang Losert 5/16/97
#define MIN_FT  0            // min point for FT
#define MAX_FT  475          // max point for FT
#define PMIN_PRE 2           // min number of nodes  in FT
#define PMAX_PRE 30          // max number of nodes in FT
#define NPONTOS_PRE 200      // number of points in FT
#include "get5.3.h"          // contains structures and constants
#include "qcbrdfun.h"        // board function acquire and initialize
#include "getdatin.h"        // input filenames and extraction parameters
char       infofile[MAX_FILELENGTH],tempfile[MAX_FILELENGTH];
char       tempold[MAX_FILELENGTH];
char      fourierfile[MAX_FILELENGTH],fourierdata[MAX_FILELENGTH];
char      timefile[MAX_FILELENGTH],fileName[MAX_FILELENGTH];
char      foldername[MAX_FILELENGTH],fileName2[MAX_FILELENGTH];

int        RANGE=600;            // total number of datapoints
int        menu_flag=0;          // =1: show a menu        =0: dont
int        input_flag=0;         // =1: input of parameters   =0: dont
```

```
int         extract_flag=0;       // =1: extract from tape  =0: dont extract
int         analyse_flag=1;       // =1: analyse binary data   =0: dont
int         recognize_flag=1;     // =1: do pattern recognition =0: dont
int         fourier_flag=1;       // =1: do fourier transform  =0: dont
int         MCID_flag=1;          // =1: save with MCID format  =0: dont
int         StartScan=0;
int         EndScan=-1;
char        buffer[BUFSIZ_OUT],*buffer_bin,*buffer_dat;
void handle_option(char *, char *);
void printline();
void goodbye(char *);
int   menu();
void  getname( int , char *, char *);
int    GetPeak(unsigned char *,int *, input_str *, peak_str *);
int    recognize(para_str , peak_str []);
int   getfourier(int , int , int , int , int , int , int ,
              char *, char *,char *, input_str []);
main( int argc, char *argv[] )
::::::::::::::
```

3. qcbrdfun.h: Definitions for functions that access the framegrabber board.

```
int     initialize(unsigned char **, int *, int *, short *);
int      acquire();
```

4. qcbrdfun.c: Relays commands to Data Translation 2255 frame grabber board.

5. getname.c: Adds number to filename

6. getdatin.h: Data input subroutine header

```
int  datain(char *, char *, char *, char *, char *, char *, char *, char *, char *);
int   read_getin(char *,input_str []);
int   write_getin(char *);
```

7. getdatin.c Data input subroutine

8. fourier.c: Smoothes interface shape and calls Fourier integral subroutine.

9. fourier-cont.c: Fourier integral subroutine.

```
//  autor   :   Jose Marcos e Orlando Abreu Gomes
//  Objetivo:   Este programa extra a transformada de fourier da interface
    obtida em cada imagem
//          e compara o resultado com a transformada de um seno,
        chamado de fourier analtico
//  modified:  11/22/96 by Wolfgang Losert
#include <stdio.h>
#include <stdlib.h>
#include <math.h>
float fourier_analitica(float, float);
```

```
float k_aux;

 void fourier(float *interface_pntr,float **spectrum, int hor,
 int pmn, int pmx, int n_pontos,
        float *A_max, float *k_max, float **fourier_anal, float *Err)
 /* programa para calcular transformada de fourier, via
  integracao numerica (sem usar FFT). esse programa usa os calculos
  feitos no caderno de laboratorio, pag. 89b a 90b  */
{
  int        i, j, i_max;   //variveis auxiliares
  float        aux;         //varivel auxiliar
  float    *spec;           //armazena os valores da transf. de Fourier
  float        k,dk;        // especifica o vetor de onda e o delta_k
  float       soma,sum,x,xx, kmn;  //variveis auxiliares na integrao
  float    coef[5];         //coeficientes para integrao
  float      pi2;           //2*PI
  float        Erro;        //armazena o erro entre o espectro analtico e o experimental
  /*****Define alguns valores iniciais*****/
  coef[0] = 0.3541666; // 17/48  *  coeficents for
  coef[1] = 1.2291667; // 59/48  *  numerical integration
  coef[2] = 0.8958333; // 43/48  *  obtained from
  coef[3] = 1.0208333; // 49/48  *  "numerical recipes" (page 108)
  pi2=8*atan(1.);    // o valor de 2*PI
  /*****Realiza a transformada de Fourier*****/
    /*****cria um ponteiro para armazenar os dados da transformada*****/
  spec = calloc(2*n_pontos+1,sizeof(float));
  if(!spec)
  {
     puts("\n not enough memory avaliable");
    exit(1);
    }
  *(spectrum) = spec;
    //liga o ponteiro do programa principal ao programa da subrotina
  /*****Integrao*****/
    /*****Define o valor inicial de k*****/
  kmn=pi2*(float)pmn/hor;
  /*****Define o valor do intervalo de integrao*****/
  dk=pi2*(float)(pmx-pmn)/(n_pontos*hor);
  /* nyquis frequency
  dk=pi2/2./(float)(hor);
  n_pontos= */
  for (j=0;j<=n_pontos;j++)
  {
    soma=0;
    sum=0;
    k=kmn+j*dk;
     for(i=0;i<4;i++)
      {
       x=  i;
      xx= i;
       soma = soma+coef[i]*(interface_pntr[i]*cos(k*x)+
         interface_pntr[hor-1-i]*cos(k*xx));
       sum =  sum+ coef[i]*(interface_pntr[i]*sin(k*x)+
          interface_pntr[hor-1-i]*sin(k*xx));
        }
    for(i=4;i<hor-4;i++)
      {
       x= i;
       soma = soma+interface_pntr[i]*cos(k*x);
       sum = sum+ interface_pntr[i]*sin(k*x);
      }
      spec[n_pontos+j+1]=k;
    spec[j] =(sum*sum+soma*soma)*4/pow(hor,2);
  }
  /*****Encontra o valor de A_max e k_max*****/
  aux=0;
  for(i=0; i<=n_pontos; i++)
    if(spec[i] > aux)
     { i_max=i; aux=spec[i]; }
  k_aux=spec[n_pontos+i_max+1];
  *A_max=pow(spec[i_max],0.5);    //escreve o valor no programa principal
  *k_max=k_aux;
  /*****Calcula o erro entre a curva de uma onda
   monocromtica( k_max ) e a transformada. experimental*****/
   Erro=0;
   for(i=0; i<=n_pontos; i++)
  Erro += pow( fourier_analitica(spec[n_pontos+i+1],
  (float)hor) - spec[i]/spec[i_max], 2);
  *Err=pow(Erro/n_pontos,0.5);  //escreve o valor no programa principal
```

```
  /*****cria um ponteiro para armazenar os dados da onda moncromtica*****/
  *(fourier_anal)=calloc(n_pontos+1, sizeof(float));
  /***** escreve o valor no programa principal*****/
  for(i=0;i<=n_pontos;i++)
    *(*fourier_anal+i)=(*A_max)*
    pow(fourier_analitica(spec[n_pontos+i+1], (float)hor), 0.5);
  /***** ajusta os valores do ponteiro spec *****/
  for(i=0;i<=n_pontos;i++)
    spec[i]=pow(spec[i], 0.5);
}
/*  &&&&&&&&&&&&&&&&&&&&&&&&&&&&&&&&&&&&&&&&&&&&&&&&&&&&&&&&&&&&&&&&&&&&  */
/***** Subrotina que calcula a transformada de uma onda monocromtica*****/
float fourier_analitica (float omega, float a)
{
  float aux, fourier;
  aux=omega*a;
  if(fabs(k_aux-omega)<0.00000001)
  {
   fourier  = pow(aux, 2) - sin(2*aux)*aux + pow(sin(aux),2);
   fourier /= (4.*pow(omega,2));
  }
  else
  {
   fourier  = pow((k_aux*cos(omega*a)*cos(k_aux*a) +
     omega*sin(omega*a)*sin(k_aux*a) - k_aux), 2) +
      pow((k_aux*sin(omega*a)*cos(k_aux*a) -
      omega*cos(omega*a)*sin(k_aux*a)),2);
   fourier /= pow((pow(k_aux,2)-pow(omega,2)), 2);
  }
  return(fourier*4/pow(a,2));
}
```

10. getpeaks.h:

```
int    GetPeak(unsigned char *,int *, input_str *, peak_str *);
int    recognize( int,int, peak_str *);
```

11. getpeaks.c: Interface extraction from image.

```
//  get_peaks  by Wolfgang Losert 5/06/97
/* ------------------------------------------------------ */
#include <stdio.h>
#include <stdlib.h>
#include <types.h>
#include <OSUtils.h>
#include <math.h>
#include <string.h>
#include <sane.h>
#include <ctype.h>
#include "get5.3.h"
#include "parabola.h"
int    checkPeak( int, int, float, float, float);
int   GetPeak(unsigned char *n_line, int *n_threshold,
       input_str *n_getin, peak_str *n_peak)
{
  static int    featCoor[MAXFEAT],featInt[MAXFEAT];
  int        i,peakCount,clusterLowEdge,clusterHighEdge,
           TooManyFlag;
  int        deltat,okflag;
  static int    summe,dsumme;
  float      fit_i,fit_z,fit_r;
/*  Scan the image line for all pixels with
  intensity differences above the  threshold */
  TooManyFlag=0;        // number of points above threshold
  peakCount = 0;        // number of peaks found
  clusterLowEdge =0;    // lower edge of point cluster above threshold
  clusterHighEdge=0;    // upper edge of point cluster above threshold
  summe=0;
  dsumme=0;
```

```
  if (n_getin->thresflag <2)
    {
    for (i=0;i<n_getin->length;++i)
      {
      summe =summe+n_line[i];
      if (i>0) dsumme = dsumme+abs(n_line[i]-n_line[i-1]);
      }
    if (n_getin->thresflag==0)
      *n_threshold = summe/n_getin->length + n_getin->threshold;
    else
      *n_threshold = dsumme/(n_getin->length - 1) + n_getin->threshold;
    }
  for (i=0;i<n_getin->length;i++)
    {
    if((n_getin->thresflag==1) ||(n_getin->thresflag==3))
      {
       if (i>0) deltat = (*(n_line+i)-*(n_line+i-1));
      else continue;
      }
    else
      deltat = (*(n_line+i));
    if ((deltat < *n_threshold ) || (i==n_getin->length -1))
      {
      if ((TooManyFlag >= MINFIT) && (TooManyFlag<= n_getin->width))
        {
        clusterHighEdge=TooManyFlag-1;
        clusterLowEdge=0;
        /* fit intensity profile of cluster and get peak*/
        if((okflag = FitPeak(TooManyFlag, clusterLowEdge,clusterHighEdge,
            featCoor, featInt,&fit_i,&fit_z, &fit_r))!=0)
          {
          /* check if peak is useful
          first  check of pattern recognition */
          if ((okflag = checkPeak(featCoor[0],featCoor[TooManyFlag-1],
                    fit_i,fit_z, fit_r))!=0)
            {
            n_peak->i[peakCount] = fit_i;
            n_peak->z[peakCount] = fit_z+n_getin->start;
            n_peak->r[peakCount] = fit_r;
            peakCount+=1;
            }
          }
        }
      TooManyFlag=0;
      continue;
      }
    ++TooManyFlag;
    if (TooManyFlag <= n_getin->width)
      {
      featCoor[TooManyFlag-1]  = i;
      featInt[TooManyFlag-1]  = deltat;
      }
    continue;
    }
  n_peak->num = peakCount;
  if (peakCount)
    return 1;         // if at least one peak was found
  else
    return 0;         // if no peak was found
  }
/*-------------------------------------------------------------------------------*/
int  checkPeak(int start, int end, float intensity, float z, float r)
  {
  if (((float)start > z) || ((float)end < z))
    return 0;              // position outside checked range
  else if ((intensity > MAXINTENSITY) || (intensity < 0))
    return 0;              // intensity of greyscale outside range
  else if ((RADIUS_MIN > r) || (RADIUS_MAX < r))
    return 0;              // radius outside range
  else
    return 1;
  }
```

12. parabola.h: Header for parabolic fit subroutine.

```
int    FitPeak( int, int, int, int *, int*, float *, float *, float *);
```

13. parabola.c: Parabolic fit soubroutine.

```
// parabola.c program makes parabolic fit
// by Wolfgang Losert 5/76/97

#include <stdio.h>
#include <stdlib.h>
#include <types.h>
#include <OSUtils.h>
#include <math.h>
#include <string.h>
#include <sane.h>
#include <ctype.h>
int  FitPeak(int npoints, int startIndex, int endIndex,
      int featCoor[],
    int featInt[],float  *intensity, float *z, float *r)
{
  static  int      i;
  static  extended   sx,sx2,sx3,sx4,sy,syx,syx2;
  static  extended   det,deta,detb,detc,fpoints,maximus,peakPosition;
  fpoints  = (extended) npoints;
  sx =0; sx2 = 0; sx3 = 0; sx4 = 0;
  sy = 0;  syx = 0; syx2 = 0; detb = 0; detc = 0;
  det=0.; deta=0.;
  for (i=startIndex; i<=endIndex; ++i)
    {
    sx += (extended)featCoor[i];
    sx2 += pow ((extended)featCoor[i],2.);
    sx3 += pow ((extended)featCoor[i],3.);
    sx4 += pow ((extended)featCoor[i],4.);
    sy += (extended)featInt[i];
    syx += (extended)featInt[i]*(extended)featCoor[i];
    syx2 += (extended)featInt[i]*pow((extended)featCoor[i],2.);
    }
  det  = fpoints*(sx2*sx4-sx3*sx3) + sx*(sx3*sx2 - sx*sx4) +
       sx2*(sx*sx3-sx2*sx2);
  deta = sy*(sx2*sx4-sx3*sx3)+syx*(sx2*sx3-sx*sx4)+
       syx2*(sx*sx3-sx2*sx2);
  detb = -sy*(sx*sx4-sx2*sx3)+syx*(fpoints*sx4-sx2*sx2)-
      syx2*(fpoints*sx3-sx*sx2);
  detc = sy*(sx*sx3-sx2*sx2)-syx*(fpoints*sx3-sx*sx2)
      +syx2*(fpoints*sx2-sx*sx);
  if ((det == 0) || (detc==0))
      return 0;         // some mistake since 0 determinante
  peakPosition  = (float)(-.5*detb/detc);
  *z = (float)peakPosition;
  maximus = (deta + peakPosition*.5*detb)/det;
  *intensity = (float)(maximus);
  *r= (float)(-.5/detc*det);
  return 1;             // found peaks
```

14. recognize.c: Pattern recognition algorithm for cellular arrays (get5.3).

```
//  recognize.c      by Wolfgang Losert 5/06/97
/* ------------------------------------------------------ */
#include <stdio.h>
#include <stdlib.h>
#include <types.h>
#include <math.h>
#include <sane.h>
#include <ctype.h>
#define DELTA_MAX 2.        // New point if one point has already been found
#define MAXDUST_PRE 10      // max number of points where nothing is found
#define RADIUS_MULT 4.      // maximum radius factor over average if
                            // interface moves forward ahead of mean int pos
#define DZ_MULT 7.          // maximum change in z in same direction
                            // as before (dz_old*DZ_MULT)
#define DZ_INI 10.          // maximum initial dev. from ave z
#define DZ_START 2.0        // maximum dz for start of check of result
                            // should be smaller than DZ_MAX
#include "get5.3.h"

/*=========================================================*/
/*  mechanism that selects   peak            */
/*=========================================================*/
```

```
int recognize(para_str para, peak_str peak[])
  {
  int   i,i2,i3,j,i_old,found,found2,found_last;
  int    count,count2,select,select2,verify;
  float  ave_z, ave_dz, ave_r, ave_i, ave_n;
  float  z1,z2,adz,dz1,dz2,z_old,z_older,next_peak;
  if (para.ext_data == 0)         // parameters for pattern recognition
      {
      para.dz_max=DELTA_MAX;
      para.dz_mult=DZ_MULT;
      para.dz_ini=DZ_INI;
      para.dz_start=DZ_START;
      para.r_max=RADIUS_MAX;
      para.r_min=RADIUS_MIN;
      para.r_mult=RADIUS_MULT;
      para.maxdust=MAXDUST_PRE;
      }
  ave_z = 0;              // calculate the averages
  ave_r = 0;
  ave_i = 0;
  ave_n = 0;
  for (i=0;i<para.length;++i)
    {
    ave_n+= peak[i].num;
    for (j=0;j< peak[i].num;j++)
      {
      ave_z+= peak[i].z[j];
      ave_i+= peak[i].i[j];
      ave_r+= peak[i].r[j];
      }
    }
  ave_z = ave_z / ave_n;
  ave_r = ave_r / ave_n;
  ave_i = ave_i / ave_n;
  ave_dz = 0;           // calculate the average dz
  for (i=0;i<para.length;++i)
    {
    for (j=0;j< peak[i].num;j++)
      {
      ave_dz+= fabs(peak[i].z[j]-ave_z);
      }
    }
  ave_dz = ave_dz / ave_n;
  printf("|z:%6.1f dz:%5.1f |",ave_z,ave_dz);
  found=0;
  z_old=0;
  z_older=-5000;
  found_last=0;
  for (i=0;i<para.length;++i)
    {
    count =  peak[i].num - 1;
    select=-1;
    for (j=count;j>=0;j--)
      {
      z1 = peak[i].z[j];
      if (select>=0)
        z2=peak[i].z[select];
      else
        z2=-10000;
      dz1 = z1 - z_old;
      dz2 = z_old - z_older;
      if (!found)          // select something close to the average
                // if nothing has been found before
        {
        if ((fabs(z1-ave_z) < para.dz_ini) && (select<0))
          {
          select=j;
          continue;
          }
        }
      else
        {
        if  ((fabs(dz1) < para.dz_max) && (fabs(z2-z_old) > para.dz_max))
          {
          select=j;
          continue;
          }
        adz=para.dz_max+para.dz_mult*dz2;
        if  ( ( ((dz1<adz)  && (dz1>0)) || ((dz1>adz)  && (dz1<0)) ) &&
          ((select <0)  || (dz1>0) ) )
          {
```

```
            select=j;
            continue;
            }
          // check if it is a dirtspot if ahead of interface
          }
        }
      /* if nothing good has been found since maxdust rewind and just take sth */
      if ((select<0) && (  (para.maxdust <= i-found_last) && (count>=0)))
          {
          i=found_last;
          do {
            i++;
            select=peak[i].num-1;
            } while (select<0);
          }
      /* if only something found in back */
      if ((select<0) && (count>=0))
        {
        for (;count>=0; count--)
        {
        if ((peak[i].z[count] < z_old) || (peak[i].z[count] < ave_z) || (!found))
          {
          i3=i;
          do {
            i3++;
            i2=peak[i3].num-1;
            if (i2 >=0)
              {
              next_peak=peak[i3].z[i2];
              if (fabs(next_peak - z_old) < para.dz_max*2.)
                {continue;}
              if (fabs(next_peak - peak[i].z[count]) < para.dz_max)
                {select=count;count=-1; continue;}
              if ( (found) && ((next_peak - peak[i].z[count]) < 0 )  &&
                   ((peak[i].z[count] - z_old) < 0) )
                   {select=count;count=-1; continue;}
              if ( (found) && (peak[i].z[count] < ave_z )  &&
                   ((peak[i].z[count] - z_old) < 0) &&
                  ((next_peak - z_old) < 0 )  &&
                  (fabs(peak[i].z[count]-ave_z) < 2*ave_dz) )
                   {select=count;count=-1; continue;}
              if ( (found) && ((next_peak - peak[i].z[count]) > 0 )  &&
                   ((peak[i].z[count] - z_old) > 0) )
                   {select=count;count=-1; continue;}
              }
            } while (peak[i3].num < 1);
          }
        }
        }
      peak[i].select = select;
      if (select>=0)
        {
        found+=1;
        found_last=i;
        z_older = z_old;
        select=peak[found_last].select;
        z_old = peak[found_last].z[select];
        }
      }
    /* now scan backward along all points only look for better points - dont eliminate*/
    found2=0;
    for (i=para.length-para.maxdust;i>=0;i--)
      {
      if (!found2)
        i_old=i+1;
      count = peak[i].num - 1;
      count2 = peak[i_old].num - 1;
      select= peak[i].select;
      select2 = peak[i_old].select;
      if (!found2)
        {
        if ((select<0) || (select2<0))
          continue;
        if ((fabs(peak[i].z[select] - peak[i_old].z[select2]) > para.dz_start ) ||
          (peak[i].z[select] < ave_z ))
          continue;
        found2=1;
        z_old=peak[i].z[select];
        z_older=peak[i_old].z[select2];
        i_old=i;
```

```
      continue;
      }
    verify=0;
    for (j=count;j>=0;j--)
      {
      z1 = peak[i].z[j];
      if (select<0)
        z2=0;
      else
        z2=peak[i].z[select];
      dz1 = z1 - z_old;
      dz2=z_old-z_older;
      if  ((fabs(dz1) < para.dz_max) && ((verify==0) ||
          (fabs(z2-z_old) > para.dz_max)) )
        {
        select=j;
        verify=1;
        continue;
        }
      adz=para.dz_max+para.dz_mult*dz2*(float)(i_old-i);
      if ( (((dz1>adz)  && (dz1<0)) || ((dz1<adz)  && (dz1>0))) &&
         (verify==0)  &&
         ( (fabs(z1-ave_z) <= fabs(z2-ave_z)) || (fabs(z1-ave_z) < ave_dz) ) )
        {
        select=j;
        verify=1;
        continue;
        }
      }
    if (verify==1)
      {
      peak[i].select=select;
      if ((select<0) || (select2<0))
        {
        printf("MISTAKE AT i=%i: select=%i select2=%i\n",i,select,select2);
        return(0);
        }
      z_old=peak[i].z[select];
      z_older=peak[i_old].z[select2];
      i_old=i;
      if ( (z_old<ave_z) && (z_older < ave_z) &&
        (fabs(z_old-z_older) < para.dz_max) )
        found2=0;
      }
    else
      {
      found2=0;
      continue;
      }
    }
  return (found);
  }
```

15. recognize-dend.c: Pattern recognition algorithm for dendrites (get5.3d).

```
//   recognize.c          by Wolfgang Losert 5/06/97
// recognize_dend.c  modified 1/21/98 to recognize dendrites
/* ------------------------------------------------------- */
#include <stdio.h>
#include <stdlib.h>
#include <types.h>
#include <math.h>
#include <sane.h>
#include <ctype.h>
#include <OSUtils.h>
#define DELTA_MAX 4.              // New point if one point has already been found
#define MAXDUST_PRE 150           // max number of points where nothing is found
#define RADIUS_MULT 4.            // maximum radius factor over average if
                                  // interface moves forward ahead of mean int pos
#define DZ_MULT 7.                // maximum change in z in same direction
                                  // as before (dz_old*DZ_MULT)
#define DZ_INI 10.                // maximum initial dev. from ave z
#define DZ_START 2.0              // maximum dz for start of check of result
                                  // should be smaller than DZ_MAX
#define MAXDENDS 50               // Maximum number of dendrite tips
#define DIST_MAX 3.0              // maximum distance between points in z-direction
#define MIN_RATIO    .7           // minimum ratio for found points vs checked lines
```

```
#define MIN_NUMBER  8              // minimum number of points per dendrite tip
#define POINTS_MAX  8              // number of points in each direction
                                   //  where one looks for dendrite tip
#define ELIMINATE_ANGLE 1          // angle beyond which peaks behind will be eliminated
#define DX_MAX 4                   // maximum x distance without points
#define   MAX_DEV   1.5            // maximum deviation of parabola tip from largest point
#define   MAX_RAD_DEND   20        // maximum dendrite tip radius
#define   MIN_RAD_DEND   0.5       // minimum dendrite tip radius
#include "get5.3.h"

/*=======================================================*/
/*  mechanism that selects       peak                    */
/*=======================================================*/
peak_str   findbig(float,para_str,peak_str []);
int      floatPeak( int, float*, float*, float *, float *, float *);

int recognize(para_str para, peak_str peak[])
   {
   int    i,j,k,k2,start_i,end_i,x_pos,number_1,found,peak_num;
   int      okflag,n_points,taken;
    float   *featzpos,*featxpos;
   float   distance,distance_new,z_initial;
   peak_str  big_z,peak_now;
   float         fit_i,fit_z,fit_r;
   featzpos = calloc((POINTS_MAX*2+2),sizeof(float));          //   allocate memory
      if(!featzpos)    {     puts("\n not enough memory avaliable"); exit(1); }
   featxpos = calloc((POINTS_MAX*2+2),sizeof(float));          //   allocate memory
      if(!featxpos)    {     puts("\n not enough memory avaliable"); exit(1); }
   if (para.ext_data == 0)             // parameters for pattern recognition
         {
         para.dz_max=DELTA_MAX;
         para.dz_mult=DZ_MULT;
         para.dz_ini=DZ_INI;
         para.dz_start=DZ_START;
         para.r_max=RADIUS_MAX;
         para.r_min=RADIUS_MIN;
         para.r_mult=RADIUS_MULT;
         para.maxdust=MAXDUST_PRE;
         }
   for (i=0;i<para.length;i++)
      {
      peak[i].z[MAXPEAK-1]=0;       // prepare for dendrite tip entering
      }
   number_1=0;
   found=0;
   peak_num=0;
   z_initial=10000.0;
   big_z = findbig(z_initial,para,peak);   // find biggest z position
   do
      {
      x_pos=big_z.num;
      peak_now = big_z;
      peak[x_pos].select = big_z.select;
      end_i=x_pos;
      start_i=x_pos;
      k=0;
      k2=0;
      for (i=x_pos+1;i<=x_pos+POINTS_MAX;i++)
         {
         if ((i>=0) && (i<para.length))
            {
            if (( abs(peak_now.num-i) > DX_MAX) || (peak[i].select>=0))
               {
               i=x_pos+POINTS_MAX;
               continue;
               }
            k2=k2+1;
            distance=DIST_MAX*fabs((float)(peak_now.num-i));
            for (j=0;j< peak[i].num;j++)
               {
               distance_new=pow(pow((peak[i].z[j]-peak_now.z[0]),2) +
pow(((float)(i-peak_now.num)),2),0.5);
               if ((distance_new < distance) && (peak[i].z[j]>0))
                  {
                  peak[i].select=j;
                  peak_now.z[0]=peak[i].z[j];
                  peak_now.num=i;
                  end_i=i;
                  distance = distance_new;
                  }
               }
```

```
            if (peak[i].select >= 0)
                k=k+1;
            }
         }
      peak_now = big_z;
      for (i=x_pos-1;i>=x_pos-POINTS_MAX;i--)
         {
         if ((i>=0) && (i<para.length))
            {
            if (( abs(peak_now.num-i) > DX_MAX) || (peak[i].select>=0))
               {
               i=x_pos-POINTS_MAX;
               continue;
               }
            k2=k2+1;
            distance=DIST_MAX*fabs((float)(peak_now.num-i));
            for (j=0;j< peak[i].num;j++)
               {
               distance_new=pow(pow((peak[i].z[j]-peak_now.z[0]),2) +
pow(((float)(i-peak_now.num)),2),0.5);
               if ((distance_new < distance) && (peak[i].z[j]>0))
                  {
                  peak[i].select=j;
                  peak_now.z[0]=peak[i].z[j];
                  peak_now.num=i;
                  start_i=i;
                  distance = distance_new;
                  }
               }
            if (peak[i].select >= 0)
               k=k+1;
            }
         }
      if (((float)k2 < MIN_RATIO * (float)k ) || (k < MIN_NUMBER))
         {
         for (i=start_i;i<=end_i;i++)
            {
            peak[i].select=-1;
            }
         }
      else
         {
         // check if nice parabolic fit
         n_points=0;
         for (i=start_i;i<=end_i;i++)
            {
            taken=peak[i].select;
            if (taken>=0)
               {
               featzpos[n_points]=(peak[i].z[taken]-big_z.z[0]);
               featxpos[n_points]=(float)(i-big_z.num);
               n_points++;
               }
            }
         if((okflag = floatPeak(n_points,featzpos, featxpos,&fit_i,&fit_z, &fit_r))!=0)
            {
            if (peak[peak_num].num >= MAXPEAK)
               printf("WARNING: OVERWRITING POINTS WITH DENDRITE TIPS\n");
            peak[peak_num].z[MAXPEAK-1] = fit_z+big_z.z[0];
            peak[peak_num].i[MAXPEAK-1] = fit_i+(float)big_z.num;
            peak[peak_num].r[MAXPEAK-1] = fit_r;
            peak_num++;
            for (i=start_i;i<=end_i;i++)
               {
               for (j=0;j<peak[i].select;j++)
                  {
                  peak[i].z[j]=0;
                  }
               for (j=peak[i].num-1;j>peak[i].select;j--)
                  {
                  peak[i].z[j]=0;
                  }
               if (peak[i].select>=0)
                  {
                  number_1++;
                  }
               }
            for (i=0;i<para.length;i++)
               {
               for (j=0;j<peak[i].num;j++)
                  {
                  if ((peak[i].z[j] < big_z.z[0]-ELIMINATE_ANGLE*
```

```
                        fabs((float)(big_z.num-i))) && (peak[i].select<0))
                    {
                    peak[i].z[j]=0;
                    }
                }
            }
         found=1;
         }
      else
         {
         for (i=start_i;i<=end_i;i++)
            {
            peak[i].select=-1;
            }
         }
      }
   z_initial=big_z.z[0];
   big_z = findbig(z_initial,para,peak);          // find biggest z position
   } while (big_z.z[0]>0);
   for (i=1;i<peak_num;i++)          // bring into order
      {
      for (j=0;j<i;j++)
         {
         if (peak[i].i[MAXPEAK-1] < peak[j].i[MAXPEAK-1])
            {
            big_z.z[0]=peak[j].z[MAXPEAK-1];
            big_z.i[0]=peak[j].i[MAXPEAK-1];
            big_z.r[0]=peak[j].r[MAXPEAK-1];
            peak[j].z[MAXPEAK-1]=peak[i].z[MAXPEAK-1];
            peak[j].i[MAXPEAK-1]=peak[i].i[MAXPEAK-1];
            peak[j].r[MAXPEAK-1]=peak[i].r[MAXPEAK-1];
            peak[i].z[MAXPEAK-1]=big_z.z[0];
            peak[i].i[MAXPEAK-1]=big_z.i[0];
            peak[i].r[MAXPEAK-1]=big_z.r[0];
            }
         }
      }
   return (number_1);
   }

peak_str findbig(float z_ini,para_str para_s,peak_str peak_s[])
   {
   int i,j;
   float z_max;
   peak_str thatsit;
   z_max=0.1;
   thatsit.z[0] = 0;
   thatsit.select=-1;
   for (i=0;i<para_s.length;++i)
      {
      for (j=0;j< peak_s[i].num;j++)
         {
         if ((peak_s[i].z[j] > z_max) && (peak_s[i].z[j] < z_ini) && (peak_s[i].select<0))
            {
            z_max = peak_s[i].z[j];
            thatsit.z[0] = peak_s[i].z[j];
            thatsit.r[0] = peak_s[i].r[j];
            thatsit.num = i;
            thatsit.select=j;
            }
         }
      }
   return (thatsit);
   }
int   floatPeak(int npoints, float featz[], float featx[],
float *intensity, float *z, float *r)
{
   int         ie;
   float    bsx,bsx2,bsx3,bsx4,bsy,bsyx,bsyx2;
   float    bdet,bdeta,bdetb,bdetc,bfpoints,bmaximus,bpeakPosition;
   bfpoints   = (float)npoints;
   bsx =0; bsx2 = 0; bsx3 = 0; bsx4 = 0;
   bsy = 0;  bsyx = 0; bsyx2 = 0; bdetb = 0; bdetc = 0;
   bdet=0.; bdeta=0.;
   for (ie=0; ie<npoints; ++ie)
      {
      bsx += featx[ie];
      bsx2 += pow(featx[ie],2.);
      bsx3 += pow(featx[ie],3.);
      bsx4 += pow(featx[ie],4.);
      bsy += featz[ie];
```

```
    bsyx += featz[ie] * featx[ie];
     bsyx2 += featz[ie] * pow(featx[ie],2.);
    }
bdet  = bfpoints*(bsx2*bsx4-bsx3*bsx3) + bsx*(bsx3*bsx2 - bsx*bsx4) +
        bsx2*(bsx*bsx3-bsx2*bsx2);
bdeta = bsy*(bsx2*bsx4-bsx3*bsx3)+bsyx*(bsx2*bsx3-bsx*bsx4)+
        bsyx2*(bsx*bsx3-bsx2*bsx2);
bdetb = -bsy*(bsx*bsx4-bsx2*bsx3)+bsyx*(bfpoints*bsx4-bsx2*bsx2)-
      bsyx2*(bfpoints*bsx3-bsx*bsx2);
bdetc = bsy*(bsx*bsx3-bsx2*bsx2)-bsyx*(bfpoints*bsx3-bsx*bsx2)
      +bsyx2*(bfpoints*bsx2-bsx*bsx);
if ((bdet == 0) || (bdetc==0))
      return 0;                    // some mistake since 0 determinante
bpeakPosition   = (float)(-.5*bdetb/bdetc);
*intensity = (float)bpeakPosition;
bmaximus = (bdeta + bpeakPosition*.5*bdetb)/bdet;
*z = (float)(bmaximus);
*r= (float)(-.5/bdetc*bdet);
if (((*intensity > npoints) || (*intensity < 0)) ||
   ((*z > MAX_DEV) || (*z < -MAX_DEV)) ||
   ((*r > MAX_RAD_DEND) || (*r < MIN_RAD_DEND)))
   return 0;                  // peak in wrong place
else
   return 1;                           // found peaks
}
```

Appendix B

Sample Preparation Procedure

The following sample preparation process was developed by D. Liu and others in this laboratory:

1. **Vacuum distillation of Succinonitrile:** $750g$ of Succinonitrile with 99% purity (Fluka) are filled into a flask, connected to a vacuum distillation apparatus. The SCN is distilled under a vacuum of $\sim 100 - 200$mTorr, while the source flask is held at $\sim 110^{o}$C and the condenser at $\sim 80^{o}$C. The middle $40\% - 60\%$ of the SCN is distilled into a flask with vacuum tight seal. This flask is then used as the source flask in a second distillation, where again the middle $40\% - 60\%$ of SCN is distilled into a vacuum tight flask for a third and possibly for a fourth distillation. In the last distillation a 25ml graded glass buret is filled, which was modified to allow vacuum tight sealing on both ends.

2. **Capillary cleaning:** The thin (0.1 × 2.0 × 300mm) glass capillaries (Vitro Dynamics) are cleaned before use. Both ends of the capillary are inserted into Teflon holders that are connected air tight on the top to a funnel and on the bottom to a flask that is held constantly at slightly low pressure. This creates sufficient suction to let even the viscous Cromerge flow through the thin capillary. The capillary is flushed (in this order) with detergent, distilled water, acetone, chromic acid, and distilled water. After the capillary is baked overnight at high temperature > 130°C inside a vacuum tube, both ends of the capillary are sealed with a torch.

3. **Sample filling:** A schematic of the capillary loading apparatus is shown in figure B.1. A measured amount of C152 ($\sim 3 - 30$mg) and a magnetic stirrer are inserted into the mixing flask. Three necks of the mixing flask are connected to inlet adaptors, Rubber covers ($\sim$ 3mm thick) are clamped onto the adaptors with screwcaps for a vacuum tight seal of the inlet. One capillary (dipped in vacuum grease) is inserted in the outward direction (to keep the end of the capillary that is dipped into SCN clean) into each of those inlet adaptors through a small slit in the rubber. The sealed tips of the capillary ends inside the flask are broken off, and the adaptors are inserted into the mixing flask. The capillary end is positioned above the expected level of SCN filling. The mixing flask is ice cooled to avoid sublimation losses. After vacuum is established in the filling apparatus, the vacuum pump is switched off briefly while the buret valve is opened and a measured amount ($\sim$ 8ml) of

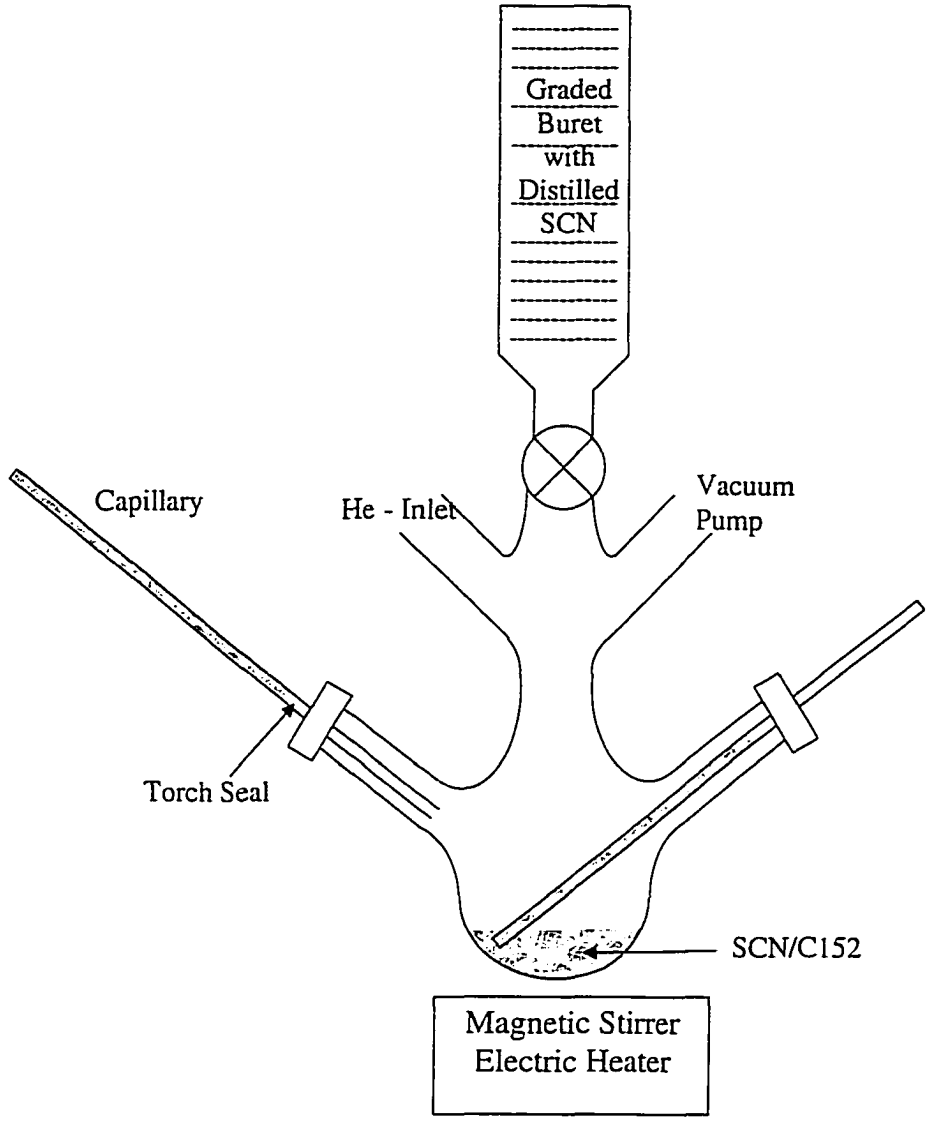

Figure B.1: Schematic of the capillary filling procedure.

SCN is filled into the flask and quickly solidifies in the chilled mixing flask. The vacuum pump is switched on to reestablish good vacuum. The mixing flask is brought in contact with a heater of $\sim 80^{o}$C and the vacuum pump is switched off (in order to minimize sublimation losses). The SCN rapidly melts and is mixed with C152 with a magnetic stirrer for about $3-5$ minutes. The vacuum pump is switched on again after the stirrer is stopped. The capillaries are heated and lowered into the liquid SCN/C152 mixture and capillary action fills the capillary approximately half. The Helium valve (triple valve for very low pressure) is then carefully opened and Helium pressure fills the capillaries completely. The heating of the capillaries is stopped and the mixture solidifies rapidly inside the capillaries, preventing it from flowing back out as the Helium is switched off. The capillaries are now raised and sample material is removed (by carefully locally heating that part of the sample with a heatgun) from the end of the capillary inside the mixing flask. The capillaries are finally tipped off with a torch. The area, where the capillary is tipped off, has to be cleaned from any material through repeated heating with a heatgun and several brief swipes across the capillary with the torch (this removes residues sticking to the glass), prior to tipping the capillary off.[1]

[1]One improvement of the filling procedure was recently developed by R. Ragnarsson *et al* [106]: Instead of moving the capillaries, it is possible to fix the ends of all capillaries close to one sidewall of the mixing flask. During filling the whole apparatus is then tilted sideways in order to bring

In this process three samples with equal concentration are produced, which are never exposed to air after the first distillation. The purity of the resulting samples is verified with a "Chester test" on a pure sample, as explained in section 3.2.2. Sample lifetimes are more than one year, limited mainly by accidental breaking of the glass capillaries.

---

the SCN to the capillary ends. In this case the capillaries can be sealed in place e.g. with glass powder for the whole filling process. This avoids possible contamination through the vacuum grease and eliminates the danger of losing the vacuum through a bad rubber seal.

Appendix C

Phase Field Model Simulations

This appendix was written by J. Kopzcyński, W.-J. Rappel and A. Karma as part of a collaborative publication [4] and is included unaltered in this thesis.[1]

C.1 Numerical Methods

The phase-field method, originally introduced by Langer [68], has recently emerged as the method of choice for the simulation of complex solidification processes [85, 69, 126, 72, 127] The method is extremely attractive when dealing with large systems and/or complicated geometries since solid-liquid interfaces, in contrast to conventional simulation techniques, do not need to be tracked explicitly. Furthermore, a recent higher order, asymptotic analysis has enabled simulations with a

[1]The research in this section was supported by the U.S. Department of Energy under grant No. DE-FG02-92ER45471 and benefited from CRAY time at the National Energy Resources Supercomputer Center.

vanishing kinetic coefficient and that result in an enormous gain in computational efficiency [74]. With these new asymptotics, it is possible to perform numerically converged and therefore *quantitatively accurate* phase-field simulations. The method has been successfully applied to dendritic growth in both 2D [74] and 3D [75] and to directional solidification [85].

In this section we will use the phase-field method to simulate the growth of a large sample under conditions that are similar to the ones described in the previous section. Our results can then be used to compare qualitatively to the experimental results. A direct quantitative comparison is at this point not possible; the phase-field method simulates the symmetric model which assumes that the diffusion constant is the same in the liquid and in the solid. The experiment, on the other hand, can be better described by the one-sided model which assumes that the diffusion constant in the solid is much smaller than in the liquid. Furthermore, the phase-field model assumes that the liquidus and the solidus have equal slope which is not the case in the experiment. Nevertheless, as we will see below, the qualitative agreement between the experiments and the simulations is excellent and we do not expect a significant difference for simulations using the one-sided model.

Rather than giving an exhaustive presentation of the phase-field method, we refer to our previous work [120, 85] for details. In short, the method consists of introducing an order parameter ψ that takes on one value in the solid and one value in the liquid. It varies smoothly between the two values across a narrow region of

width W. The dynamics of this order parameter is determined by minimizing a free energy which has minima corresponding to the liquid and to the solid state. The precise form of this free energy is somewhat arbitrary but one that leaves the extrema at $\psi = \pm 1$ and is computationally advantageous leads to the following equation in the frame moving with the pulling speed V_P:

$$\begin{aligned}
&\tau(\mathbf{n})\,(\partial_t - V_P\,\partial_z)\psi = \\
&-(\psi^2-1)\left(\psi + \bar{\lambda}\,(\psi^2-1)\,(u + \tfrac{z-z_0}{l_T})\right) \\
&+ \vec{\nabla}\cdot(W(\mathbf{n})^2\vec{\nabla}\psi) \\
&+ \partial_x\left(|\nabla\psi|^2 W(\mathbf{n})\tfrac{\partial W(\mathbf{n})}{\partial \psi_x}\right) + \partial_z\left(|\nabla\psi|^2 W(\mathbf{n})\tfrac{\partial W(\mathbf{n})}{\partial \psi_z}\right)
\end{aligned} \tag{C.1}$$

Here, $u \equiv \bar{\mu}\,/\,(\Delta C_0\,(\partial\mu/\partial C))$ is the dimensionless chemical potential field, $\bar{\mu} \equiv \mu - \mu_{eq}(T_0) - \partial\mu/\partial T|_{T=T_0}$ is the departure of the chemical potential μ of solute molecules relative to the solvent from its equilibrium value, z is the pulling direction, z_0 is the position of the steady planar interface, $\bar{\lambda}$ is a coupling constant and l_T is the thermal length. The width $W(\mathbf{n})$ and the constant relaxation time $\tau(\mathbf{n})$ depend on the normal direction to the interface $\mathbf{n}$ which allows us to include anisotropy in the model [85]. The order parameter is then coupled to the dimensionless chemical potential field u which leads to the following equation:

$$(\partial_t - V_P\,\partial_z)\,u \;=\; D\,\nabla^2 u + \frac{1}{2}\,(\partial_t - V_P\,\partial_z)\,\psi \tag{C.2}$$

where D is the diffusion constant. The last term in this equation represent the rejection of impurities from the solid phase into the liquid phase.

In the limit where the interface is curved over a scale that is much smaller than

W ($\kappa W << 1$) and where the interface Peclet number $p = V_P W/D$ is much smaller that unity ($p << 1$), it can be shown [85] that the above equations reduce to the standard sharp interface equations for the symmetric model [128] with a constant miscibility gap:

$$(\partial_t - V_P\,\partial_z)\,u \;=\; D\,\nabla^2 u \tag{C.3}$$

$$u_{int} \;=\; -\,d_0(\mathbf{n})\,\kappa \;-\; (z_{int} - z_0)/l_T \tag{C.4}$$

$$V_n \;=\; D\,(\,\partial_{\mathrm{n}} u\,|_S \;-\; \partial_{\mathrm{n}} u\,|_L) \tag{C.5}$$

$$u(\infty) = -1 \tag{C.6}$$

where z_{int} is the position of the interface, κ is the local interface curvature, V_n is the normal interface speed, $d_0(\mathbf{n})$ is the capillary length.

The implementation of Eqns. C.1,C.2 on a discrete square grid with coordinates i, j is straightforward and, along with other numerical details, is explained in detail in [85]. To minimize CPU time, we chose as an initial condition for the simulations reported here the converged planar solution corresponding to a pulling speed V_P. This solution is one-dimensional and depends only on the grid coordinate in the pulling direction j: $u_0(j), \psi_0(j)$. We have verified that different initial conditions (corresponding to the u and ψ fields of a planar interface at rest) resulted in identical qualitative results. In all our simulations the pulling speed was chosen to be higher than the critical pulling speed given by the Mullins Sekerka instability V_C: $V_P = 5V_C$. Note that even though $V_P > V_C$ the interface remains planar since the numerically introduced perturbations are not large enough to destabilize the

interface. The grid size in our simulations was chosen as $\Delta x = 0.8$ with a time step of $\Delta t = 0.073$. The numerical consequences of such a large grid size are discussed at length in [85].

C.2 Numerical Results

We have focused our simulations in the region where we can expect doublets based on our previous work [62, 21]. There, we performed a linear stability analysis of the steady state cellular interface using a Green's function approach. Although we used the standard symmetric model with non-constant miscibility gap we will see below that all results carry directly over to the case of constant miscibility gap simulated by the phase field method.

We found that there exists a stable band of cellular solutions which size depends strongly on the anisotropy strength. For anisotropy values below a critical value the band disappears and there are no stable cellular solutions. Above this critical value the size of the band increases as the anisotropy is increased. We found that for the anisotropy value considered in this study (1%) there is a narrow band of stable solutions. In addition, we found that there are two sets of multiplet solutions that bifurcate off the main branch [21]. These multiplets are structures that consists of repeating cellular subunits, each containing a set of distinct cells separated by unequal grooves. The simplest multiplet is the doublet which is the focus of this paper. The Eckhaus instability and the fold were found to act as accumulation points for the two sets. The multiplets bifurcating near the low wavelength accu-

mulation point (the Eckhaus instability) do not to resemble stable experimental multiplets while the ones bifurcating near the fold with higher wavelengths have morphologies similar to experimental multiplets. The first multiplet bifurcating off the main branch as one approaches the fold from the low wavelength side is the doublet branch. These results indicate that the region where one might expect doublets with morphologies that resemble experimental doublets is near the fold of the main branch.

Using the phase-field method, we first reconstructed the main branch of cellular solutions, its stable band and the branch of doublets bifurcating near the fold. The main branch was reconstructed using a computational box with a width equal to half a wavelength λ and a sinusoidal perturbation of the interface as initial condition. From the previous study on the stability of the main branch we know that the stable band of cells is limited on both the short and long wavelength side by instabilities that have a wavelength that is twice the wavelength of the underlying cellular structure. This enables us to determine this band using the phase-field method by taking a computational box that contains two cells, and by perturbing these two cells with a 2λ perturbation. Stable cells are characterized by perturbations that damp out in time while the perturbations for unstable cells grow in time. The doublet branch was reconstructed in a similar fashion as the main branch: we start with a computational box with a sinusoidal perturbation. For a wavelength bigger that the wavelength of the fold, we found that a doublet was selected. Once on the doublet branch, it is easy to follow it to higher and

lower wavelengths. Having established the doublet branch, we examined its stability against perturbations of various wavelengths in the same way as the main branch. We found that the stable band is limited by oscillatory instabilities of the wavelength of a single doublet in both the low and the high spacings regime. On the low spacings side, the stability limiting mode is asymmetric with respect to the doublet center (the shallow groove) and causes doublet peaks to oscillate. On the high spacings side, the first unstable mode is symmetric and both long sides of a doublet prone to this mode perform a breathing or a waving motion. The branch structure and the stability regions are shown in Fig. C.1 where we show the tip undercooling $\Delta = 1 - (z_{tip} - z_0)/l_T$, where z_{tip} is the position of the tip, as a function of the dimensionless wavelength, $Pe = \lambda V_P/(nD)$ ($n = 1$ for cells on the main branch and $n = 2$ for doublets).

In our first large scale simulation we added small random noise to the initial condition by randomly shifting the ψ_0 and u_0 fields along the z axis. This initial perturbation is sufficient to destabilize the planar interface.

The phase-field enables us to choose a very large computational box, making this simulation equivalent to experiment 2 in Sec. II.B. A sequence of interfaces for different times is shown in Fig. C.2. As in the experiment, the interface undergoes continuous tip splitting and cell overgrowth and shows signs of developing doublet structures. However, even after continuing this simulation four times longer than in the figure, the interface never reaches a steady-state. Different initial conditions than the one described above lead to the same qualitative picture. Therefore, in

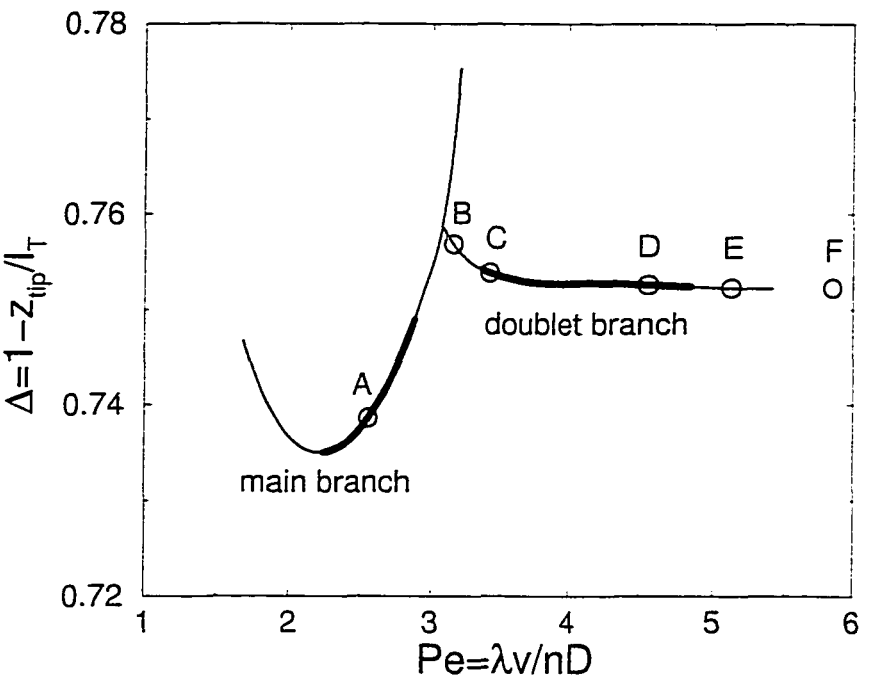

Figure C.1: The branch structure as calculated by the phase-field method. The stable part of the main (cellular) and doublet branch is indicated by the thick line. The symbols correspond to the various simulations shown in this paper.

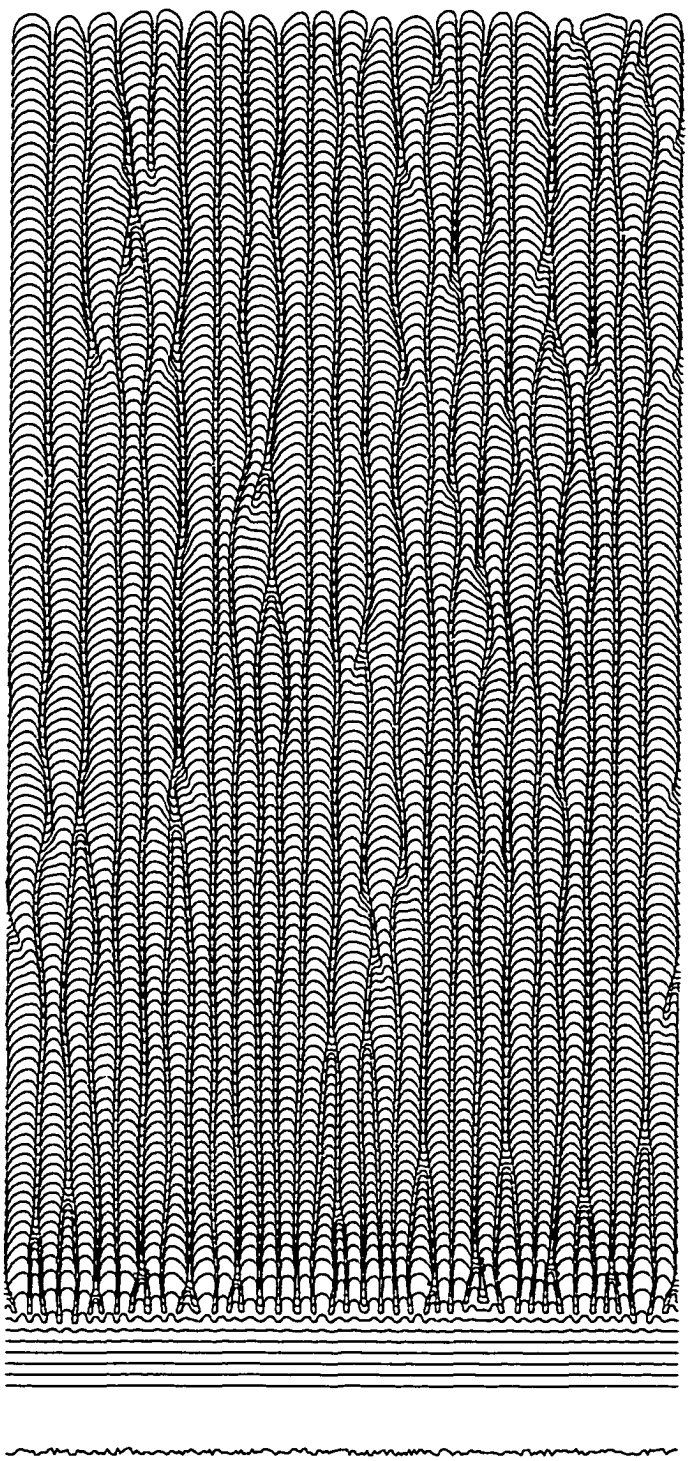

Figure C.2: The evolution of the interface for $V_P = 5V_C$. The initial condition was the converged planar state with a small random noise (magnified 1000 times in vertical direction for clarity). The system never settles in a steady-state.

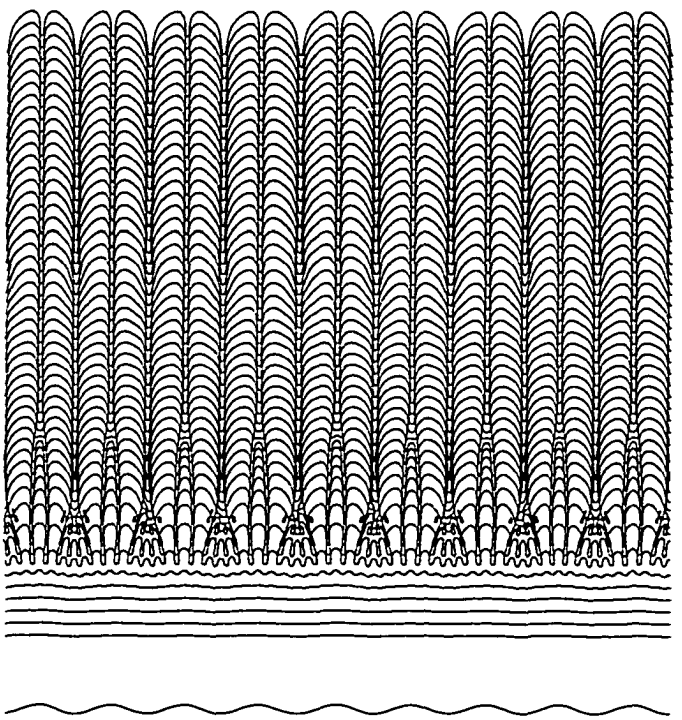

Figure C.3: The evolution of the interface for $V_P = 5V_C$. The initial condition was the converged planar state with a small perturbation with wavelength $\lambda_P = 181.96$ (magnified 10 times in vertical direction for clarity). The system settles in a periodic array of doublets.

full agreement with the results of the experiments, the simulations indicate that no stable doublet state can be reached dynamically from a planar interface for this value of the surface tension anisotropy ($\epsilon = 1\%$).

To investigate the effect of a sinusoidal perturbation of the interface, as utilized in the experiments, we applied a small perturbation with a fixed wavelength λ_P to both the ψ and u fields. Specifically, we applied a perturbation of the form

$$u(i,j) = u_0(j\Delta x - A\cos\left(\frac{2\pi i\Delta x}{\lambda_P}\right)) \tag{C.7}$$

and a similar expression for $\psi(i,j)$. Typically, we chose for the amplitude one grid

point, i.e. $A = \Delta x$. To find the values of the fields at the new grid points we used a linear interpolation. We have verified that different perturbations, such as square wave, gave the same qualitative result. The results of a periodic perturbation with a wavelength that leads to stable doublets is shown in Fig. C.3. The wavelength of the perturbation, $\lambda_P = 181.96$ corresponds to point D in Fig. C.1. After the initial transient the interface quickly settles into a stable period array of doublets. Note that, as in the experiments, the final state has the same wavelength as the perturbation.

Further investigation revealed that there exists a stable domain of doublets that can be reached dynamically with the aid of the periodic perturbation. This domain is represented by the thick solid part of the doublet branch in Fig. C.1. This domain approaches, but does not reach, the main branch. Close to the main branch, the final steady state consists of doublets that are less pronounced (more symmetric). An example of such a state is shown in Fig. C.4, which corresponds to point C in Fig. C.1 with $\lambda_P = 136.47$. In this case the dynamics of doublet formation are very similar to experiment 1.

The unstable part of the doublet branch that connects it with the main branch is characterized by solutions that display an oscillatory mode discussed earlier. This can be seen in Fig. C.5 corresponding to the initial perturbation with $\lambda_P = 125.97$ (point B in Fig. C.1).

This instability is very similar in nature to the oscillatory mode limiting the stable part of the main branch at higher spacings explored in [85, 84]. In agreement

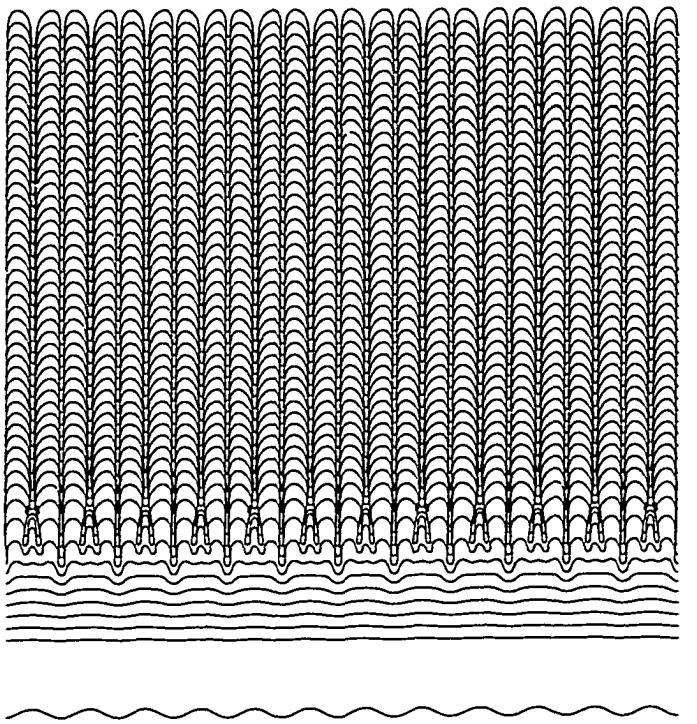

Figure C.4: As Fig. C.3 but now with $\lambda_P = 136.47$. The system settles in stable doublets of the smaller wavelength.

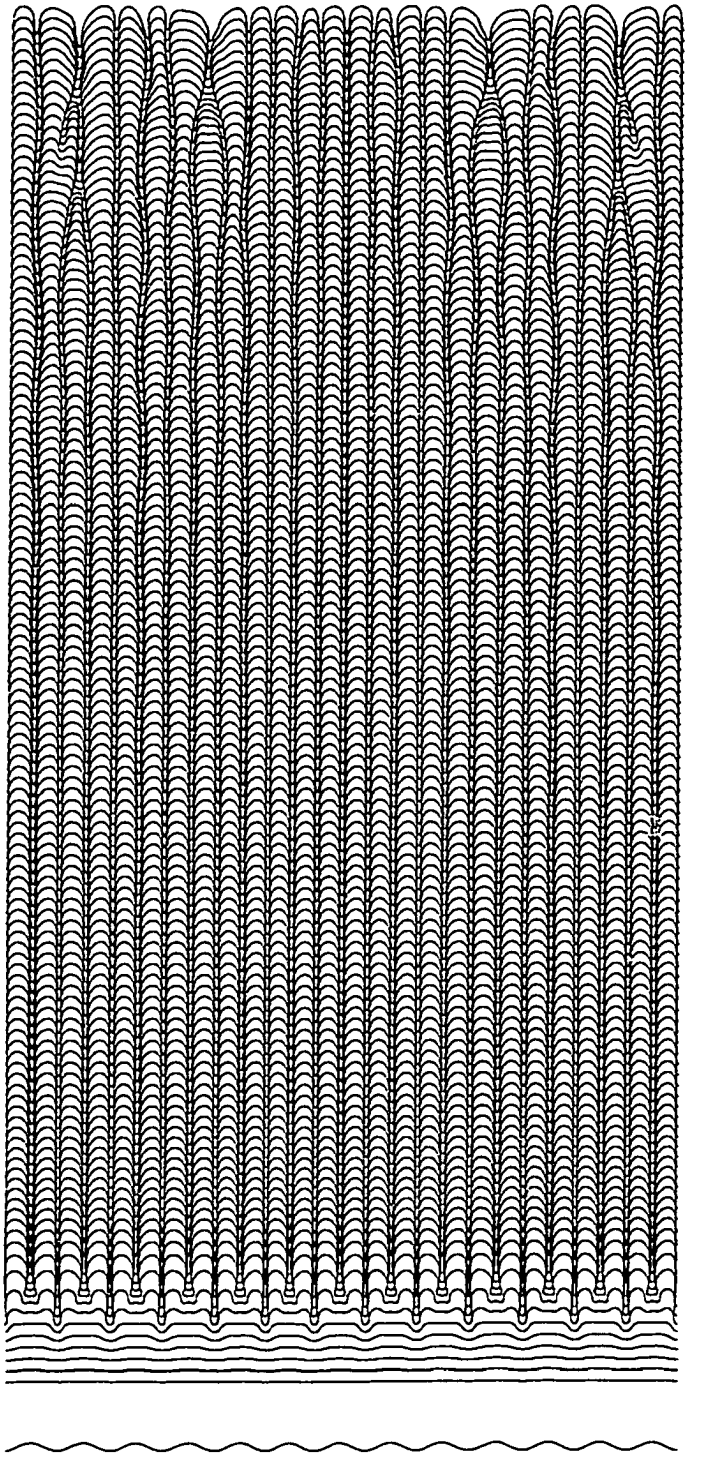

Figure C.5: As Fig. C.3 but now with $\lambda_P = 125.97$. The system displays an oscillatory instability.

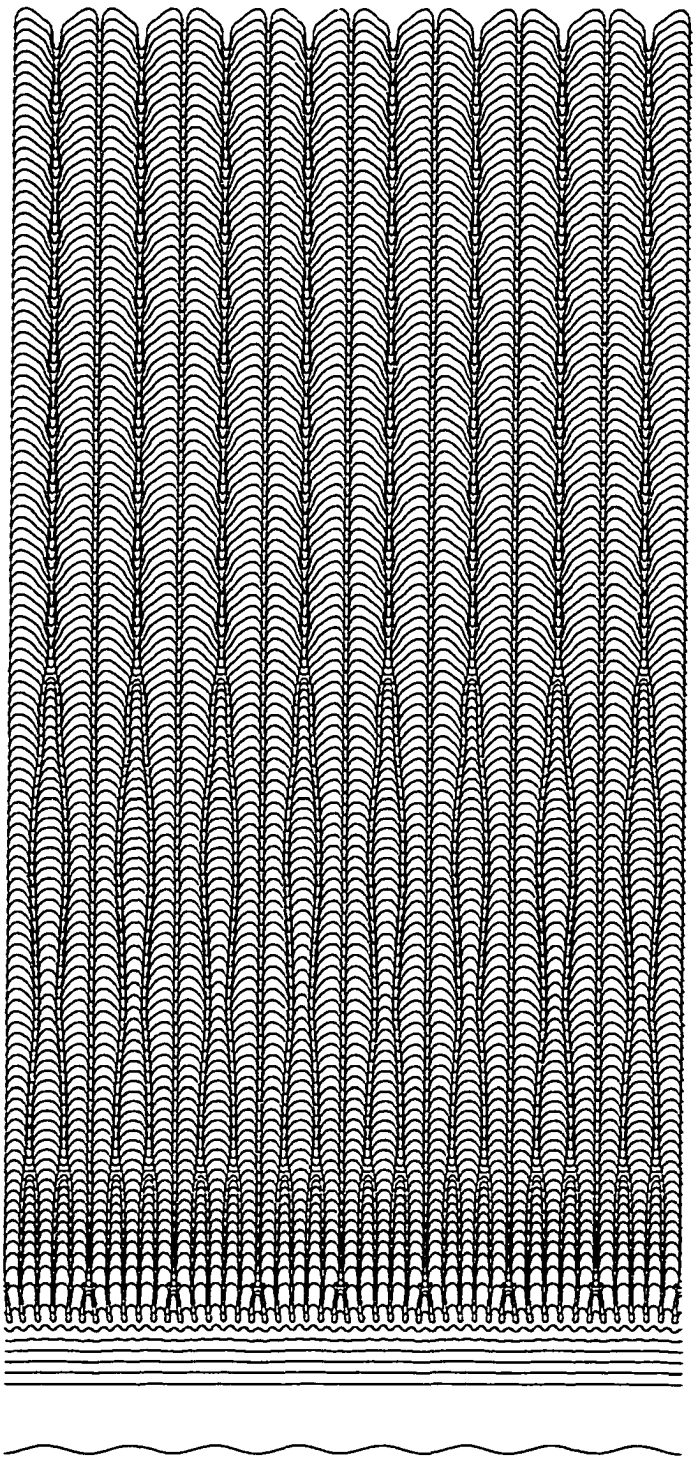

Figure C.6: As Fig. C.3 but now with $\lambda_P = 204.7$. The system displays a waving or a breathing instability.

with the experimental observations 7.6, doublets with small asymmetry appear to be stable initially until an oscillatory instability develops, which leads to an overgrowth of some of the cells.

On the large wavelength side, the stable domain is bounded by another type of instability described previously during establishing the stable band of the doublet branch. This mode, corresponding to the initial perturbation with $\lambda_P = 204.7$ and clearly visible in a final stage of the interface evolution shown in Fig. C.6, is similar to the experimentally observed instability 7.5. The doublets prone to this instability, despite performing a waving or a breathing motion along their long sides, remain intact for some small window of wavelengths around point E in Fig. C.1.

As one further increases the initial perturbation wavelength, an irregular spatio-temporal instability takes place and is qualitatively similar to the one observed in the experiments (point F in Fig. C.1, interface evolution not shown).

Finally, we have verified that we can dynamically select a state in the stable domain of a main branch (point A in Fig. C.1) through a tip splitting starting with $\lambda_P = 102.36$ (Fig. C.7) or directly starting with $\lambda_P = 51.18$ (not shown).

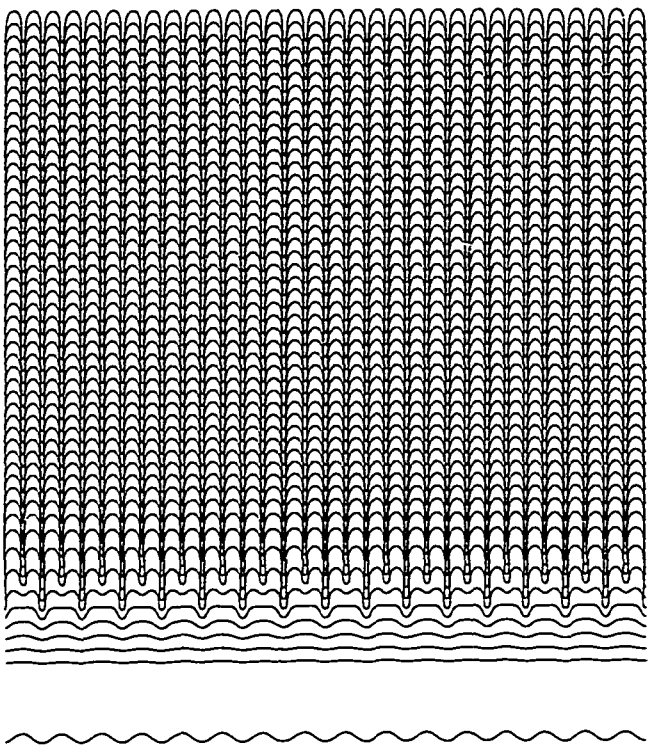

Figure C.7: As Fig. C.3 but now with $\lambda_P = 102.36$. The system settles in a periodic cellular array directly.

Bibliography

[1] W. Losert, B.Q. Shi, H.Z. Cummins, and J.A. Warren. Spatial period-doubling instability of dendritic arrays in directional solidification. *Phys. Rev. Lett.*, 77(5):889–891, 1996.

[2] W. Losert, B.Q. Shi, and H.Z. Cummins. Evolution of dendritic patterns during alloy solidification: Onset of the initial instability. *Proc. Nat. Acad. Sci. USA*, 95:431 -438, 1998.

[3] W. Losert, B.Q. Shi, and H.Z. Cummins. Evolution of dendritic patterns during alloy solidification: From the initial instability to the steady state. *Proc. Nat. Acad. Sci. USA*, 95:439–442, 1998.

[4] W. Losert, D.A. Stillman, H.Z. Cummins, P. Kopczyński, W.-J. Rappel, and A. Karma. Doublet cellular pattern in directional solidification selected through spatially periodic perturbations. *to be submitted Phys. Rev. E*, pages –, 1998.

[5] I. Kepler. *Seu de nive sexangula.* G. Tampach ed., Frankfurt on Main, 1611.

[6] I. Kepler. *The six-cornered snowflake.* Oxford at the Claredon Press, Oxford, 1966.

[7] M. McLean. *Directionallly Solidified Materials for High Temperature Service.* The Metals Society, London, 1983.

[8] W.J. Broad. Faulty rivets emerge as clues to titanic disaster. *The New York Times*, January 27:F1, 1998.

[9] N.R. Grugel. Microstructural evolution of primary dendrite trunks in directionally solidified, hypoeutectic, aluminum-silicon alloys. *Metal. Trans. A*, 26 A:496–499, 1995.

[10] S. Kumai, J. Hu, Y. Higo, and S. Nunomura. *Acta Mater.*, 46(6):2249–2257, 1996.

[11] C.H. Caceres and J.R. Griffiths. Strength of materials: Fundamental physical aspects of the strength of crystalline materials. In *ICSMA 10, Proceedings of the 10th International Conference*, pages 451–454, 1994.

[12] P.R. Scheller, P. Papaiacovou, D.-Y. Lin, M. Çöl, and Wienfried Dahl. The influence of solidification morphology on the high-temperature mechanical properties of an 18-10crni steel. *Steel Research*, 66(12):530–536, 1995.

[13] Y.L. Liu and S.R. Kang. *Materials Science and Technology*, 12(1):12–18, 1996.

[14] W. Kurz and R. Trivedi. Solidification microstructures: Recent developments and future directions. *Acta Metall. Mater.*, 38:1–17, 1990.

[15] M. W. Mullins and R. F. Sekerka. Stability of a planar interface during directional solidification of a dilute binary alloy. *J. Appl. Phys.*, 35(2):444–451, 1964.

[16] W. Kurz and D.J. Fisher. Dendritic growth at the limit of stability: Tip radius and spacing. *Acta Metal.*, 29:11–20, 1981.

[17] S. Akamatsu, G. Faivre, and T. Ihle. Symmetry broken doublet fingers and seaweed patterns in thin-film directional solidification of a nonfaceted cubic crystal. *Phys. Rev. E*, 51(5):4751–4773, 1995.

[18] T. Ihle and H. Müller-Krumbhaar. Diffusion-limited fractal growth morphology in thermodynamical two-phase systems. *Phys. Rev. Lett.*, 70(20):3083–3086, 1993.

[19] T. Ihle and H. Müller-Krumbhaar. Fractal and compact growth morphologies in phase transitions with diffusive transport. *Phys. Rev. E*, 49(4):2972–2991, 1994.

[20] H. Jamgotchian, R. Trivedi, and B. Billia. Array of doublets: A branch of cellular solutions in directional solidification. *Phys. Rev. E*, 47(6):4313–4322, 1993.

[21] P. Kopczyński, W.-J. Rappel, and A. Karma. Cellular multiplets in directional solidification. *Phys. Rev. E*, 55(2):R1282–R1285, 1997.

[22] J.W. Rutter and B. Chalmers. A prismatic substructure formed during solidification of metals. *Canadian Journal of Physics*, 31:15–39, 1953.

[23] W. A. Tiller, K. A. Jackson, J. W. Rutter, and B. Chalmers. The redistribution of solute atoms during the solidification of metals. *Acta Metall.*, 1:428–437, 1953.

[24] K.A. Jackson and J.D. Hunt. Transparent compounds that freeze like metals. *Acta Metall.*, 13:1212–1215, 1965.

[25] J.D. Hunt, K.A. Jackson, and H. Brown. Temperature gradient microscope stage suitable for freezing materials with melting points between -100^{o}c and $+200^{o}$c. *Rev. Sci. Instr.*, 37:805–805, 1966.

[26] D. P. Woodruff. *The solid-liquid interface.* Cambridge University Press. 1973.

[27] W. Kurz and D.J. Fisher. *Fundamentals of Solidification.* Trans Tech Publications, Switzerland, 1984.

[28] R. Trivedi and W. Kurz. Dendritic growth. *Inter. Mater. Rev.*, 39(2):49–74, 1994.

[29] D. Bouchard and J. S. Kirkaldy. Scaling of intragranular dendritic microstructure in ingot solidification. *Metal. Trans. B*, 27B:101–113, 1996.

[30] P.C. Searson, J.M. Macaulay, and F.M. Ross. *J. Appl. Phys.*, 72(1):253–??, 1992.

[31] K. Somboonsuk, J. T. Mason, and R. Trivedi. Interdendritic spacing : Part i. experimental studies. *Metal. Trans. A*, 15 A:967, 1984.

[32] R. Trivedi and K. Somboonsuk. Constrained dendritic growth and spacing. *Mater. Sci. Eng.*, 65:65–74, 1984.

[33] D. A. Kessler, J. Koplik, and H. Levine. Pattern selection in fingered growth phenomena. *Advances in Physics*, 37(2):255–339, 1988.

[34] J. S. Langer. Dendrites, viscous fingers, and the theory of pattern formation. *Science*, 243:1150–1156, 1989.

[35] R. Trivedi. Interdendritic spacing: Part ii. a comparison of theory and experiment. *Metal. Trans. A*, 15A:977–982, 1984.

[36] S.-Z. Lu and J. D. Hunt. A numerical analysis of dendritic and cellular array growth: The spacing adjustment mechansims. *J. Cryst. Growth*, 123:17–34, 1992.

[37] W. D. Huang, X. G. Geng, and Y. H. Zhou. Primary spacing selection of constrained dendritic growth. *J. Cryst. Growth*, 134:105–115, 1993.

[38] S. H. Han and R. Trivedi. Primary spacing selection in directionally solidified alloys. *Acta Metall. Mater.*, 42(1):25–41, 1994.

[39] J. A. Warren and J. S. Langer. Prediction of dendritic spacings in a directional solidification experiment. *Phys. Rev. E*, 47(4):2702–2712, 1993.

[40] J. A. Warren and J. S. Langer. Stability of dendritic arrays. *Phys. Rev. A*, 42(6):3518–3525, 1990.

[41] D. Bouchard and J. S. Kirkaldy. Predictions of dendrite arm spacings in unsteady- and steady-state heat flow of unidirectionally solidified binary alloys. *Metal. Trans. B*, 28B:651–663, 1997.

[42] V. Seetharaman, M. A. Eshelman, and R. Trivedi. Cellular spacings-ii. dynamical studies. *Acta Metall.*, 36(4):1175–1185, 1988.

[43] L. M. Williams, M. Muschol, X. Qian, W. Losert, and H. Z. Cummins. Dendritic sidebranching with periodic localized perturbations: Directional solidification of pivalic acid-coumarin 152 mixtures. *Phys. Rev. E*, 48:489–499, 1993. Erratum: *Phys. Rev. E* 48:4862.

[44] M. Rabaud, Y. Couder, and N. Gerard. Dynamics and stability of anomalous saffman-taylor fingers. *Phys. Rev. A*, 37(3):935–947, 1988.

[45] S.A. Curtis and J.V. Maher. Racetrack for competing viscous fingers. *Phys. Rev. Lett.*, 63(25):2729–2732, 1989.

[46] E. Ben-Jacob, R. Godbey, N.D. Goldenfeld, J. Koplik, H. Levine, T. Mueller, and L.M. Sander. Experimental demonstration of the role of anisotropy in interfacial pattern formation. *Phys. Rev. Lett.*, 55(12):1315–1318, 1985.

[47] J.-M. Flesselles, A.J. Simon, and A.J. Libchaber. Dynamics of one-dimensional interfaces: An experimentalist's view. *Advances in Physics*, 40:1–51, 1991.

[48] H. Assadi and A.L. Greer. The interfacial undercooling in solidification. *J. Cryst. Growth*, 172:249–258, 1997.

[49] R. F. Sekerka. Optimum stability conjecture for the role of interface kinetics in selection of the dendrite operating state. *J. Cryst. Growth*, 154:377–385, 1995.

[50] G. B. McFadden, A. A. Wheeler, R. J. Braun, and S. R. Coriell. Phase-field models for anisotropic interfaces. *Phys. Rev. E*, 48(3):2016–2024, 1993.

[51] R. Trivedi and J. T. Mason. The effects of interface attachment kinetics on solidification interface morphologies. *Metal. Trans. A*, 22A:235–249, 1991.

[52] B. Caroli, C. Caroli, and B. Roulet. Instabilities of planar solidification fronts. In Goodrèche, editor, *Solids far from equilibrium*, chapter 2, pages 155–296. Cambridge University Press, Cambridge, 1991.

[53] J. S. Langer. Instabilities and pattern formation in crystal growth. *Rev. Mod. Phys.*, 52:1–28, 1980.

[54] L. H. Ungar and R. A. Brown. Cellular interface morphologies in directional solidification. the one-sided model. *Phys. Rev. B*, 29(3):1367–1380, 1984.

[55] D. Liu, L. M. Williams, and H. Z. Cummins. Subcritical-supercritical bifurcation crossover in directional solidification. *Phys. Rev. E*, 50(6):R4286–R4289, 1994.

[56] B. Caroli, C. Caroli, and B. Roulet. On the emergence of one-dimensional front instabilities in directional solidification and fusion of binary mixtures. *J. Phys. (Paris)*, 43:1767–1780, 1982.

[57] R. Trivedi and K. Somboonsuk. Pattern formation during the directional solidification of binary systems. *Acta Metall.*, 33(6):1061–1068, 1985.

[58] J. I. Alexander, D. J. Wollkind, and R. F. Sekerka. The effect of latent heat on weakly non-linear morphological stability. *J. Cryst. Growth*, 79:849–865, 1986.

[59] J.M.A. Figueiredo and O.N. Mesquita. Morphological instability of a nonequilibrium nematic-isotropic interface. *Phys. Rev. E*, 53(3):2423–2435, 1996.

[60] J.M.A. Figueiredo, A.Vidal, and O.N. Mesquita. Planar-cellular instability in a growing nematic-isotropic interface. *J. Cryst. Growth*, 166:222–227, 1996.

[61] B. Caroli, C. Caroli, and L. Ramirez-Piscina. Initial front transients in directional solidification of thin samples of dilute alloys. *J. Cryst. Growth*, 132:377–388, 1993.

[62] P. Kopczynski, W.-J. Rappel, and A. Karma. Critical role of crystalline anisotropy in the stability of cellular array structures in directional solidification. *Phys. Rev. Lett.*, 77(16):3387–3390, 1996.

[63] J. A. Warren. How does a metal freeze? a phase-field model of alloy solidification. *IEEE Computational Science and Engineering*, Summer:38–49, 1995.

[64] A.A. Wheeler, N.A. Ahmad, W.J. Boettinger, R.J. Braun, G.B. McFadden, and B.T. Murray. Recent developments in phase-field models of solidification. *Advances in Space Research*, 16:(7)163–(7)172, 1995.

[65] O. Penrose and P. C. Fife. Thermodynamically consistent models of phase-field type for the kinetics of phase transitions. *Physica D*, 43:44–62, 1990.

[66] J. A. Warren and W. J. Boettinger. Prediction of dendritic growth and microsegregation patterns in a binary alloy using the phase-field method. *Acta Metall. Mater.*, 43(2):689–703, 1995.

[67] S. L. Wang, R. F. Sekerka, A. A. Wheeler, B. T. Murray, S. R. Coriell, R. J. Braun, and G. B. McFadden. Thermodynamically-consistent phase-field models for solidification. *Physica D*, 69:189–200, 1993. .

[68] J.S. Langer. *Directions in Condensed Matter*, page 164. World Scientific, Singapore, 1986.

[69] R. Kobayashi. *Experimental Math*, 3:60–81, 1994.

[70] R. Kobayashi. Modeling and numerical simulations of dendritic crystal growth. *Physica D*, 63:410–423, 1993.

[71] O. Penrose and P. C. Fife. On the relation between the standard phase-field model and the thermodynamically consistent phase field model. *Physica D*, 69:107–113, 1993.

[72] S.-L. Wang and R.F. Sekerka. Computation of the dendritic operating state at large supercoolings by the phase filed model. *Phys. Rev. E*, 53(4):3760–3776, 1996.

[73] R.J. Braun and B.T. Murray. Adaptive phase-field computations of dendritic crystal growth. *J. Cryst. Growth*, 174:41–53, 1997.

[74] A. Karma and W.-J. Rappel. Phase-field method for computationally efficient modeling of solidification with arbitrary interface kinetics. *Phys. Rev. E*, 53(4):1–4, 1996.

[75] A. Karma and W.-J. Rappel. Numerical simulation of three-dimensional dendritic growth. *Phys. Rev. Lett.*, 77(19):4050–4053, 1996.

[76] A. Karma and W.-J. Rappel. Phase-field simulation of three-dimensional dendrites: Is microscopic solvability theory correct? *J. Cryst. Growth.* 174:54–64, 1997.

[77] D.J. Wollkind and L.A. Segel. A nonlinear stability analysis of the freezing of dilute binary alloys. *Phil. Trans. R. Soc. London*, 268:351–380, 1970.

[78] W. Eckhaus. *Studies in non-linear stability theory.* Springer Verlag, Berlin, 1965.

[79] J.S. Langer. Chance and matter. In J. Souletie, J. Vannimenus, and R. Stora, editors, *Lectures in the theory of pattern formation.* Les Houches Summer School, session 46, North Holland, Amsterdam, 1987.

[80] J. D. Weeks and W. van Saarloos. Stability and shapes of cellular profiles in directional solidification: Expansion and matching methods. *J Cryst. Growth*, 112:244–282, 1991. .

[81] P. Coullet and G. Iooss. Instabilities of one-dimensional cellular patterns. *Phys. Rev. Lett.*, 64(8):866–869, 1990.

[82] D. A. Kessler and H. Levine. Steady-state cellular growth during directional solidification. *Phys. Rev. A*, 39:3041–3052, 1989.

[83] M. A. Eshelman, V. Seetharaman, and R. Trivedi. Cellular spacings-i. steady state growth. *Acta Metall.*, 36(4):1165–1174, 1988.

[84] M. Georgelin and A. Pocheau. Oscillatory instability, limit cycle and transition to doublets in directional solidification. *Phys. Rev. Lett.*, 79(14):2698–2701, 1997.

[85] P. Kopczyński, A. Karma, and W.-J. Rappel. to be published.

[86] G.P. Ivantsov. *Dokl Akad. Nauk SSSR*, 58:567, 1947.

[87] J. S. Langer and H. Müller-Krumbhaar. Theory of dendritic growth-i. elements of a stability analysis. *Acta Metall.*, 26:1681–1688, 1978.

[88] J. S. Langer and H. Müller-Krumbhaar. Theory of dendritic growth-ii. instabilities in the limit of vanishing surface tension. *Acta Metall.*, 26:1689–1696, 1978.

[89] J. S. Langer and H. Müller-Krumbhaar. Theory of dendritic growth-iii. effects of surface tension. *Acta Metall.*, 26:1697–1708, 1978.

[90] M. Muschol, D. Liu, and H. Z. Cummins. Surface-tension-anisotropy measurements of succinonitrile and pivalic acid: Comparison with microscopic solvability theory. *Phys. Rev. A*, 46:1038–1050, 1992.

[91] M. Ben-Amar and E. Brener. *Phys. Rev. Lett.*, 71:589, 1993.

[92] C. Misbah, H. Müller-Krumbhaar, and Y. Saito. Dendritic growth and directional solidification. *J. Cryst. Growth*, 99:156–160, 1990.

[93] M. N. Barber, A. Barbieri, and J. S. Langer. Dynamics of dendritic sidebranching in the two-dimensional symmetric model of solidification. *Phys. Rev. A*, 36:3340–3349, 1987.

[94] M. A. Chopra, M. E Glicksman, and N.B. Singh. Dendritic solidification of binary alloys. *Metal. Trans. A*, 19A:3087–3096, 1988.

[95] M. E. Glicksman, R. J. Schaefer, and J. D. Ayers. Dendritic growth: A test of a theory. *Metal. Trans. A*, 7A:1749–1759, 1976.

[96] K.A. Jackson. Defect formation, microsegregation and crystal growth morphology. In *Solidification*, chapter 5. American Society for Metals, Metals Park, OH, 1971.

[97] C.A. Wulff and E.F.Jr. Westrum. Heat capacities and thermodynamic properties of globular molecules. vi. succinonitrile. *J. Phys. Chem.*, 67:2476–2381, 1963.

[98] Sigma Chemical Co.

[99] E.R. Rubinstein, S.H. Tirmizi, and M.E.Glicksman. Long-term purity assessment in succinonitrile. *J. Cryst. Growth*, 106:89–96, 1990.

[100] S. Akamatsu and G. Faivre. Residual impurity effects in directional solidification: Long-lasting recoil of the front and nucleation-growth of gas bubbles. *J. Phys. I France*, 6:503–527, 1996.

[101] L.M. Williams, M.R. Srinivasan, and H.Z. Cummins. Direct observation of microbubbles in directional solidification of salol. *Phys. Rev. Lett.*, 64(13):1526–1528, 1990.

[102] J. Bechhoefer, P. Oswald, A. Libchaber, and C. Germain. Observations of cellular and dendritic growth of a smecticb smectica interface. *Phys. Rev. A*, 37(5):1691–1696, 1988.

[103] J. Bechhoefer. *Directional solidification at the nematic-isotropic interface.* PhD thesis, University of Chicago, 1988.

[104] J. Bechhoefer, A. J. Simon, A. Libchaber, and P. Oswald. Destabilisation of a flat nematic-isotropic interface. *Phys. Rev. A*, 40(4):2042–2056, 1989.

[105] J.M.A. Figueiredo, M.B.L. Santos, L.O. Ladeira, and O.N. Mesquita. Transient dynamics of a cellular front instability during directional solidification. *Phys. Rev. Lett.*, 71(26):4397–4400, 1993.

[106] R. Ragnarsson. private communication.

[107] Y. Xia and R.A. Brown. Measurement of the onset of two-dimensional cellular solidification in the succinonitrile-acetone binary alloy. *J. Cryst. Growth*, 154:205–210, 1995.

[108] S. de Cheveigne, C. Guthmann, P. Kurowski, E. Vincente, and H. Biloni. Directional solidification of metallic alloys: The nature of the bifurcation from planar to cellular interface. *J. Cryst. Growth*, 92:616–628, 1988.

[109] S.C. Huang and M.E. Glicksman. Fundamentals of dendritic solidification i. steady-state tip growth. *Acta Metall.*, 29:701–716, 1981.

[110] M. A. Chopra, M. E Glicksman, and N.B. Singh. Measurement of the diffusion coefficient of acetone in succinonitrile at its melting point. *J. Cryst. Growth*, 92:543–546, 1988.

[111] H. Chou and H. Z. Cummins. Evolution of the dendritic instability in solidifying succinonitrile. *Phys. Rev. Lett.*, 61:173–176, 1988.

[112] J.M.A. Figueiredo. private communication.

[113] S. de Cheveigne, C. Guthmann, and M.-M. Lebrun. Cellular instabilities in directional solidification. *J. Phys. (Paris)*, 47:2095–2103, 1986.

[114] Q. Li, H. N. Thi, H. Jamgotchian, and B. Billia. Preferred-pattern formation during initial transients in directional solidification. *Acta Metall. Mater.*, 43(3):1271–1278, 1995.

[115] G. Ding, W. Huang, X. Lin, and Y. Zhou. Prediction of average spacing for constrained cellular/dendritic growth. *J. Cryst. Growth*, 177:281–288, 1997.

[116] K. Somboonsuk and R. Trivedi. Dynamical studies of dendritic growth. *Acta Metall.*, 33:1051–1060, 1985.

[117] B. Billia and R. Trivedi. Pattern formation in crystal growth. In D. T. J. Hurle, editor, *Handbook of crystal growth*, volume 1, chapter 14, pages 899–1073. Elsevier Science Publishers B. V., 1993.

[118] J. D. Hunt and S.-Z. Lu. Numerical modeling of cellular/dendritic array growth: Spacing and structure prediction. *Metal. Trans. A*, 27A:611–623, 1996.

[119] T.S. Plaskett and W.C. Winegard. Cell to dendrite transition in tin base alloys. *Can. J. Phys.*, 38:1077–1088, 1960.

[120] A. Karma and W.J. Rappel. to be published in Phys. Rev. E.

[121] S.N. Tewari and R. Shah. Macrosegregation during steady-state arrayed growth of dendrites in directionally solidified pb-sn alloys. *Metal. Trans. A*, 23 A:3383–3392, 1992.

[122] W.-J. Rappel. Asymmetric cells in directional solidification. *Phys. Rev. E*, 48(5):4118–4120, 1993.

[123] B. Caroli, C. Caroli, and B. Roulet. The mullins-sekerka instability in directional solidification of thin samples. *J. Cryst. Growth*, 76:31–49, 1986.

[124] G. Grange, C. Jourdan, J. Gastaldi, and B. Billia. *J. Physique III*, 4:293, 1994.

[125] B. Billia, H. Jamgotchian, and H. N. Thi. Influence of sample thickness on cellular branches and cell-dendrite transition in directional solidification of binary alloys. *J. Cryst. Growth*, 167:265–276, 1996.

[126] A.A. Wheeler, B.T. Murray, and R.J. Schaefer. Computation of dendrites using a phase field model. *Physica D*, 66:243–262, 1993.

[127] T. Abel, E. Brener, and H. Müller-Krumbhaar. Three-dimensional growth morphologies in diffusion controlled channel growth. *Phys. Rev. E*, 55(6):7789–7792, 1997.

[128] J. S. Langer. Studies in the theory of interfacial stability-ii. moving symmetric model. *Acta Metall.*, 25:1120–1137, 1977.

IMAGE EVALUATION TEST TARGET (QA-3)

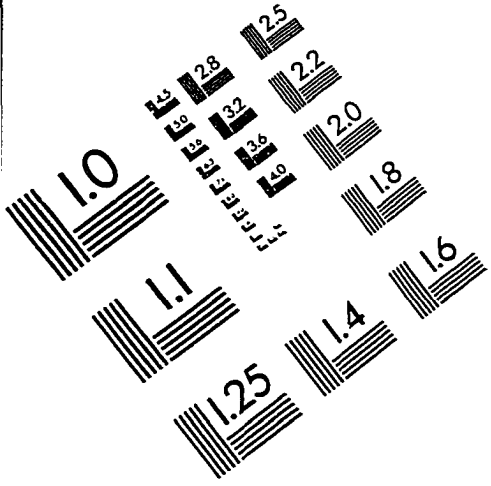

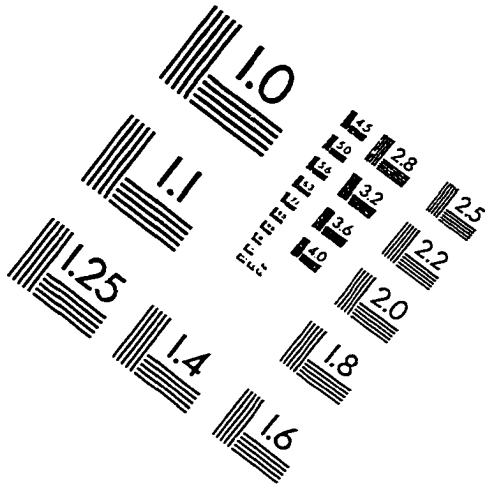

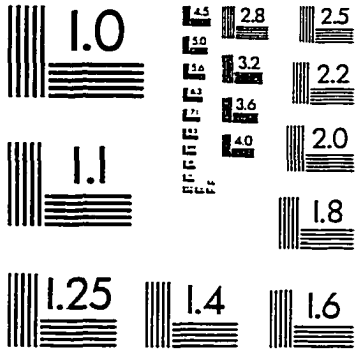

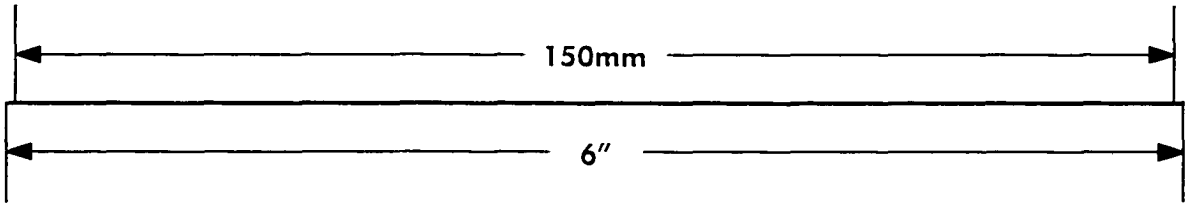

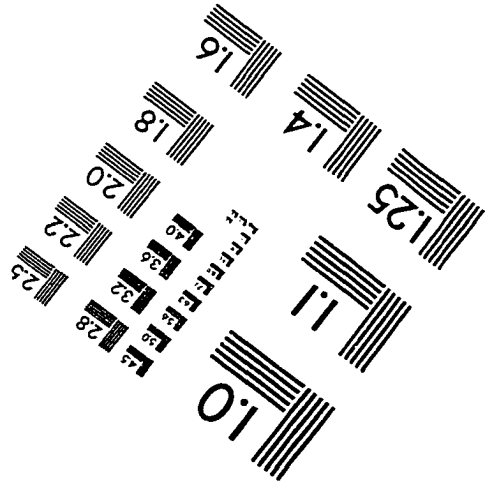

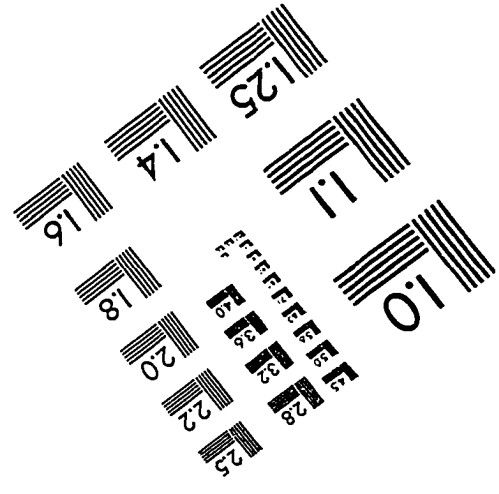

APPLIED IMAGE, Inc
1653 East Main Street
Rochester, NY 14609 USA
Phone: 716/482-0300
Fax: 716/288-5989